

PROMOTING LOWER AUSFERRITE TRANSFORMATION IN SINTERED

FE-4.00NI-0.50MO-SI-C ALLOY BY CO ADDITION



A THESIS REPORT SUBMITTED IN PARTIAL FULFILLMENT
OF THE REQUIREMENTS FOR THE DEGREE OF
MASTER OF ENGINEERING IN AUTOMOTIVE AND ADVANCED TRANSPORTATION
ENGINEERING
SCHOOL OF ENGINEERING
KING MONGKUT'S INSTITUTE OF TECHNOLOGY LADKRABANG
YEAR 2024
KMITL-2024-EN-M-277-284

This material is reserved for educational use only, not allowed for commercial use.

Forbidden to modify the content, and cite the document when use.



COPYRIGHT 2024

SCHOOL OF ENGINEERING

KING MONGKUT'S INSTITUTE OF TECHNOLOGY LADKRABANG

This material is reserved for educational use only, not allowed for commercial use.

III

Forbidden to modify the content, and cite the document when use.

THESIS TITLE Promoting Lower Ausferrite Transformation in Sintered Fe-4.00Ni-0.50Mo-Si-C alloy by Co Addition

STUDENT NAME Mr. Putsaccada Viseth

STUDENT ID 64601181

DEGREE Master of Engineering

PROGRAMME Automotive and Advanced Transportation Engineering

ADVISOR Asst. Prof. Dr. Jittraporn Wongsangam

CO-ADVISOR Dr. Ruangdaj Tongsi



ABSTRACT

Sintered iron-based alloy is one of the most widely used materials in the automotive industry due to its benefits namely near net shape, low strength-to-weight ratio, and low production cost. In addition to automotive applications, it has a high potential for applications in transportation-oriented industries such as the rail transportation industry. Despite this, fewer studies are conducted to improve the mechanical properties and tribological properties of sintered alloys, specifically on sintered Fe-based alloys. One of the main disadvantages of sintered Fe-based alloy is its ductility. Sintered Fe-based alloys have significantly low elongation values around 3-4 % due to their porosity. However, it would require a high production cost and additional tools to reduce porosity in sintered parts. High production costs are not preferred for any manufacturing. In this research, alloying element Co is added to Sintered Fe-Ni-Mo-Si-C alloys to modify their microstructure to improve their mechanical and tribological properties. Co-addition is expected to accelerate the bainitic transformation in sintered Fe-Ni-Mo-Si-C alloys. The increase of bainitic ferrite plates would lead to a high fraction of ausferrite having dual-phase lamellar microstructure (bainitic ferrite and austenite plates), which presumably led to evading the trade-off between strength and ductility in experimental sintered composites. It was found that the bainitic ferrite fraction increased with increasing added Co content. With bainitic ferrite transformation acceleration, the competitive martensite transformation was reduced. The sintered composites with austempered ductile iron-like microstructure (graphite nodules plus ausferrite without or with small martensite fraction) could be produced by adding Co contents of ³ 2.0 wt. %. As a result, tensile strength and elongation values of sintered composites increased with increasing Co content. High elongation values of up to 7 %, uncommonly high values for sintered composites, were obtained in sintered specimens. The increases of tensile strength and ductility with increasing Co content, indicating the evading strength-ductility trade-off dilemma, were attributed to the bainitic ferrite formation acceleration. However, the increase of Ausferrite formation seems to have an insensitive effect on to wear properties of sintered Fe-Ni-Mo-Si-C alloys.

ACKNOWLEDGEMENT

First of all, I would like to express my deepest appreciation to my NSTDA advisor Dr. Ruangdaj Tong Sri. He always supports and nurtures me by taking his busy schedule for me. I really appreciate the valuable advice, and his guidance for me from the start to finish of this research. I have learned and absorbed new knowledge in the research field. Moreover, he has not only contributed research ideas to my research but also explained the theoretical background and increased my insight into the powder metallurgy field. Without his help, surely, I surely wouldn't have completed my master's thesis.

Secondly, I am extremely grateful to Asst. Prof. Dr. Jitraporn Wongsan Ngam for her feedback and comment on my both thesis and paper. She always encouraged and motivated me during my research. Thirdly, I would like to thank all PMPT team member for their guidance and support from start to finish of my research work.

Next, I am extremely grateful for the scholarship provided by NSTDA and TAIST-Tokyo Tech. Also, I am also grateful for the support from the National Metal and Material Technology Center (MTEC) and King Mongkut's Institute of Technology Ladkrabang (KMUTL).

Finally, I must express my sincere thanks to my parents, who have always given me valuable pieces of advice, inspiration, and unconditional love since the moment I was born. Without their unwavering support in my research journey throughout the last two years, I would not have accomplished this achievement.

Putsaccada Viseth

TABLE OF CONTENTS

Chapter	Page
ABSTRACT	V
ACKNOWLEDGEMENT	VI
TABLE OF CONTENTS	VII
LIST OF TABLES	X
LIST OF FIGURES	XI
LIST OF SYMBOLS	XIV
LIST OF DEFINITIONS	XV
CHAPTER 1 INTRODUCTION	1
1.1 Research Background.....	1
1.2 Objectives	2
1.3 Scope of Work.....	3
CHAPTER 2 LITERATURE REVIEW.....	4
2.1 Overview of Powder Metallurgy.....	4
2.1.1 Conventional powder metallurgy	5
2.1.2 Application of iron-based sintered materials.....	7
2.2 Phase Transformation Theory.....	7
2.2.1 Iron-carbon phase diagram (Fe-C diagram).....	8
2.2.2 Time temperature transformation	9
2.2.3 Continuous cooling diagram.....	11
2.3 Overview of Microstructure in Steel and Alloys	13
2.3.1 Ferrite phase.....	13
2.3.2 Pearlite phase.....	13
2.3.3 Bainite phase	14
2.3.4 Martensite phase	16
2.4 Influence of Alloying Elements	16
2.4.1 Influence of alloying elements on eutectoid point (phase stabilization)....	17
2.4.2 Influence of alloying elements on martensite transformation.....	18
2.4.3 Influence of alloying elements on bainite transformation.....	18

This material is reserved for educational use only, not allowed for commercial use.

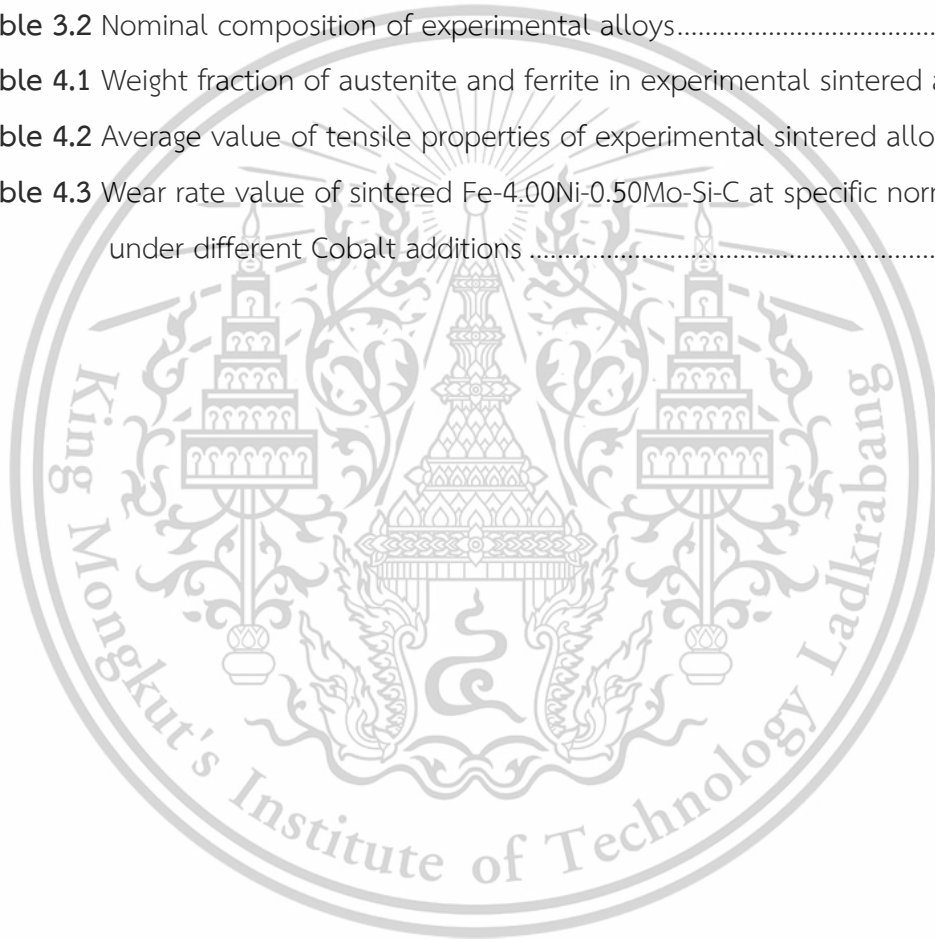
2.5 Effect of Cobalt (Co) Addition.....	19
2.5.1 Effect of cobalt on bainitic transformation.....	19
2.5.2 Influence of cobalt on mechanical properties of steels.....	22
2.6 Overview of Tribological Characterization.....	26
2.6.1 Pin-on-disc dry sliding wear test.....	26
2.6.2 Wear rate of materials.....	27
2.6.3 Wear mode of materials.....	27
2.7 Recent Researches on Sintered Fe-Based Alloys.....	29
CHAPTER 3 RESEARCH METHODOLOGY.....	32
3.1 Material Preparation.....	32
3.1.1 Based material.....	32
3.1.2 Addition of alloying elements.....	32
3.1.3 Experimental alloys.....	33
3.2 Sintered Specimen Preparation.....	34
3.2.1 Mixing step.....	34
3.2.2 Compacting step.....	35
3.2.3 Sintering step.....	36
3.3 Experimental Procedure.....	38
3.4 Microstructure Characterization.....	39
3.4.1 Optical microscope.....	39
3.4.2 Scanning electron microscopy (SEM).....	40
3.4.3 X-ray diffraction (XRD).....	41
3.4.4 Electron probe microanalyzer (EPMA).....	42
3.5 Metallography Preparation.....	43
3.5.1 Sectioning.....	43
3.5.2 Mounting.....	43
3.5.3 Grinding.....	44
3.5.4 Polishing.....	45
3.5.5 Chemical Etching.....	46
3.6 Mechanical Properties Determination.....	47
3.7 Hardness Test.....	47
3.8 Determination of Tribology Properties and Wear Rate.....	49
CHAPTER 4 RESULTS AND DISCUSSION.....	51

This material is reserved for educational use only, not allowed for commercial use.

4.1 Microstructure of Sintered Alloys.....	51
4.1.1 OM of sintered alloys without Co addition.....	51
4.1.2 OM of sintered alloys with Co addition.....	53
4.1.3 X-ray diffraction of sintered alloys.....	56
4.1.4 SEM images of sintered alloys without Co addition.....	58
4.1.5 SEM images of sintered alloys with Co addition.....	59
4.1.6 EPMA mapping analysis of sintered 00Co and 30Co alloys.....	61
4.2 Mechanical Properties of Sintered Alloys.....	64
4.2.1 Hardness of sintered alloys.....	64
4.2.2 Tensile properties of sintered alloys.....	64
4.2.3 Surface fracture of sintered alloys after tensile testing.....	68
4.3 Tribological Properties of Sintered Alloys.....	69
4.3.1 Friction coefficient of sintered alloys.....	69
4.3.2 Wear rate of sintered alloys.....	72
4.3.3 Worn surface of all sintered alloys at 5N normal load.....	74
4.3.4 Worn surface of all sintered alloys at 10N normal load.....	76
4.3.5 Worn surface of all sintered alloys at 15N normal load.....	79
4.3.6 Wear debris of all sintered alloys at 15N normal load.....	81
4.3.7 EDS inspection of wear debris at 15N normal load.....	83
CHAPTER 5 CONCLUSIONS AND RECOMMENDATION.....	85
5.1 Conclusion.....	85
5.2 Recommendation for Future Work.....	86
REFERENCES.....	87
APPENDIX A.....	94
APPENDIX B.....	96
AUTHOR BIOGRAPHY.....	100

LIST OF TABLES

Table	Page
Table 2.1 Summary of quantitative experimental data, V_B is bainitic ferrite fraction, reproduced from [11].	21
Table 2.2 Literature on mechanical properties of sintered Fe-base alloy/steels.	31
Table 3.1 Composition of ATOMET 4801	32
Table 3.2 Nominal composition of experimental alloys.	34
Table 4.1 Weight fraction of austenite and ferrite in experimental sintered alloys.	58
Table 4.2 Average value of tensile properties of experimental sintered alloys.	67
Table 4.3 Wear rate value of sintered Fe-4.00Ni-0.50Mo-Si-C at specific normal load under different Cobalt additions	73



LIST OF FIGURES

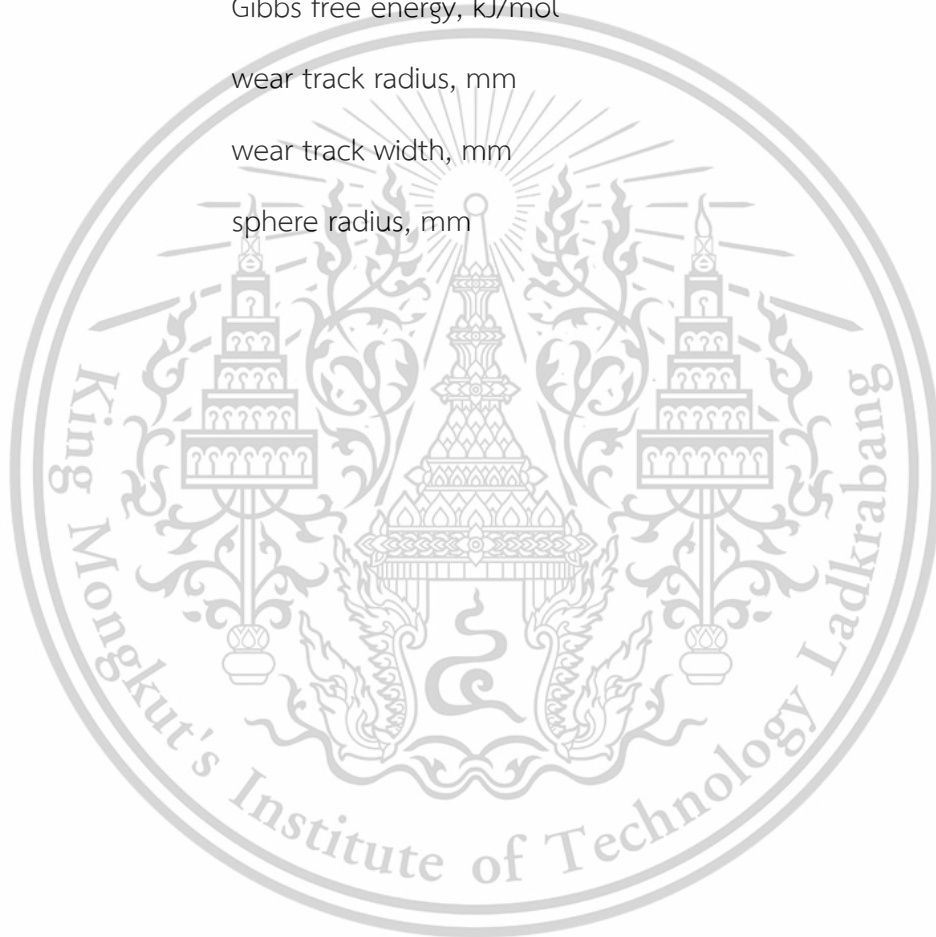
Figure	Page
Figure 2.1 Place of PM in material processing technology [12].....	4
Figure 2.2 Bearing and gear part made from P/M process [13].....	5
Figure 2.3 Flowchart of the traditional powder metallurgy process [14]	6
Figure 2.4 Model explaining the powder particles before and after sintering [15].....	7
Figure 2.5 PM structural products made from iron-based material [12].....	8
Figure 2.6 Fe-C phase diagram [17].....	9
Figure 2.7 Simplified diagrams of TTT and CCT in eutectoid steel [16].....	10
Figure 2.8 Time temperature transformation diagram for a eutectoid steel [16].....	11
Figure 2.9 CCT and TTT diagrams for a eutectoid steel with critical cooling rate [16]12	12
Figure 2.10 Four specimens of eutectoid steel cooled at different rates [16].....	12
Figure 2.11 Appearance of ferrite phase in quenched steel and Fe-0.4C steel [20]..	14
Figure 2.12 OM image of pearlite [19].....	14
Figure 2.13 Schematic representation of upper and lower bainite [21]	15
Figure 2.14 OM and TEM micrograph of bainite obtained at 200 °C [22].....	15
Figure 2.15 OM image of plate shape of martensite [19].....	16
Figure 2.16 Simplified sections of the Fe-C-Si diagram [23].....	17
Figure 2.17 Effect of alloying elements on martensite start temperature [24].....	18
Figure 2.18 The influence of Cr, Mo, W, and Mn on bainite transformation [25]	19
Figure 2.19 Free energy change as function of temperature [11]	20
Figure 2.20 Transformation time of bainite transformation [11].....	20
Figure 2.21 Effect of the Co and Al addition on shifting TTT curves [26].....	22
Figure 2.22 Volume fraction and thickness of the bainitic ferrite [26]	23
Figure 2.23 Engineering stress strain curve obtained at room temperature [28]	24
Figure 2.24 Tensile strength and yield strength versus Co content [27]	25
Figure 2.25 Hardness of both alloys versus Co content [27]	25
Figure 2.26 Schematic of pin-on-disc dry sliding wear test [30]	26
Figure 2.27 Common wear mechanisms: a) adhesive wear, b) abrasive wear and c) fatigue wear [36].....	29

Figure 2.28 UTS versus elongation from recent researches on Fe-base material.....	30
Figure 3.1 Alloying Elements.....	33
Figure 3.2 Analytical balance AND GF-400	33
Figure 3.3 Conventional process of powder metallurgy [43]	35
Figure 3.4 Mechanical rotating machine	35
Figure 3.5 Hydraulic Pressing Machine	36
Figure 3.6 Compacted specimens or green specimens.....	37
Figure 3.7 High vacuum sintering furnace (SCHMETZ).....	37
Figure 3.8 Sintering profile and inside view of sintering furnace	38
Figure 3.9 Compacted specimens after sintering.....	38
Figure 3.10 Flowchart of experimental procedure.....	39
Figure 3.11 Optical microscope (Olympus STM7).....	40
Figure 3.12 Scanning electron microscope (JSM-7800F Prime).....	40
Figure 3.13 X-Ray diffractometer machine, Rigaku TTRAX III.....	41
Figure 3.14 Electron Probe Microanalyzer Shimadzu 8050G.....	42
Figure 3.15 Cutting machine (StruersDiscotom-5).....	43
Figure 3.16 Compression mounting machine and mounting materials.....	44
Figure 3.17 Mechanical Rotating Machine for Grinding and Polishing	45
Figure 3.18 Silicon carbide papers	45
Figure 3.19 POLY-Diamond Suspension (Size 6, 3 and 1 micron).....	46
Figure 3.20 Polishing Clothes (6micron,3micron and 1micron).....	46
Figure 3.21 Chemical etchant used for normal and color etching.....	47
Figure 3.22 Tensile testing machine (Instron 8801).....	48
Figure 3.23 Hardness testing machine (Instron-930).....	48
Figure 3.24 Wear test set up (pin-on-disc sliding test).....	49
Figure 4.1 OM image of sintered Fe-4.00Ni-0.50Mo-0.20Mn-Si-C (low magnification) .	51
Figure 4.2 OM images of sintered 00Co composite, normal and two stage-tinted (color OM) low and high magnification.....	52
Figure 4.3 OM and tinted OM images of sintered composites: (a and b) sintered 05Co composite, (c and d) sintered 10Co composite, (e and f) sintered 15Co composite, (g and h) sintered 20Co composite, (i and j) sintered 25Co composite, and (k and l) sintered 30Co composite.....	56

Figure 4.4 XRD pattern of experimental sintered alloys (a) sintered 00Co, (b) sintered 05Co, (c) sintered 10Co, (d) sintered 15Co, (e) sintered 20Co, (f) sintered 25Co and (g) sintered 30Co alloys.....	57
Figure 4.5 SEM image of sintered 00Co alloy	59
Figure 4.6 SEM image of sintered alloys; (a) sintered 05Co, (b) sintered 10Co, (c) sintered 15Co, (d) sintered 20Co, (e) sintered 25Co and (f) sintered 30 alloys.....	60
Figure 4.7 Comparison of matrix of sintered composite; (a) sintered 05Co and (b) sintered 30Co.....	61
Figure 4.8 EPMA mapping of sintered 00Co alloy.....	62
Figure 4.9 EPMA mapping of sintered 30Co alloy.....	63
Figure 4.10 Hardness values of experimental sintered composites	65
Figure 4.11 Ultimate and yield strength of all sintered alloys	66
Figure 4.12 SEM images of surface fracture of sintered alloys; (a) 0.0Co alloy, (b) 1.5Co alloy and (c) 3.0Co alloy.....	68
Figure 4.13 Friction coefficient of all sintered alloys at difference normal load.....	69
Figure 4.14 Friction coefficient versus sliding distance at normal load 5N.....	71
Figure 4.15 Friction coefficient versus sliding distance at normal load 10.....	72
Figure 4.16 Friction coefficient versus sliding distance at normal load 15N.....	72
Figure 4.17 Wear rate at specific normal load of sintered Fe-4.00Ni-0.50Mo-0.20Mn-Si-C versus Co contents.....	74
Figure 4.18 SEM micrograph of worn surface of all sintered alloys at 5N normal load	76
Figure 4.19 SEM micrograph of worn surface of all sintered alloys at 10N normal load	78
Figure 4.20 SEM micrograph of worn surface of all sintered alloys at 15N normal load	81
Figure 4.21 SEM micrograph of wear debris at all sintered alloys at 15N normal load	83
Figure 4.22 EDS of wear debris of sintered 00Co alloy	83
Figure 4.23 EDS of wear debris of sintered 15Co alloy	84
Figure 4.24 EDS of wear debris of sintered 30Co alloy	84

LIST OF SYMBOLS

γ	austenite
α	ferrite
ρ_s	green density, g/cm ³
μ	friction coefficient
G	Gibbs free energy, kJ/mol
R	wear track radius, mm
d	wear track width, mm
r	sphere radius, mm



LIST OF DEFINITIONS

P/M	Powder Metallurgy
Co	Cobalt
Al	Aluminum
SEM	Scanning Electron Microscope
OM	Optical microscope
XRD	X-ray diffraction
SiC	Silicon carbide
B/F	Bainitic Ferrite
BP	Black Particle
M/A	Martensite austenite
Fe ₃ C	Cementite
M _s	Martensite start temperature
M _f	Martensite finish temperature
Wt.%	Weight percentages
BCT	Body-center tetragonal
BCC	Body-center cubic
FCC	Face-center cubic
HEAs	High entropy alloys

CHAPTER 1

INTRODUCTION

1.1 Research Background

Powder metallurgy is widely used in the automotive industry because of its advantages, namely its near-net shape-forming capability, less material waste, low weight-to-strength ratio, low production cost, and unique microstructure. The application of powder metallurgy (PM) is still growing along with the development trend in the automotive industry. Low weight-to-strength ratios and friction materials are common applications of PM materials for the automotive and rail transportation industries. The traditional powder metallurgy process, which consists of pressing and sintering, is the most widely used processing method among other routes of powder metallurgy. Many manufacturing industries prefer the traditional PM process because of its simplicity and lower cost compared to other PM processes. By compacting and sintering, it offers a significant degree of flexibility in terms of alloy composition and material microstructure. As a result, it can acquire properties that ordinary wrought steel cannot. Several features of PM products, for example, such as sintered friction materials consisting of metallic matrix composites, can be produced via this route, as reported in some previous studies [1]–[4].

High strength and high ductility are the key components in the path of sintered alloy improvement [5], [6]. The microstructure of the alloy or steel should have both soft and hard phases in order to exhibit good strength and ductility. Retained austenite and ferrite are the two typical soft phases that increase ductility. It is well known that sintered alloys have low ductility as a consequence of porosity. Nevertheless, reducing porosity in sintered parts would require costly extra tools, which is not ideal for manufacturing. Sintered alloys had an intriguing composition with a variety of microstructure phases, including ferrite, bainite, and martensite-austenite, which can only be manufactured by the sintering process. These microstructure formations have a significant impact on the mechanical properties, tribological properties, and wear behavior.

Many studies have been conducted over the years to improve the mechanical and wear properties of sintered materials, notably iron (Fe) base materials. Sintered iron-based alloys exhibited good tensile strength but low elongation for sintered

This material is reserved for educational use only, not allowed for commercial use.

materials. To increase its mechanical qualities even further, alloying elements were added to the base material to tailor its microstructure. It has been suggested that alloying elements like silicon carbide (SiC), molybdenum (Mo), and nickel (Ni) can affect the way sintered iron-based materials transform. According to a prior study [1], the interaction between sintered Fe and silicon carbide (Fe-SiC) composites produced superior tensile strength and a low elongation value. Molybdenum had demonstrated a significant impact on the development of bainite in Fe-SiC. As the Mo content increased, the elongation decreased while the tensile strength increased as a result of the matrix hardenability through bainite formation. A recent study by Tiwat et al. showed that Nickel has altered the microstructure of Fe-Mo-Si-C by suppressing pearlite transformation, resulting in bainitic ferrite (BF) and martensite austenite (M-A) transformations at low temperatures [7]. Martensite formation increased as nickel content increased. Surprisingly, while nickel concentration boosted tensile strength and hardness, elongation remained relatively low.

The fraction of martensite rather than lower Ausferrite or bainite may be due to ductility strengthening. According to Tiwat et al., there is a window for BF/M-A transformation at low temperatures because high nickel content can restrict ferrite and perlite transformation [7]. According to this hypothesis, the increase in martensite fraction in sintered Fe-Mo-Si-C alloy might be related to the very slow kinetics of bainite transformation at low temperatures.

It is commonly known that cobalt (Co) and aluminum (Al) can accelerate bainitic transformation [8]–[11]. In this study, Co addition was selected to modify the matrix of sintered Fe-Ni-Si-C composite with the aim of increasing the bainitic ferrite (BF) fraction, which would increase the ausferrite fraction. Due to the dual-phase lamellar microstructure of ausferrite, it was hypothesized that the increase in BF fraction would lead to an increase in ausferrite fraction in sintered Fe-Ni-Si-C composites. The nature of ausferrite lamellar structure was expected to improve mechanical properties, especially ductility enhancement, but it had an unknown influence on tribological properties.

1.2 Objectives

The thesis aims to study the following points:

- 1) To promote lower Ausferrite formation in sintered pre-alloyed Fe-4.00Ni-

This material is reserved for educational use only, not allowed for commercial use.

0.50Mo-0.20Mn powder by Cobalt addition

- 2) To investigate the effect of Cobalt addition on the microstructure and mechanical properties of sintered Fe-4.00Ni-0.50Mo-0.20Mn alloy
- 3) To investigate the effect of Cobalt addition on the tribological properties and its wear behaviors of sintered Fe-4.00Ni-0.50Mo-0.20Mn alloy

1.3 Scope of Work

This research is carried out within the following points below:

- 1) Co content varies from 0.50, 1.00, 1.50, 2.00, 2.50 and 3.00 wt.% are added to pre-alloyed powder ATOMET4801 with composition Fe-4.00Ni-0.50Mo-0.20Mn.
- 2) Green specimens are sintered at a temperature of 1250 °C for 45 minutes in a vacuum furnace and slowly cooled in the furnace.
- 3) Phase and microstructure of sintered Fe-4.00Ni-0.50Mo-0.20Mn-Co alloys are characterized by x-ray diffraction (XRD), optical microscope (OM), and Scanning Electron Microscope (SEM).
- 4) Mechanical properties and hardness value of sintered Fe-4.00Ni-0.50Mo-0.20Mn-Co alloys are determined by the uniaxial tensile test and Rockwell hardness test respectively.
- 5) Tribological properties including friction coefficient and wear rate of sintered Fe-4.00Ni-0.50Mo-0.20Mn-Co alloys are determined using the dry sliding pin on disk test.
- 6) Wear behaviors of sintered Fe-4.00Ni-0.50Mo-0.20Mn-Co alloys are investigated by observing the worn surface of disk specimens by SEM.

CHAPTER 2

LITERATURE REVIEW

2.1 Overview of Powder Metallurgy

Powder metallurgy (P/M) is a type of manufacturing technology that involves diffusing different metal powders through a sintering process. P/M offers low production costs, shape complexity, a high strength-to-weight ratio, high precision parts, and other advantages over traditional methods such as forging, casting, extrusion, stamping, and machining. PM has an important role in advanced material process technology because of its simplicity and versatility. **Figure 2.1** shows the role of P/M in material processing technology. Moreover, P/M offers more freedom to the composition of alloys and microstructure modification of the material. By controlling and modifying the microstructure, it can obtain properties that cannot be obtained by general wrought steel.

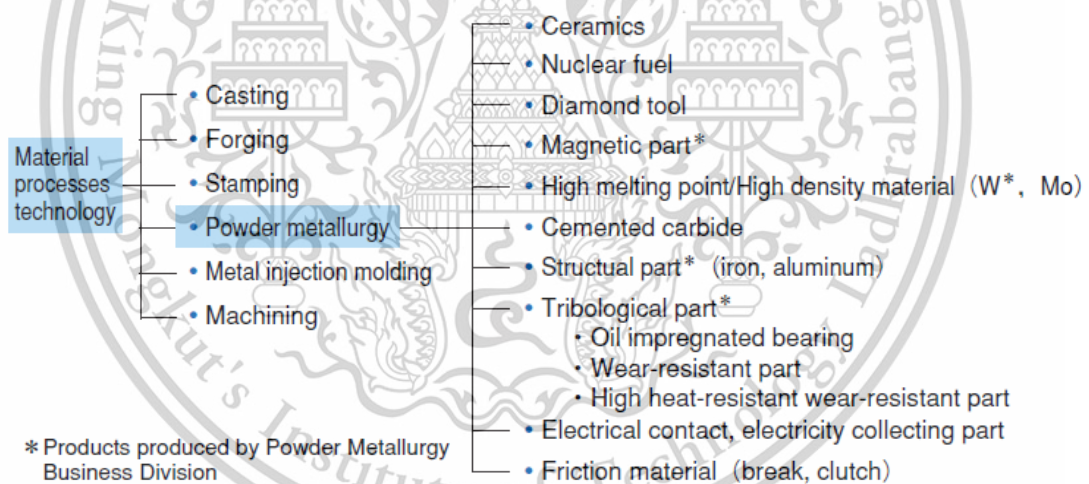


Figure 2.1 Place of PM in material processing technology [12]

Since many products can be utilized by PM, the main products of P/M are classified into three main parts, namely, structural parts, tribological parts, and magnetic parts. Structural parts contain a large portion of PM products. It comprises high-strength materials, high-dimensional precision parts, and sintered hardening materials. Tribological parts are roughly classified into bearing and heat-wear resistance materials, while magnetic parts contain sintered magnetic core material. The

development of magnetic parts is strongly influenced by the emerging electric vehicle, which cannot be achieved with wrought steel.

Even though PM is used by many industrial sectors, the automotive industry is responsible for over 90% of powder metallurgy products [12]. Some applications for PM in a vehicle are transmission, engine, battery, fuel injection, steering, shock absorber, brake disc, etc. **Figure 2.2** shows some bearing and gear parts made from the PM process.

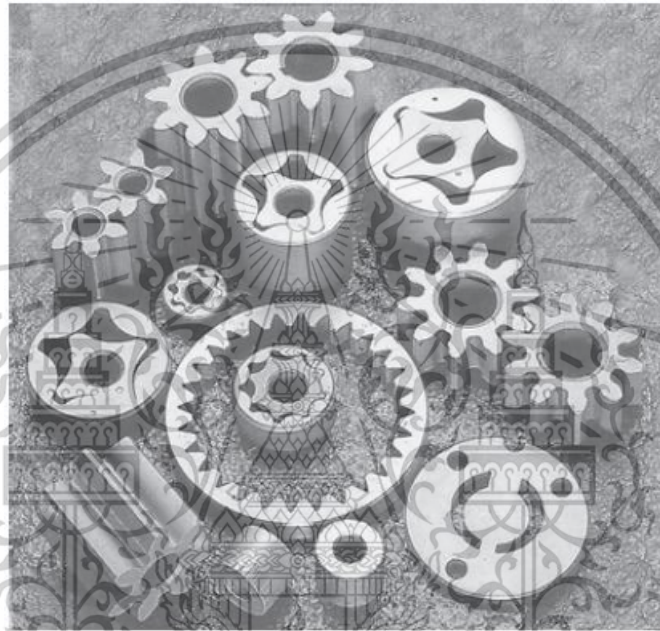


Figure 2.2 Bearing and gear part made from P/M process [13]

2.1.1 Conventional powder metallurgy

Many processing techniques for PM are available in the manufacturing industry, ranging from traditional or conventional press and sinter, metal injection molding (MIM), isostatic pressing (hot and cold isostatic pressing), and rapid prototyping [13]. Among the PM processing techniques mentioned, the traditional press and sinter is the most preferred method by the manufacturing industry because of its simplicity of operation. Traditional press and sinter process consists of mixing, pressing (compacting), and sintering. **Figure 2.3** shows the flowchart of the traditional powder metallurgy process.

- **Mixing/blending:** Raw powder of based alloy is mixed with alloying element and lubricant. The purpose of mixing is to produce a homogeneous mixture of base powder, alloying powder and lubricant powder. The role of lubricant is to

reduce friction between powder and the surface of the die compaction tool. Popular lubricants are metallic stearates, stearin, and zinc stearate (used in this study).

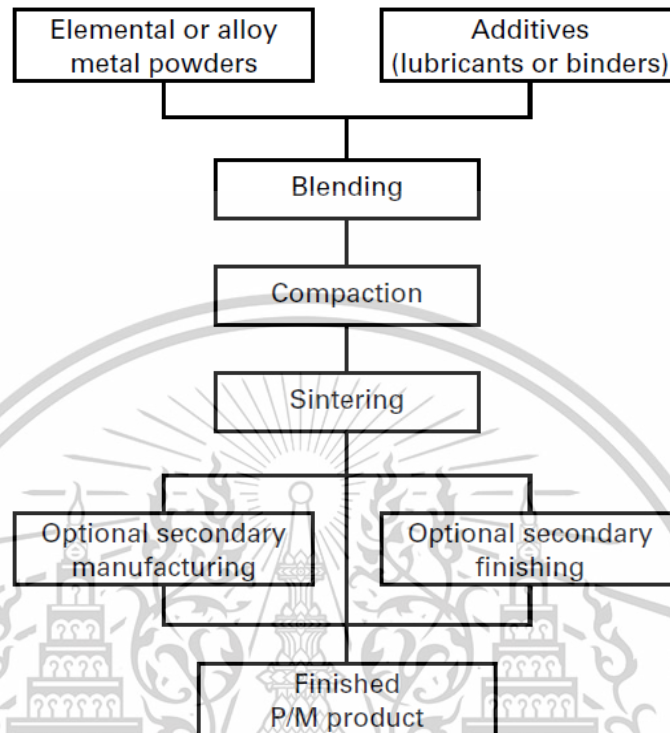


Figure 2.3 Flowchart of the traditional powder metallurgy process [14]

- **Compaction:** The mixed powders are compacted to a desired shape under a pressure of 150-900 MPa. In traditional powder metallurgy, cold compaction is used instead of warm and hot compaction. Mixed powders are bonded together by means of cold-welding between their powder grain. Moreover, compacted powders must be strong enough to withstand die ejection and handling purposes before sintering.
- **Sintering:** Sintering is the most important step in the process. It is the thermal treatment of a compacted powder at a temperature below the melting point of the main constituent to increase its strength by bonding powder particles together. **Figure 2.4** illustrates the necking behavior between powder particles. Sintering must be carried out in a controlled atmosphere and vacuum furnace because metals are prone to oxidation at elevated temperatures. Nitrogen (N₂) mixed with O₂ can be used as heat for sintering. Besides from mixture of N₂ and O₂, Hydrogen, Co, and CO₂ can also be used.

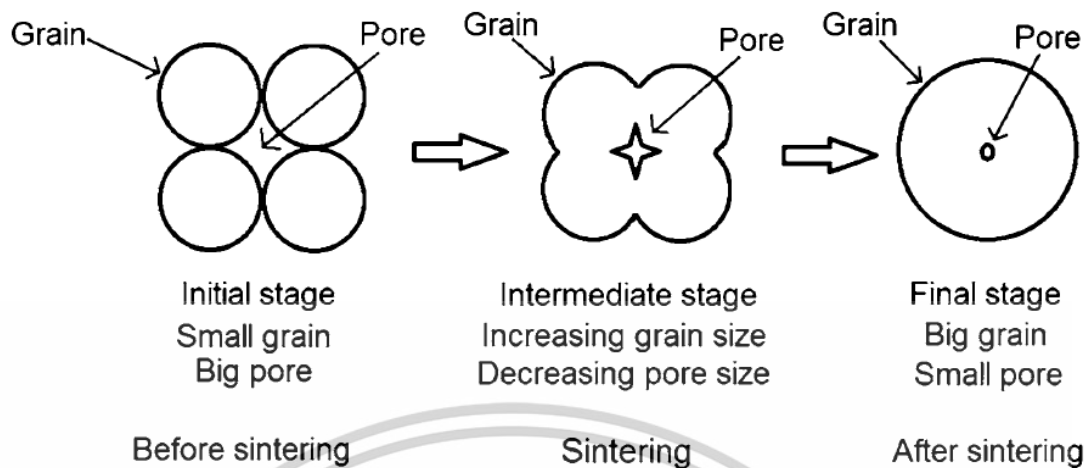


Figure 2.4 Model explaining the powder particles before and after sintering [15]

2.1.2 Application of iron-based sintered materials

In the powder metallurgy process, different types of based materials, such as iron-based, titanium-based, and aluminum-based, were used based on specific applications. For instance, aluminum-based sintered alloys are used to reduce weight for advanced, high-strength components. Some automotive parts, such as camshaft-bearing caps (Al-Si) and shock absorbers (Al-Fe-Ce), were created from aluminum-based materials [13]. However, aluminum powder is expensive and not desired for general applications, to be precise, automotive parts. Iron-based material (alloy) is an alternative option due to its economy. Specifically, many structural applications in automotive are made from iron-based sintered alloy. Examples include camshafts, connecting rod bearing caps, crankshaft sprockets, and so on. **Figure 2.5** shows the PM part made from iron-based materials. Due to its economic advantage, iron-based sintered alloys are still maintaining their place in powder metallurgy markets.

2.2 Phase Transformation Theory

To understand the research concept, a basic understanding of phase transformation is required. The iron-carbon diagram is the fundamental diagram describing the phase transformation of iron based on temperature and carbon concentration. This diagram is suitable for a basic understanding before describing other heat treatment diagrams. In this diagram, the products of austenite (γ) such as

ferrite (α) phase, cementite (Fe_3C) and pearlite are discussed. A more theoretical approach has been developed for more practical use.

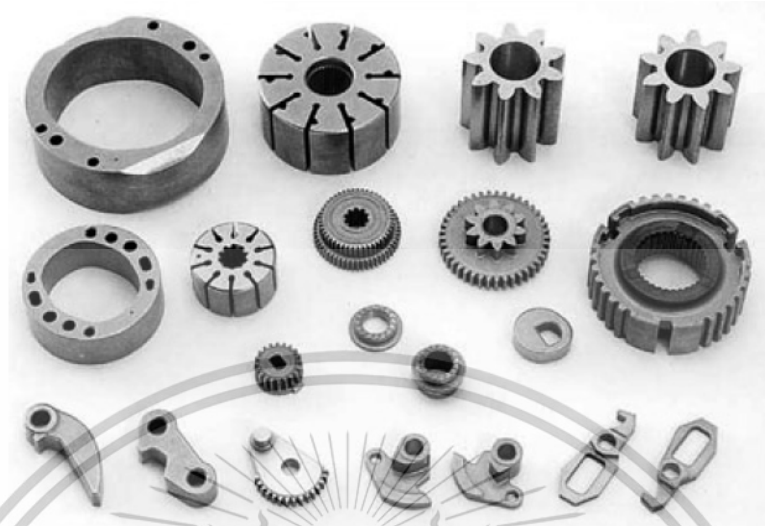


Figure 2.5 PM structural products made from iron-based material [12]

Time-temperature and continuous cooling transformation are transformation diagrams based on temperature and holding time Both TTT and CCT diagrams are more suitable for explaining the manufacturing process of steel. However, both TTT and CCT diagrams are not as general as the Iron-Carbon diagram. They are specifically designed for a specific type of steel. All three diagrams are explained in the following sections.

2.2.1 Iron-carbon phase diagram (Fe-C diagram)

The Iron-carbon phase diagram is a diagram that describes the phase transformation of the iron-carbon system in the equilibrium state. The Fe-C diagram, depicted in **Figure 2.6**, illustrates phase transformation as a function of temperature and carbon concentration. Alloys with C content up to 2.0 wt.% are classified as steels, while alloys with C content greater than 2.0 wt.% are classified as cast irons [16]. Three invariant reactions in the Fe-C diagram are called peritectic, eutectic, and eutectoid. The important reaction is the eutectoid reaction, which affects both cast iron and steel. Alloys with a C content greater than 2.0 wt.% are not discussed here. In the eutectoid reaction, two distinct reactions are classified based on carbon content at 0.8 wt.%. Reactions in alloys with carbon content from 0 to 0.8 wt.% (0–0.8 wt.%) are called hypoeutectoid reactions, while reactions in alloys with carbon content from 0.8 to 2.0 wt.% are called hypereutectoid reactions.

This material is reserved for educational use only, not allowed for commercial use.

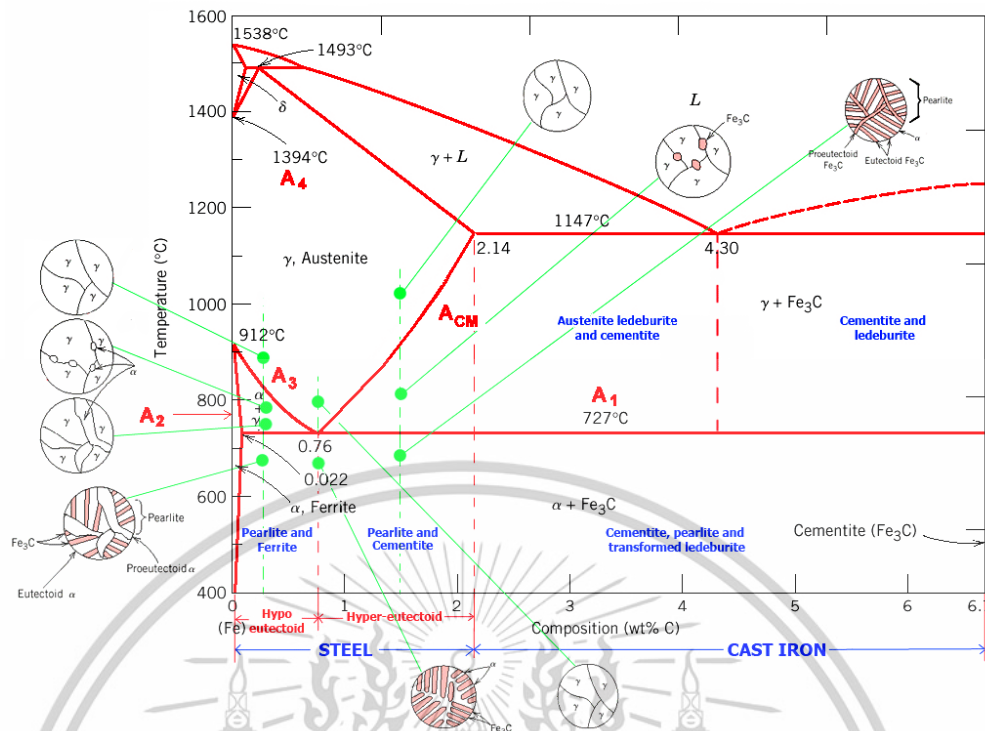


Figure 2.6 Fe-C phase diagram [17]

Since the studied sintered alloys contain 1.2 wt.% of C, the change in microstructure at this mentioned carbon content should be explained using this diagram. At 1.2 wt.% carbon, the microstructure is fully in the austenite phase after heating up to around 1200°C. Upon cooling, the cementite phase (Fe_3C) starts to form when steel is cooled below the A_{CM} line and upper A_1 line. This cementite is called proeutectoid cementite. As steel continues to cool below the A_1 line, the remaining austenite is transformed to pearlite due to a eutectoid reaction. Pearlite is a mixture of ferrite and cementite. As a result, hypereutectoid steels consist of proeutectoid cementite and pearlite.

2.2.2 Time temperature transformation

Time-temperature transformation (TTT), also known as isothermal transformation, is the transformation diagram explaining the transformation for a specific product as a function of temperature and time. Considering TTT diagram is unlike the Fe-C diagram since the Fe-C diagram only explains the transformation of carbon steels under equilibrium conditions, while TTT describes phase transformation

under non-equilibrium conditions. Some applications of TTT diagrams include martempering, austempering, isothermal annealing, and patenting.

Before explaining the TTT diagram, it would be better to clarify the difference between TTT and CCT diagrams since both of them are often confusing. **Figure 2.7** portrays the precise representation of phase transformation, which is accomplished with time-temperature transformation and continuous cooling transformation. As can be seen from **Figure 2.7**, as the transformation temperature decreases, phases such as pearlite and bainite are formed from the parent austenite phase. However, only pearlite and martensite are formed from parent austenite as the cooling rate increases, according to CCT or IT.

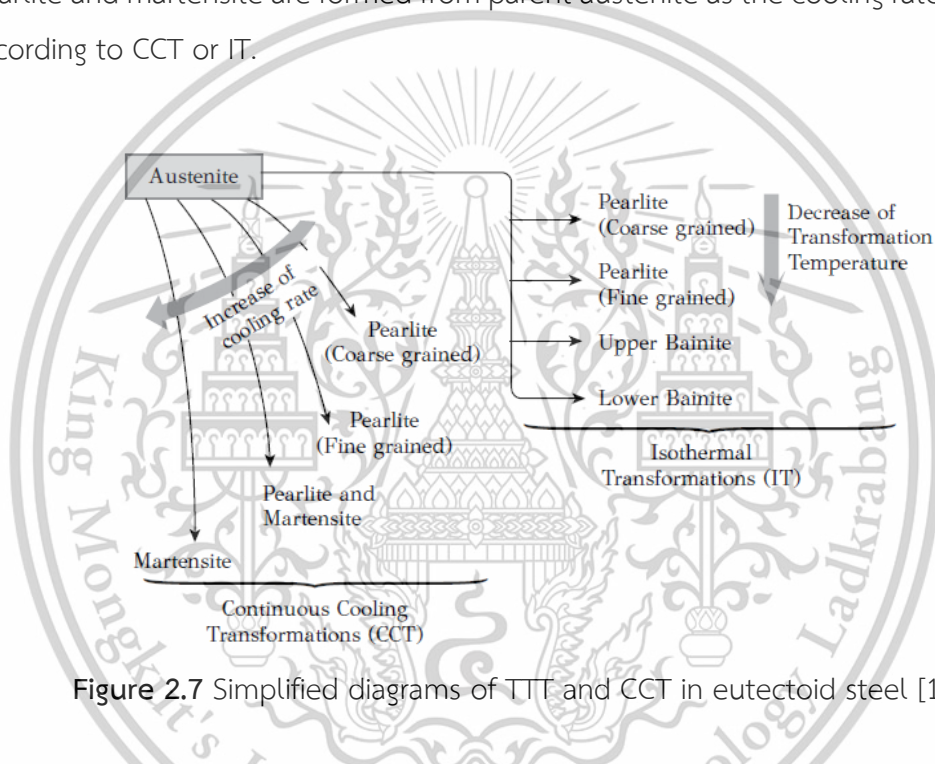


Figure 2.7 Simplified diagrams of TTT and CCT in eutectoid steel [16]

Figure 2.8 below shows a TTT diagram of eutectoid steel. The TTT curve has the characteristic of a "C" shape because the driving force is limited at higher temperatures, whereas mobility is limited at low temperatures [18]. Two horizontal lines are martensite start and finish temperatures (M_s and M_f), while the inner C curve and outer C curve represent the start and finish of transformation, respectively. The turning point of pearlite and bainite starts at the "nose" point. The upper part of the nose is the start and finish of the pearlite transformation, while the lower part is the start and finish of the bainite transformation. The dotted line represents 50% of the transformation, which means the austenite phase is still present during the transformation of either pearlite or bainite. When steel is cooled to martensite start

temperature, martensite starts to form until martensite finish temperature. This martensite is not formed by TTT but by CCT from M_s to M_f temperatures. CCT is explained in the following section.

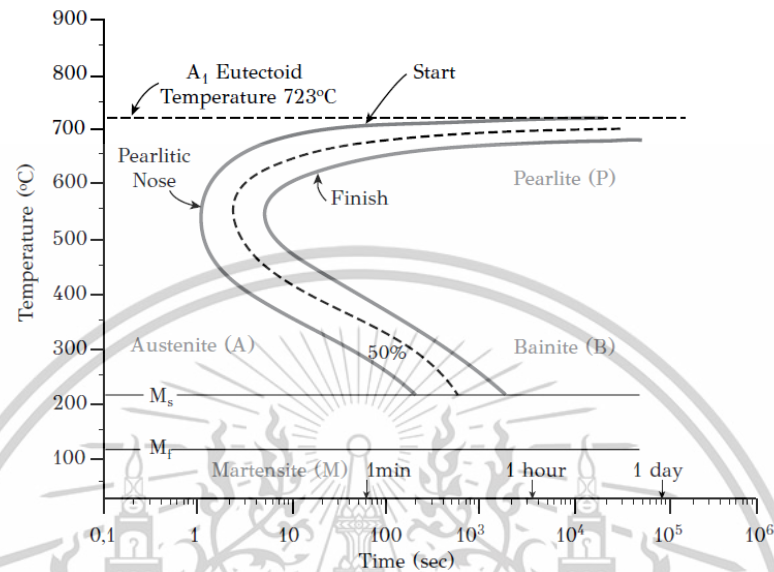


Figure 2.8 Time temperature transformation diagram for a eutectoid steel [16]

2.2.3 Continuous cooling diagram

Continuous cooling transformation (CCT) diagram represents the evolution of transformation that occurs during continuous cooling. Most heat treatments applied to steel include austenitizing followed by continuous cooling at different rates [17]. To better understand certain differences between TTT and CCT, both diagrams are depicted in **Figure 2.9**. The figure shows CCT and TTT for eutectoid steel with three different cooling rates.

Three specimens with three different cooling rates are presented in **Figure 2.9**. Specimen 1 has the lowest cooling rate, and the cooling curve of specimen 1 crosses both the start and finish curves of pearlite transformation. This results in all austenite transforming into pearlite. Specimen 2 has a higher cooling rate than specimen 1. Its cooling curve crosses the start curve of pearlite, but it does not cross the finish curve. This means pearlite forms during cooling from point E to point F and no bainite forms during cooling from point F to point G due to the short transformation time in the bainite region. This means the final microstructure consists of pearlite and martensite.

Finally, specimen 3 is cooled at a sufficiently high rate. The austenite is fully transformed into martensite. It is noted that the CCT diagram of the eutectoid steel does not predict bainite formation.

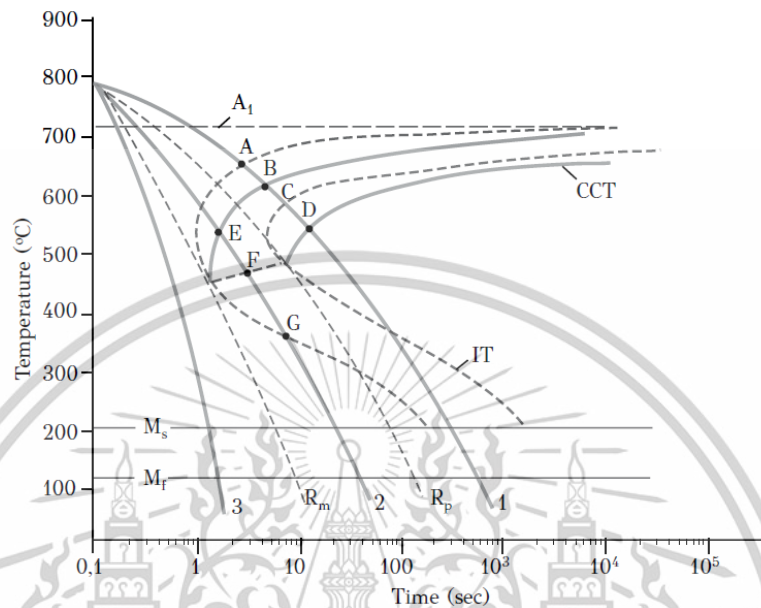


Figure 2.9 CCT and TTT diagrams for a eutectoid steel with critical cooling rate [16]

Figure 2.10 further explains the application of the CCT diagram. Four specimens of eutectoid steels are cooled at different rates. Four different types of cooling rates are illustrated in Figure 2.10. As can be seen from this figure, different microstructures are obtained at different cooling rates.

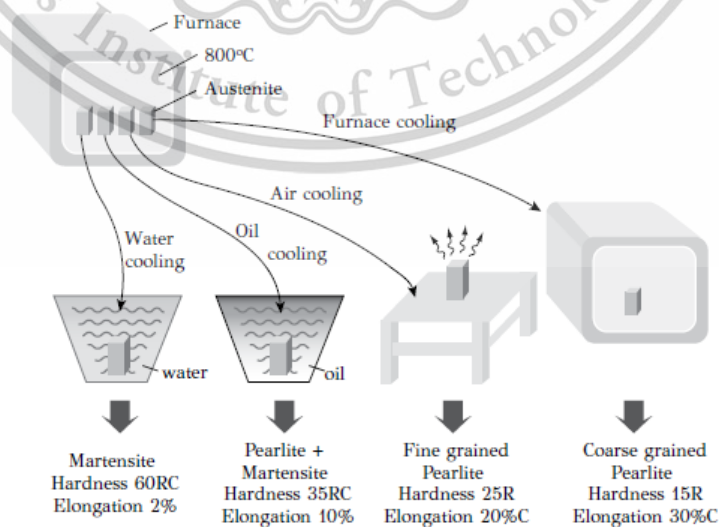


Figure 2.10 Four specimens of eutectoid steel cooled at different rates [16]

This material is reserved for educational use only, not allowed for commercial use.

2.3 Overview of Microstructure in Steel and Alloys

In general, steel and alloys typically contain some of the following phases in their microstructure: ferrite, pearlite, martensite, bainite, and austenite (retained austenite) phases. All these phases are the products of the phase transformation of the parent austenite phase. Austenite has a cubic closed-packed microstructure, also known as the face center cubic structure (FCC) [18]. The crystal structure, morphology, and benefits of each phase are briefly described in the following section.

2.3.1 Ferrite phase

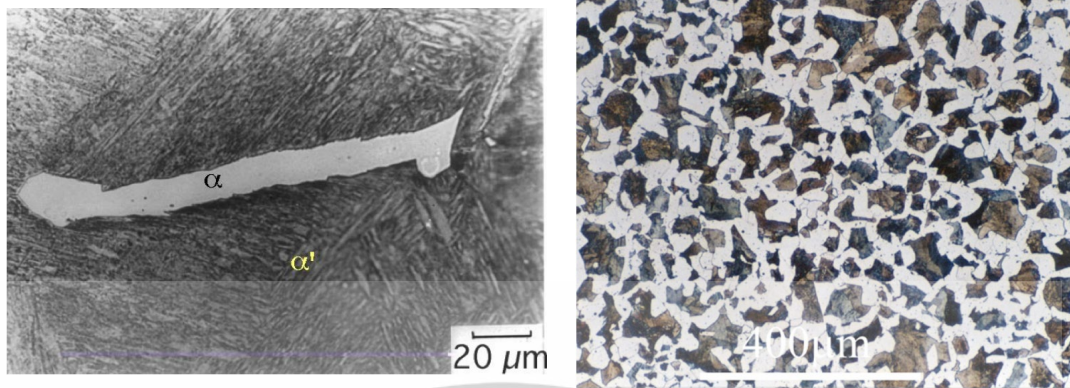
Ferrite, denoted as α , is the first product of parent austenite upon cooling. It has a body-center cubic crystal structure (BCC). Ferrite is classified into different types depending on the atomic transformation mechanism and its nucleation area. Four types of ferrites are allotriomorphic ferrite, idiomorphic ferrite, Widmanstätten ferrite, and acicular ferrite. More details on each type of ferrite can be found in this source [19]. Ferrite is commonly reflected as a white area under the optical microscope.

Figure 2.11 shows OM images that contain ferrite phase (allotriomorphic ferrite) along with other phases (martensite and pearlite phases). **Figure 2.11a** shows the ferrite (displayed as white) area with martensite in a sample that is partially transformed into ferrite and then quenched to obtain martensitic transformation for the remaining austenite. **Figure 2.11b** illustrates the ferrite phase (white area) and pearlite phase (dark area) in Fe-0.4C steel. It is worth mentioning that the ferrite phase acts as a soft phase which is good for tensile strength and ductility but not good for hardness.

2.3.2 Pearlite phase

Pearlite is a mixture of two phases: cementite and ferrite. It exhibits a lamellar morphology with a sequential plate or lamella of cementite and ferrite [16]. Two types of pearlites are coarse and fine pearlites. Coarse pearlite is formed at high temperatures (just below eutectoid temperature), while fine pearlite is formed at low temperatures (in the vicinity of 540°C). The coarse and fine structure of pearlite affects its mechanical properties. Fine pearlite shows a greater hardness than coarse pearlite due to the high density of the cementite and ferrite interface. An example of full pearlite formation in

a microstructure is depicted in **Figure 2.12**.



(a) Ferrite in quenched steel

(b) Ferrite in a Fe-0.4C steel

Figure 2.11 Appearance of ferrite phase in quenched steel and Fe-0.4C steel [20]

2.3.3 Bainite phase

Bainite phase is the phase in the microstructure that consists of a non-lamellar mixture of ferrite and carbides [20]. Many terms are used to describe bainite morphology, only two terms, lower and upper bainite are described in this study. Bainite exhibits high tensile strength and good hardness. Lower bainite is obtained at relatively low temperatures while upper bainite is obtained at higher temperatures. Both bainites form as aggregates of laths or plates of ferrite [20]. The main difference between them is the precipitation of carbide.

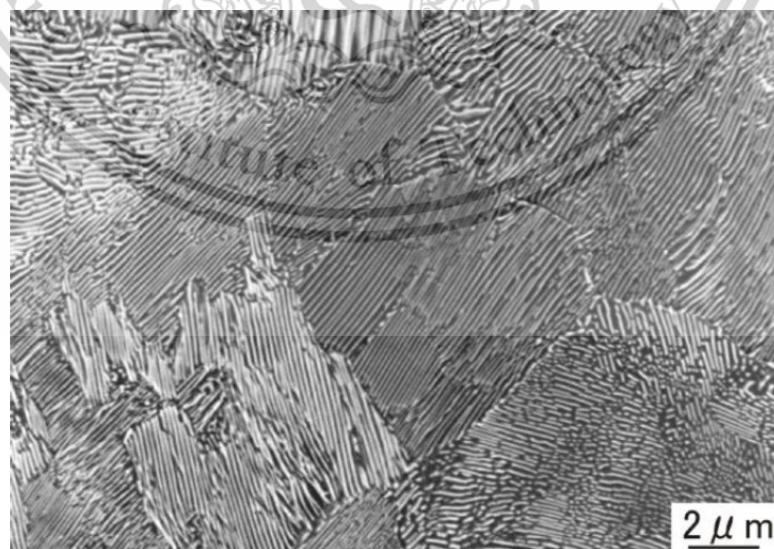


Figure 2.12 OM image of pearlite [19]

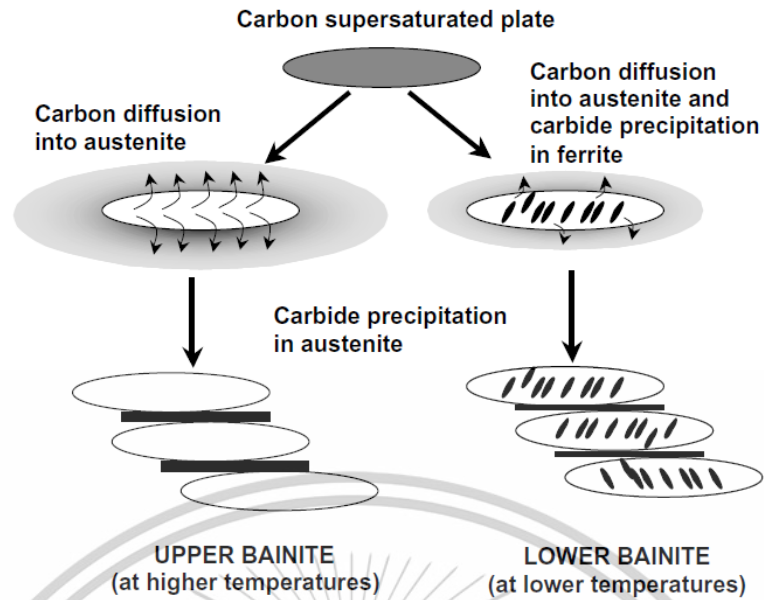


Figure 2.13 Schematic representation of upper and lower bainite [21]

Figure 2.13 shows the precipitation difference between lower and upper bainite. Moreover, a clear difference in mechanical properties is observed between lower and upper bainite. Optical microscope images and transmission electron microscopy images of bainite formation are shown in **Figure 2.14**. These images were observed by F.G Caballero et al. in high carbon high silicon steel [22]. The images were obtained via isothermal transformation at 200°C. However, lower and upper bainite were not elaborated in this study.

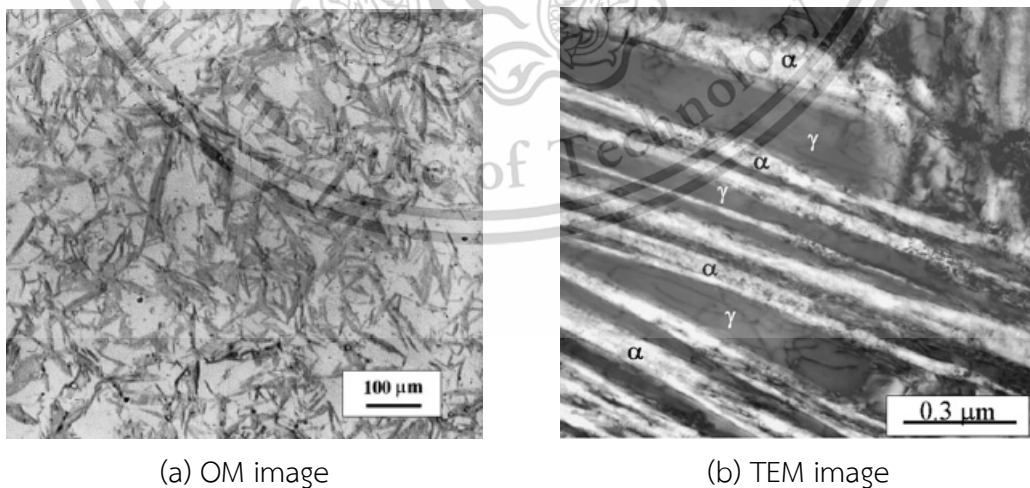


Figure 2.14 OM and TEM micrograph of bainite obtained at 200 °C [22]

2.3.4 Martensite phase

Martensite is a supersaturated solid solution of carbon in ferrite. It starts to form when austenite is cooled to a temperature below M_s temperature. Martensite has a body-center tetragonal (BCT) structure. It forms by a displacive transformation mechanism. Martensite is classified into different types such as lath martensite, lenticula, and thin plate. **Figure 2.15** shows a plate of martensite in a nickel-rich alloy and a low-alloy steel.

Martensite has a very high hardness value; however, it exhibits a low elongation value since its transformation mechanism is susceptible to impurity embrittlement [19].

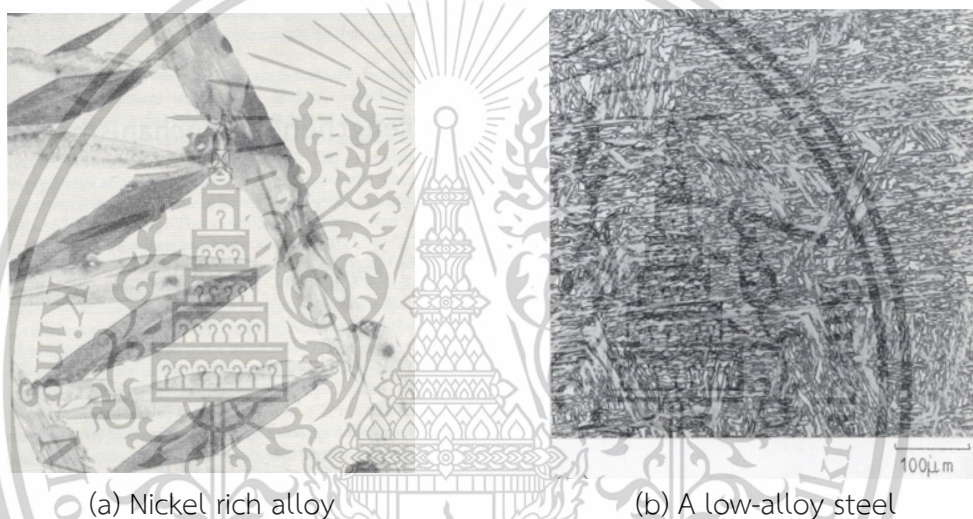


Figure 2.15 OM image of plate shape of martensite [19]

2.4 Influence of Alloying Elements

Besides the most influential element carbon in steel, other alloying elements are intentionally added for many reasons. The role of alloying elements is hardly characterized due to several complexity factors. Alloying elements influence the rate of phase transformation, phase stability, solid solubility of other elements, deformation and strengthening mechanism, etc. Only alloying elements that existed in these studied sintered alloys are discussed in this section. However, the effect of alloying elements on typical steel and sintered material could be different due to different processing techniques. The first subsection briefly explains the effect of alloying elements on typical steel while the second subsection discusses the influence of

alloying elements on this studied sintered alloy with past and recent research papers on iron-sintered alloy.

2.4.1 Influence of alloying elements on eutectoid point (phase stabilization)

The most commonly known requirements of alloying elements in steel are deoxidation, stabilization of austenite, grain refinement, hardenability, carbide former, and oxidation and corrosion resistance. Regarding phase stabilization, the alloying element can influence either austenite or ferrite stabilization:

- Austenite Stabilizers: alloying elements include C, Ni, Mn, and Co, their addition expands the austenite field in the phase diagram.
- Ferrite Stabilizers: alloying elements include Si, Al, Mo, addition of these element restricts the austenite field in the phase diagram.

Since both phase stabilizer can widen their own phase field, the eutectoid temperature in the Fe-C diagram is also strongly influenced. Austenite stabilizers lower eutectoid temperature, therefore widening the temperature range in which austenite is stable. In contrast, ferrite stabilizers raise the eutectoid temperature, thereby restricting the austenite phase field. **Figure 2.16** below shows the effect of Si on eutectoid temperature [23]. For the same carbon content, the gamma loop of steel alloyed are varied with different silicon percentages. The eutectoid point appears at higher temperatures and lower carbon contents when the silicon percentage increases in the alloy.

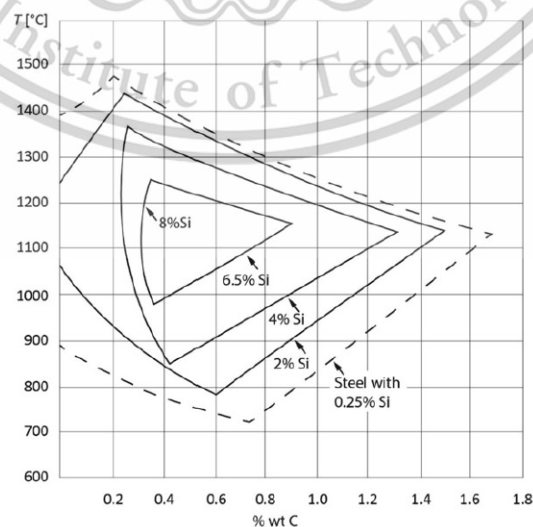


Figure 2.16 Simplified sections of the Fe-C-Si diagram [23]

This material is reserved for educational use only, not allowed for commercial use.

2.4.2 Influence of alloying elements on martensite transformation

In steel, martensitic transformation takes place during the rapid cooling of austenite, so-called quenching in the heat treatment term. Martensite begins to form at M_s (martensite start temperature) and ends at M_f (martensite finish temperature). Normally, martensite starts to form at a temperature around 300°C . However, martensitic transformation is strongly dependent on the addition of alloying elements. Most alloying elements lower martensite start temperature except Co and Al as depicted in **Figure 2.17**.

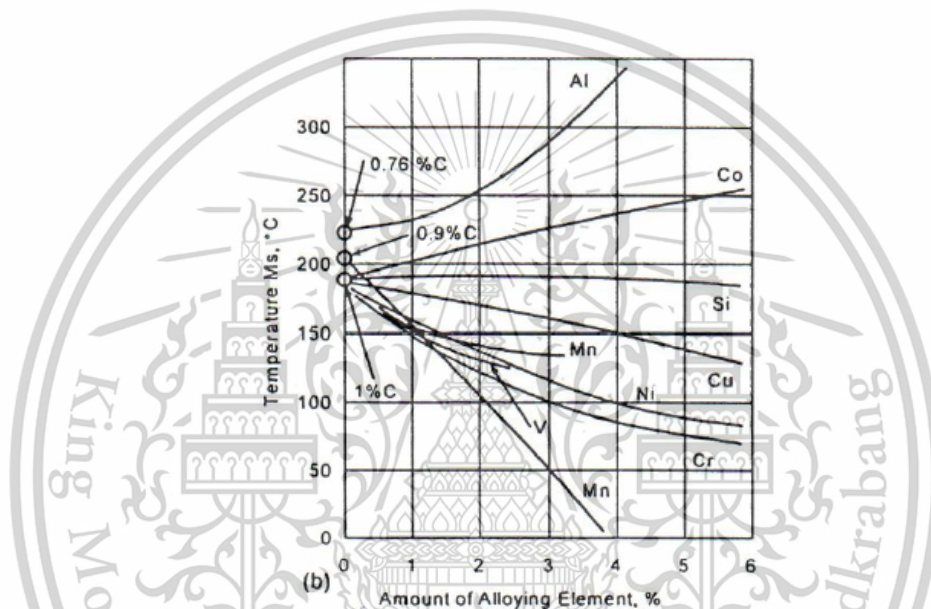


Figure 2.17 Effect of alloying elements on martensite start temperature [24]

2.4.3 Influence of alloying elements on bainite transformation

In carbon steels, the bainite transformation (stage II transformation) occurs between 500 and 250°C beneath the precipitation curve of undercooled austenite (C curve). It takes place between the transitions of pearlite and martensite. The transformation and microstructure formation produced are identical to those seen during the diffusion pearlite or diffusionless martensite transformation. Alloying elements influence the kinetics of bainite transformation, although to a lower extent compared to the case of pearlite transformation. For instance, bainite transformation is basically delayed at high temperatures, whereas austenite transformation takes place almost entirely at lower temperatures in the case of steel alloyed with Ni or Mn.

For high-carbon steels with 1.0 wt.% C, **Figure 2.18** illustrates the effect of

different alloying elements regarding these parameters. As can be shown, Mn and Cr have a significant impact on the kinetics of the bainite transformation by lengthening the incubation period, decreasing the lowest temperature at which austenite remains stable, and raising the maximum transformation rate. At the same time, while alloying with Mo and W significantly slows down the pearlite transition, it has no impact on the kinetics of the bainite transformation [25].

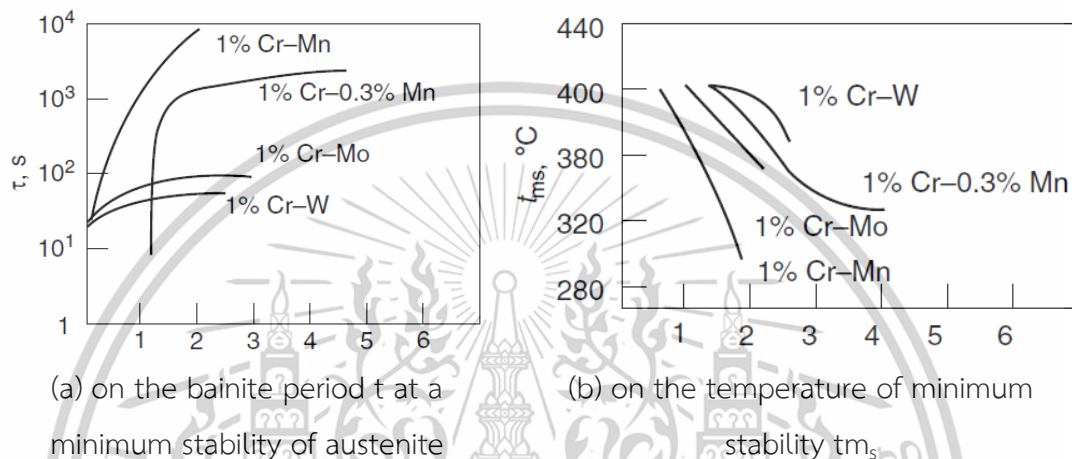


Figure 2.18 The influence of Cr, Mo, W, and Mn on bainite transformation [25]

2.5 Effect of Cobalt (Co) Addition

Generally, cobalt (Co) is an element that is known to increase martensite start temperature along with Aluminum (Al). Cobalt became popular among researchers during the development of nanostructure bainite. Co is known to shift the TTT curve to the left. The influence of Co and Al on bainite transformation has been observed through several studies. However, the significant effects of Co and Al on steel are varied depending on different types of steel. Some studies suggest that the addition of Co increases mechanical properties while some suggest that Co and the combination of Co and Al addition does not improve any mechanical properties. Both positive and negative effects of Co are discussed accordingly in this section.

2.5.1 Effect of cobalt on bainitic transformation

Normally, bainite can take up to 2 days to 60 days to complete transformation within 125-325°C [11]. Transformation can be accelerated by increasing free energy change accompanying the austenite to ferrite transformation. It is well known that both

cobalt and aluminum increase free energy change. Therefore, Co and Al were used to accelerate bainite transformation in steel. Free energy in alloys with and without Co and Al-containing was confirmed in a study by C-Garcia Mateo et al. [11]. **Figure 2.19** illustrates the difference in free energy between alloys with and without Co and Al. Alloy 1 contains no Co and Al, while alloy 2 contains 1.54 wt.% of Co, and alloy 3 contains both Co (1.60 wt.%) and Al (0.99 wt.%).

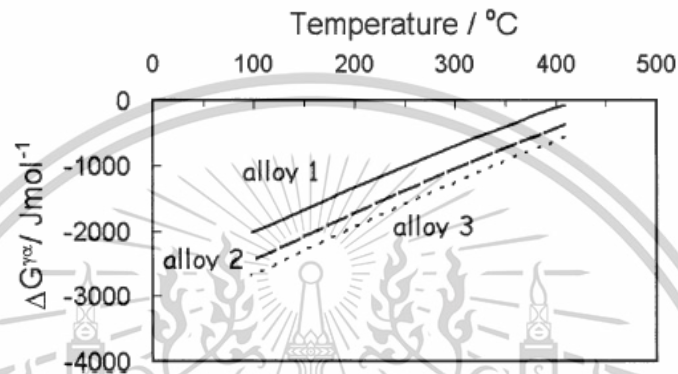


Figure 2.19 Free energy change as function of temperature [11]

According to C-Garcia Mateo et al., Co has a considerable effect on bainite transformation in high-carbon steel. The acceleration of bainite transformation was observed in Co and a combination of Co and Al alloys. Due to the rate of acceleration, bainitic ferrite fraction is also increased. **Figure 2.20** shows the time taken for bainite transformation. As can be seen, Co has a significant effect on the rate of transformation and is even greater for alloy with a combination of Co and Al.

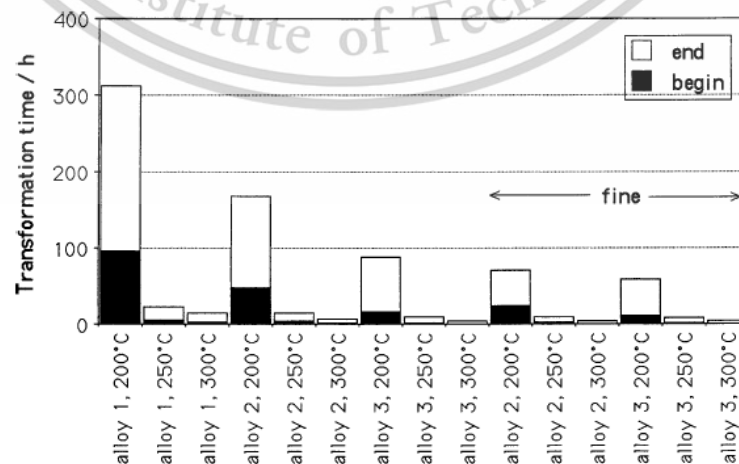


Figure 2.20 Transformation time of bainite transformation [11]

The black area and white area of the bar chart identify the start and end of the transformation accordingly. Alloy with Co and Al addition (alloy 3) shows an increase in transformation rate. The time taken for this studied alloy to complete bainite transformation is below 100 hours. It is quite significant if compared to alloy without Co and Al addition.

Another effect of cobalt in high-carbon steel is further refining the microstructure due to an increase in driving force. Two benefits are obtained due to this effect. The first benefit is an increase in the formation of bainitic ferrite while a decrease in islands of retained austenite. The second benefit is the refinement of the size of bainitic ferrite plates which are desired for mechanical properties. This refinement is concluded as mainly a consequence of the effect of Co by the author. **Table 2.1** shows the summary of quantitative experimental data of three types of alloys with and without Co and Al addition. Each type of alloy is designed to transform at different temperatures. This table shows evidence of the benefits of Co addition.

Table 2.1 Summary of quantitative experimental data, V_B is bainitic ferrite fraction, reproduced from [11].

	Temperature / °C	Time / h	Thickness / nm	Error / nm	V_B
Alloy 1	300	240	124	4	0.55
Alloy 1	200	363	35	1.3	0.69
Alloy 2 (Co)	300	24	106	10	0.67
Alloy 2 (Co)	200	216	38	2	0.79
Alloy 3 (Co+Al)	300	8	57	4	0.66
Alloy 3 (Co+Al)	200	216	40	3.6	0.78

Alloy 1 transform at 300 °C has a volume fraction of bainitic ferrite 0.55 which is higher than alloy 1 transform at the same temperature, volume fraction of only 0.67. Moreover, the thickness of alloy 2 is smaller than the thickness of alloy 1. However, an interesting point is the transformation time, at 200 °C transformation temperature, the bainitic transformation time of alloy with Co is surprisingly the same with alloy 3

which contains both Co and Al. This means that only Co addition is needed for acceleration of bainitic transformation below 300 °C.

Another study was conducted by the International Research Institute for Steel Technology to confirm the influence of Co and Al on bainitic transformation in super bainitic steels. Two alloy steels with Co and Al were investigated. Alloy 1 contains only Al while Alloy 2 contains both Co and Al. The effect of Co and Al addition on shifting TTT curves were calculated by Feng Hu et al. [26]. **Figure 2.21** shows the shifting TTT curves of alloy 1 and alloy 2 on heat treatment of bainitic steel.

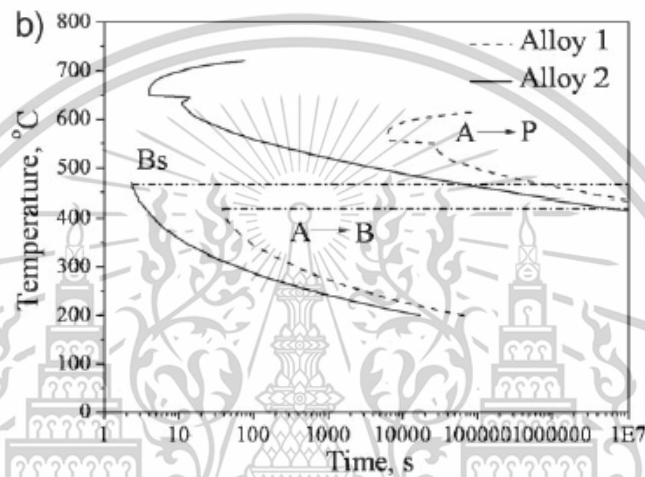


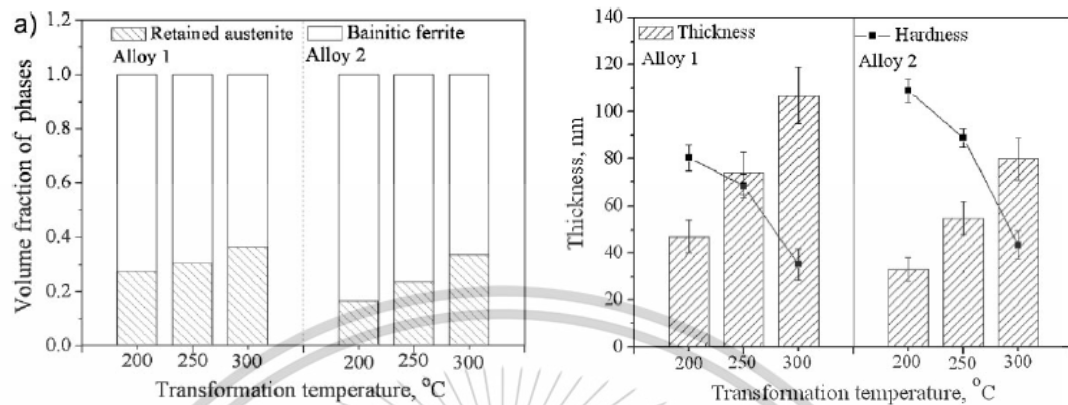
Figure 2.21 Effect of the Co and Al addition on shifting TTT curves [26]

The volume fraction of the bainitic ferrite of alloy 2 is higher than the volume fraction of the bainitic ferrite of alloy 1 as observed in this study [26]. Nevertheless, the thickness of the bainitic ferrite plate is also reduced as observed in alloy 2. The reduction of thickness is mainly the combination effect of Co and Al. **Figure 2.22** shows both the increase in the fraction of bainitic ferrite and the reduction of the thickness of bainitic ferrite plate respectively.

2.5.2 Influence of cobalt on mechanical properties of steels

Generally, many studies on the influence of Co were conducted on bainitic steel or bainitic-related steel. Bainitic steels have an extraordinary property. It has a very high tensile strength which exhibits 2GPa, a hardness at 600-670HV, and toughness in excess of 30-40MPa m^{1/2} as reported by F.G Caballero et al. [10]. The extraordinary of bainitic steel is heavily related to the microstructure of bainite or so-called bainitic ferrite. The goal of achieving the nanostructure of bainitic ferrite leads to the addition

of Co or Al. Since bainitic steel already exhibits a very high tensile strength, the influence of Co on mechanical properties is not widely investigated.



(a) Volume fraction of phase (b) Thickness of bainitic ferrite plate

Figure 2.22 Volume fraction and thickness of the bainitic ferrite [26]

In this section, the influence of Co on the mechanical properties of steel is discussed. Co-addition can have a positive or negative effect on the mechanical properties of steels because different types of processing methods can affect the influence of Co-addition. Two factors were obtained from Co addition on studied high carbon, silicon-rich steels with bainitic microstructure. Those factors are the amount of bainitic ferrite and the presence of retained austenite. These two factors have a strong effect on the tensile properties of steels with bainitic microstructure according to Carlos Garcia-Mateo and Francisca G. Caballero [10]. Alloy with 1.51 wt.% of Co content shows better tensile properties compare to alloy with combination of Co and Al when isothermal transformation temperature at 250°C and 300°C. In contrast, an alloy with a combination of Co and Al exhibits better tensile properties when isothermal transformation temperature at 200°C. The total elongation of both alloys decreases as tensile strength increases. It is concluded by the authors that the main strengthening mechanism is the thickness of the ferrite plate while ductility might be dependent on the fraction of retained austenite and its stability. Alloys with a high fraction of retained austenite show the best results in terms of elongation value and this phase is also stated to be the softest phase in the microstructure [10]. **Figure 2.23** illustrates the engineering stress-strain curve of both alloys at room temperature. So, Co addition can increase the tensile properties of steel with bainitic microstructure as observed in the

This material is reserved for educational use only, not allowed for commercial use.

study. A recent study (in 2021) on the effect of Co addition on the mechanical properties of new generation 3Cr-3W and 5Cr-3W steels was investigated by Gokhan Arici et al. [27].

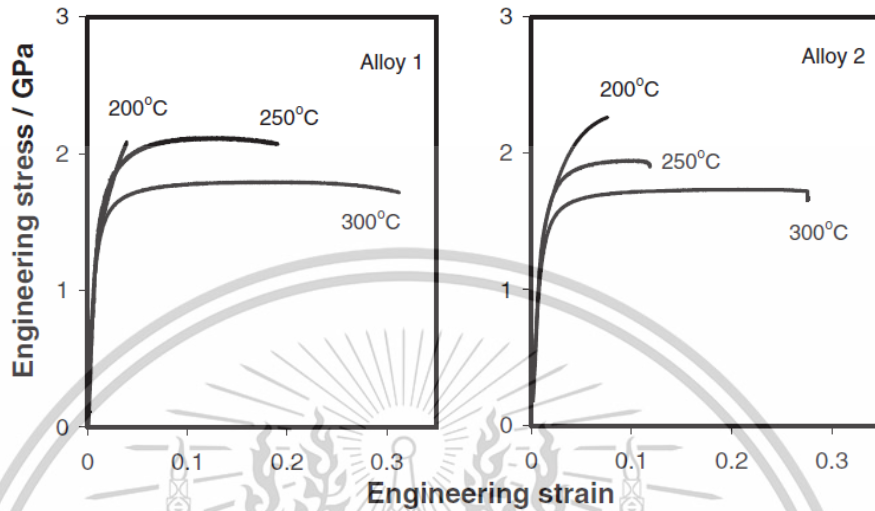


Figure 2.23 Engineering stress strain curve obtained at room temperature [28]

Co content at 0%, 0.5%, 1.5%, 3%, and 4.5% wt. were added to new generation steels produced by casting and hot rolling. It is reported that Co increased the mechanical properties of 3Cr-3W and 5Cr-3W to a certain extent. Gokhan Arici comments that the addition of Co increases tensile strength and hardness to a specific rate, however, further addition of Co more than 3.0 wt.% reduces the strength slightly in 3Cr-3W steel. This reduction of tensile strength might be attributed to the increase of ferrite phase in 3Cr-3W steel with Co content of more than 3.0 wt.% [27]. Slightly different results of tensile strength were observed on 5Cr-3W steel. Co addition more than 3.0wt.% does not reduce the tensile strength of 5Cr-3W steel nor increase the tensile strength. Another negative effect of Co is the reduction of toughness. The impact energy of both steels is decreased as Co increases. Hardness is also sensitive in this study. However, the ductility or total elongation value of both steels is not reported by the authors. The tensile strength and hardness of both steels are depicted in **Figure 2.24** and **Figure 2.25** accordingly.

Another research by JingYang et al. suggests that although Co addition has a considerable effect on mechanical properties, Al addition shows better results on steel

produced by casting and austempering [29]. Co content at 1.78 wt.% was added and varied in the austempering process in his study.

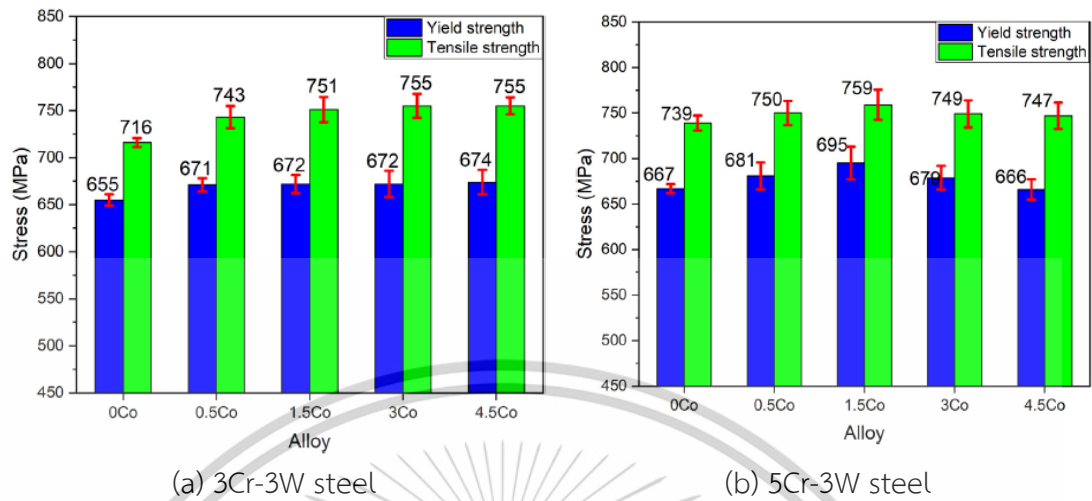


Figure 2.24 Tensile strength and yield strength versus Co content [27]

However, the reference steel without Co and Al is not provided by the author. A study on the effect of Al addition on strength carbide-free bainitic steels by Jun-yu Tian et al. comments that Al addition has a different effect on heat treatment methods. For CCP treatment, Al addition had no strong effect on the tensile properties of high-strength carbide-free bainitic steels while Al addition significantly decreased tensile strength and moderately increased total elongation in the case of ITP treatment.

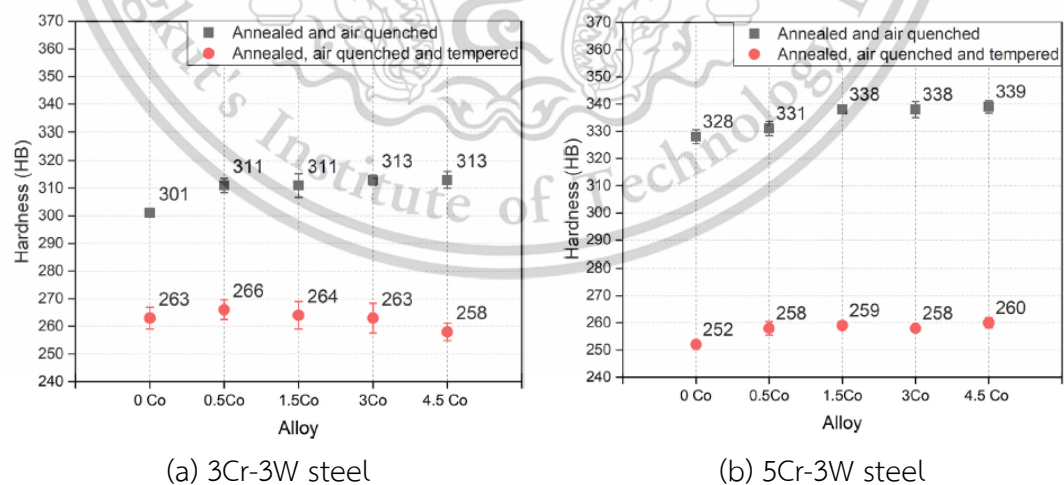


Figure 2.25 Hardness of both alloys versus Co content [27]

2.6 Overview of Tribological Characterization

Besides exhibiting good mechanical properties, materials also need to have good tribological properties according to their specific application. Tribology deals with the friction, wear rate, and contact mechanism between two or more materials (wear mechanism), etc. Friction coefficient, wear rates, and wear mechanisms are important parameters in tribology. For some applications, such as brake discs, materials should have a high friction coefficient, while others require a low friction coefficient, such as transmission parts. The friction coefficient can be determined by wear testing. There are different types of wear testing, such as pin-on-disc sliding wear, reciprocating sliding wear, fretting wear, etc. In this literature, only the pin-on-disc sliding wear test is described in the following section, followed by the wear mode or wear mechanism.

2.6.1 Pin-on-disc dry sliding wear test

In wear testing, the pin-on-disc dry sliding test is one of the most widely used due to its simplicity in test apparatus. The test includes a disc specimen and a pin with a ball at the end of it. Typically, the pin can take any form. A ball pin or lens is used in the "ball on disk" test. The alignment of the pin needs to be set up carefully; otherwise, it will lead to non-uniform wear due to non-uniform loading. The schematic of the pin-on-disc system is illustrated in **Figure 2.26**. The important pin-on-disc test parameters are the normal load (N), sliding speed (m/s), sliding distance (m), pin-end diameter (mm), and track diameter (mm). These parameters can influence the results of tests. Besides these mentioned parameters, the environment, such as temperature and humidity, also affects the test results. All these parameters can be input during the testing. Moreover, tests are carried out under different test standards, such as ASTM G99 and ASTM F732.

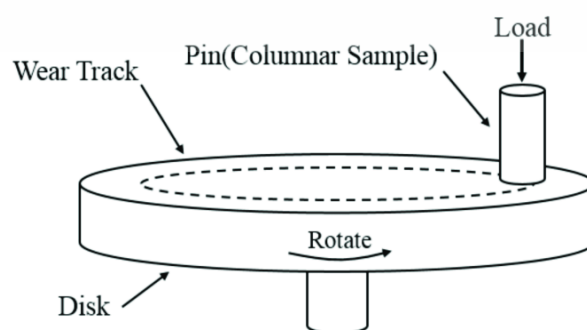


Figure 2.26 Schematic of pin-on-disc dry sliding wear test [30]

This material is reserved for educational use only, not allowed for commercial use.

In this research, a wear test is set up according to ASTM G99 [31]. Force data during testing is obtained through the test system. Then, the friction coefficient is determined using the formula given in ASTM G99.

2.6.2 Wear rate of materials

Wear rate can be classified as the amount of material removed per unit of time due to friction. Wear rate can describe how much surface of a tested specimen is being removed in some specific condition. It can also be used to observe how materials respond when the surface of the material is removed by friction. Alongside the SEM image of the worn surface, the wear behavior of materials can be discussed. To determine the wear rate of materials, volume loss must be determined. Normally, the mass of the tested specimen is lost due to the counterpart material. So, by measuring the weight of the test specimen before and after the test, volume loss can be determined. However, mass loss in some test specimens is too small to be measured with digital measurement. This is due to the very high strength of the interface of the specimen surface, for example, steel and sintered alloy.

In the case of metals and alloys, the wear rate on such surfaces is quite high because polished metal surfaces are extremely prone to friction and wear. The characteristics of the materials or the kind of mating material affect how quickly they wear. The contamination that forms on the surface of the material creates chemical coatings that lower adhesion and hence lower wear rates. Moreover, in the context of metals, the wear rate is affected by a number of variables in addition to their chemical and physical properties [32]. The testing conditions, such as applied load, sliding speed, and temperature, have a significant influence on the wear rate of metals. For example, the effect of sliding speed and applied load is that if the sliding speed is increased, the interface temperature increases, leading to a decrease in wear rate at the interface.

2.6.3 Wear mode of materials

In addition to wear rate, wear mode or wear mechanism is very important in the study of tribology. Wear mode commonly describes how the surface of a material is removed due to sliding movement between two solid surfaces. Wear can be moderate or severe, depending on the normal load and sliding distance. Moderate or

mild wear is defined as worn surfaces that contain smooth and tiny wear particles. Severe wear, on the other hand, can be described as a roughened, damaged surface with a huge amount of wear debris that is visible to the human eye. The components' service life is short due to severe wear. Thus, applying a lubricant and modifying the component's surface can both extend the component's life cycle [33].

Due to the complexity of wear, wear modes or mechanisms can be classified into four main types: abrasive wear, adhesive wear, corrosive wear, and delamination or fatigue wear. These four types are commonly found in metals and alloys. Each type of wear mode is briefly explained below:

- Abrasive wear: Abrasive wear occurs when a hard, rough surface moves across a smooth surface. According to ASTM International, it is characterized as material loss brought on by hard particles that push against and slide over a solid surface [34]. Abrasive can be further divided into two types of abrasive, namely two-body and three-body abrasive wear.
- Adhesive wear: Adhesive wear is the unintended transfer of material compounds and wear debris from one surface to another when the surfaces are in frictional contact. It can be formed in two different ways: by the growth or fragmentation of wear particles or the plastic deformation of microcracks followed by asperity [33], [35].
- Corrosive wear: Whenever a sliding surface is subjected to a corrosive environment and the sliding action repeatedly removes the preventative corrosion product, corrosive wear does actually occur as an indirect wear mechanism. The newly formed surface is thus subject to extra corrosive damage. Nevertheless, corrosion wear might be considered as an accelerated corrosion process.
- Fatigue wear: Fatigue begins with the formation of cracks and fissures on the material's surface; the fracture created on the surface is the consequence of strain induced across the surface owing to external factors such as rolling or sliding on the surface. In the context of metals, fatigue wear is caused by the development of both surface and subsurface fractures, which, after a given number of cycles, result in severe damage.

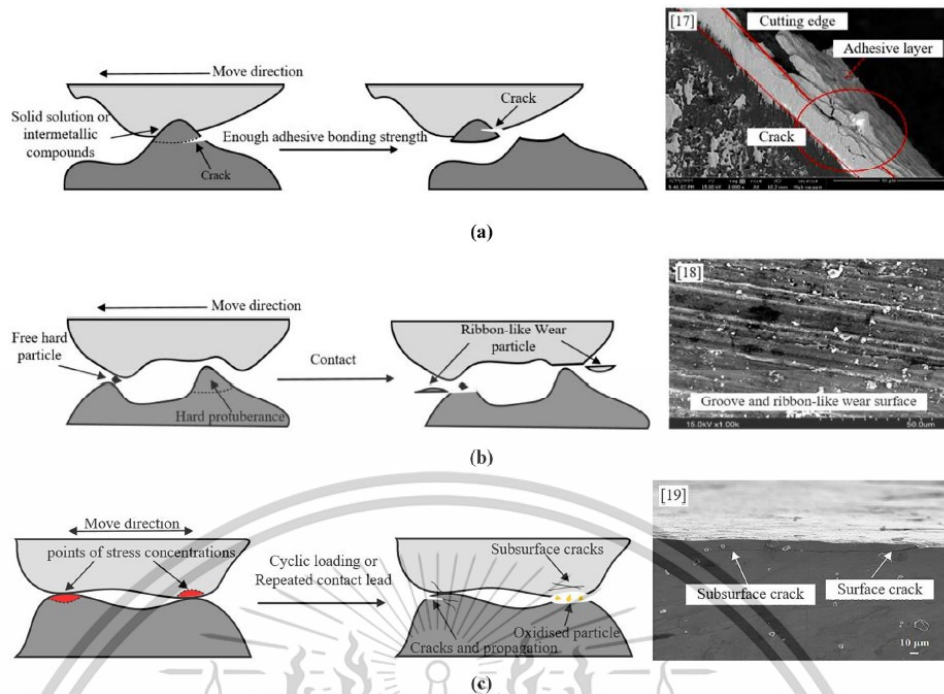


Figure 2.27 Common wear mechanisms: a) adhesive wear, b) abrasive wear and c) fatigue wear [36]

Figure 2.27 below shows some images of most common wear mechanism found in metals and alloys and their SEM of worn surfaces.

2.7 Recent Researches on Sintered Fe-Based Alloys

The development of sintered alloys and/or steels is centered on improving their mechanical properties [5], [6]. Both high strength and high ductility are the main focus among researchers since strength and ductility trade-offs are commonly seen in steels and/or alloys. So, avoiding the strength and ductility dilemma is a very complicated task that requires more expertise and investigation, especially for sintered Fe-base parts. In the case of sintered Fe-base alloys, their elongation or ductility is relatively low (3–4% of tensile strain at break) compared to other base materials, such as aluminum-base or titanium-base alloys. Porosity is the main cause of low elongation values [37]. Different methods, including optimizing sintering temperature, optimizing cooling rate, etc., were used in previous research. It is well known that the strength of a sintered iron (Fe)-based alloy matrix can be improved by sinter hardening, while the ductility can be increased via the transformation-induced plasticity (TRIP) effect. So, by

modifying the final microstructure, one might obtain both high strength and high ductility.

However, the sintering temperature and cooling rate are restricted to values available in industrial sintering furnaces. Some results of elongation values versus tensile strength of sintered Fe-base alloys from recent research are depicted in **Figure 2.28**. It is clearly shown that in order to obtain a very high tensile strength, ductility or elongation needs to be sacrificed. This trade-off phenomenon is commonly observed in sintered steels or alloys. This trade-off phenomenon is a drawback to expanding the application of the sintered P/M industry. More results on mechanical properties from national and international research papers are illustrated in **Table 2.2**. As can be seen from **Table 2.2**, the elongation value is still low despite the efforts of many outstanding researchers.

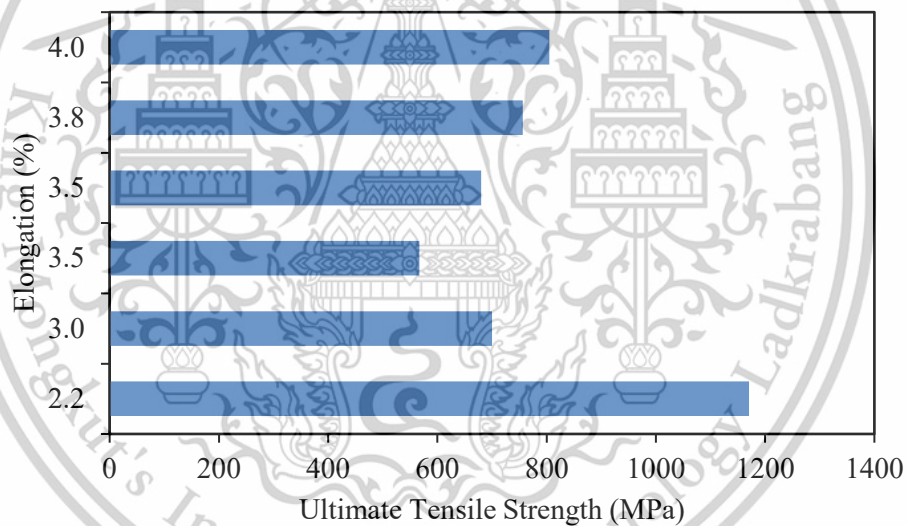


Figure 2.28 UTS versus elongation from recent researches on Fe-base material

Table 2.2 Literature on mechanical properties of sintered Fe-base alloy/steels

Author & Year	Materials (wt.%)	UTS (MPa)	Elongation (%)	Ref.
GŁOWACZ et al., 2019	Fe-1.5Mn-0.60Si-0.80C, 1250°C	726	3.6	[38]
M. Sulowski, 2016	Fe-3Mn-0.6C-0.5Mo-0.03Si, 1220°C NC100.24+Elkem+C-Fe-3Mn-0.8C,1250°C	639 595	2.99 3.80	[39]
Chawla and Deng, 2005	Fe-Mo-Ni, 1120°C	784.4	6.5 ± 0.7	[37]
S. Chakthin et al., 2008	Fe, 1200 °C	224	6.06	[1]
Jinsu You et al. 2021	Fe-5Mo-0.4B-0.8C, 1280°C	< 700	<5	[40]
Wananurut et al., 2015	AstaloyCrM-0.1C, 1250°C	< 400	< 4.5	[41]
Kittikhun et al., 2018	Fe-1.50Mo-4.0SiC, 1250°C	< 700	<2	[3]
Kittikhun et al. 2018	Fe-3.0Cr-0.5Mo-4.0SiC, 1250°C	< 700	<2	[4]
Tiwat et al., 2021	Fe-4.0Ni-0.5Mo-0.2Mn-4.0SiC, 1250°C	1170.5	2.24	[7]
Thunyamon et al., 2021	Fe-1.5Mo-0.15Mn-4.0SiC, 1250 °C	1005.3	3.14	[42]

CHAPTER 3

RESEARCH METHODOLOGY

3.1 Material Preparation

The specimen was prepared from pre-mix powder ATOMET 4801 with 4.0 wt.% SiC and a variable amount of Cobalt (Co). Cobalt was added in different amounts, starting from 0.5 wt.% to 3.0 wt.%. Pre-alloy ATOMET 4801 was used as the base material in this study. The composition and properties of this pre-alloy are shown in the following sections.

3.1.1 Based material

ATOMET 4801 is a pre-mix alloy manufactured by RioTinto Powder Manufacturing Company. It is a highly compressible metal powder produced by the water atomization technique. This pre-alloyed powder already contains 4.0 wt.% of nickel (Ni), which is suitable for high-strength applications. According to some given data, the tensile strength of ATOMET 4801 is around 500 MPa using the described method (sintered in a 90% nitrogen-based atmosphere at 1120°C (2050°F) for 20 minutes at a cooling rate of 0.4°C/s from 650°C (1200°F) to 400°C (750°F). The composition of the pre-alloy ATOMET 4801 is shown below in Table 3.1.

Table 3.1 Composition of ATOMET 4801

Composition (wt.%)						
C	O	S	Mn	Mo	Ni	Fe
0.01	0.15	0.009	0.20	0.50	4.00	Bal.

3.1.2 Addition of alloying elements

Silicon carbide (SiC) and Cobalt (Co) are used as alloying elements in this research. Silicon carbide is known as a reinforcement particle. It can increase the tensile strength of based materials, for example, iron-based materials. On the other hand, Cobalt is used in many different applications, such as gas turbine engines and batteries. Moreover, cobalt is also used as an additional alloying element, mostly in nickel-based alloys. It helps increase the wear and corrosion resistance of the materials. In this study, This material is reserved for educational use only, not allowed for commercial use.

Co is added to the based material ATOMET 4801 to alter its microstructure by influencing the bainite transformation during cooling. The mesh particle sizes of both silicon carbide and cobalt are around 200 to 400 micrometers. **Figure 3.1** shows the alloying powder of SiC and Co.

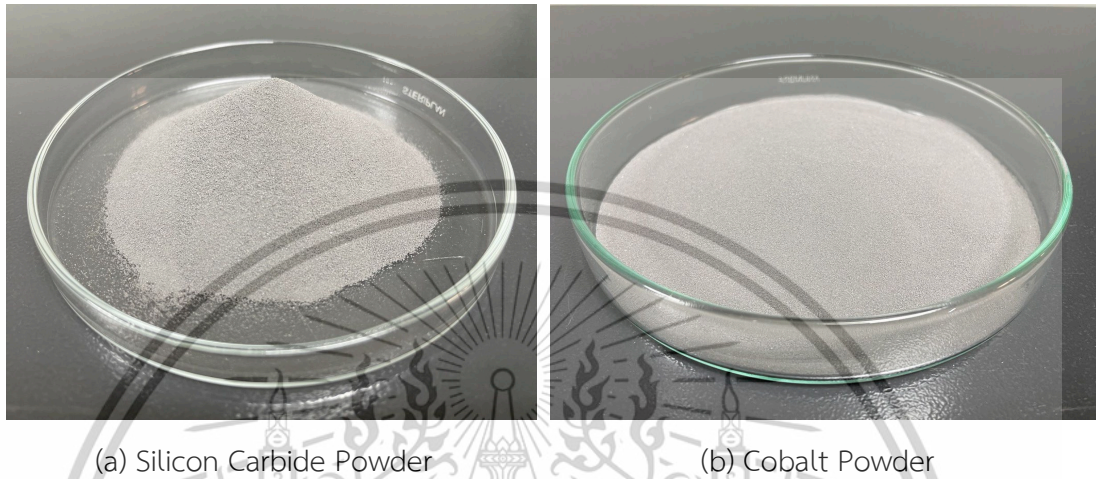


Figure 3.1 Alloying Elements

3.1.3 Experimental alloys

The final alloy for sintering is a mixture of the iron-based alloy ATOMET 4801 with a fixed 4.0 wt.% of SiC and 0.5 to 3.0 wt.% Co. The amount of iron-based material is adjusted according to Co content. A total of seven different compositions are prepared, six with different amounts of Co content and one without Co content. One without Co content is prepared as the reference material. **Table 3.2** shows the final composition of the studied alloys.



Figure 3.2 Analytical balance AND GF-400

This material is reserved for educational use only, not allowed for commercial use.

The weight of each alloy is measured carefully using a high-precision laboratory analytical balance model, AND GF-400. The analytical balance can indicate results to 4 decimal places in the gram unit and have a repeatability of 0.001g. **Figure 3.2** shows the AND GF-400 analytical balance.

Table 3.2 Nominal composition of experimental alloys

Sintered alloy	Nominal Composition (wt. %)						
	C	Co	Mo	Mn	Ni	Si	Fe
00Co	1.20	0.00	0.50	0.19	3.84	2.80	Balance
05Co	1.20	0.50	0.48	0.19	3.82	2.80	Balance
10Co	1.20	1.00	0.48	0.19	3.80	2.80	Balance
15Co	1.20	1.50	0.47	0.19	3.78	2.80	Balance
20Co	1.20	2.00	0.47	0.19	3.76	2.80	Balance
25Co	1.20	2.50	0.47	0.19	3.74	2.80	Balance
30Co	1.20	3.00	0.47	0.19	3.72	2.80	Balance

3.2 Sintered Specimen Preparation

Experimental sintered alloys were prepared via conventional or traditional powder metallurgy routes. Conventional powder metallurgy processes are widely used in industry due to their simplicity. It consisted of three main steps: mixing or blending, compacting, and sintering. **Figure 3.3** illustrates the conventional powder metallurgy process. Each step is described in the following sections.

3.2.1 Mixing step

All metal powders were mixed according to the nominal composition for experimental alloys. Then, 1.0 wt.% of Zinc stearate (ZnSt) was added as a lubricant for compaction purposes and poured into a plastic bottle. After that, mixed powders were blended using a mechanical rotating machine with a rotation speed of 20 rotations per minute.

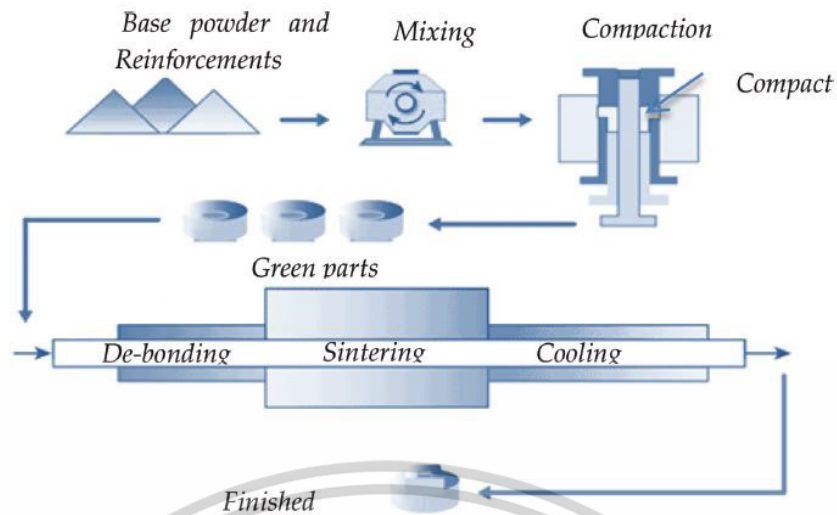


Figure 3.3 Conventional process of powder metallurgy [43]

During blending, the rotation speed is very important since it can affect the homogeneity of the mixed powder. If the rotation speed is too fast, the powders will not mix together homogeneously due to falling (opposite to flowing). Figure 3.4 shows bottles of mixed powder attached to a mechanically rotating machine for blending.



Figure 3.4 Mechanical rotating machine

3.2.2 Compacting step

After blending, mixed powders were poured into compaction dies and compacted into two different shapes, namely, a tensile test bar and a coin shape, with

This material is reserved for educational use only, not allowed for commercial use.

a green density of $6.5 \pm 0.05 \text{ g/cm}^3$. A hydraulic pressing machine was used for compaction, with a pressing pressure of around 120 bar. This machine was operated by manual control. Firstly, open the mold shape by pushing down the bottom die and filling the mixed powder into the mold, then press the top die to the desired pressure. After that, hold the top die for 30 seconds to 1 minute and release the top die. Finally, eject the bottom die to get the specimen. The hydraulic pressing machine and compacted specimens are shown in **Figure 3.5** and **Figure 3.6** respectively. The green specimens have enough strength for handling purpose.

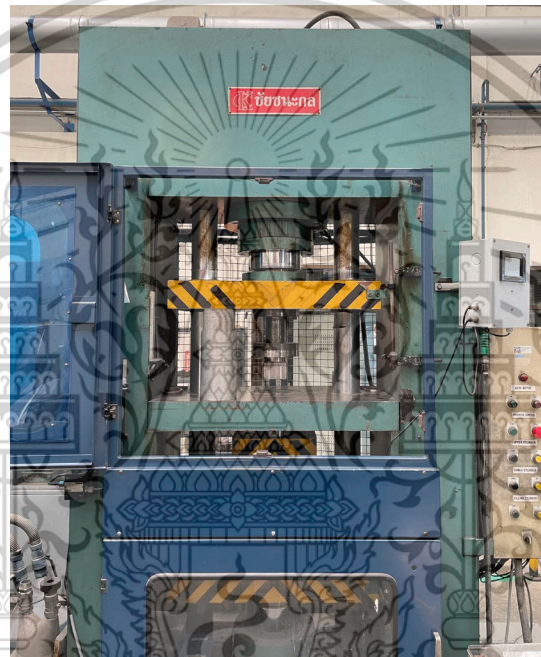


Figure 3.5 Hydraulic Pressing Machine

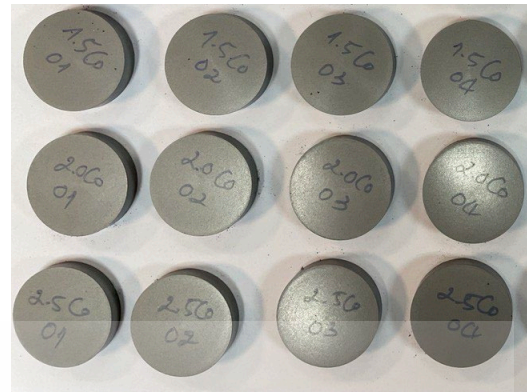
3.2.3 Sintering step

The final step in the traditional process of powder metallurgy is sintering. All compacted specimens were sintered in a high-vacuum sintering furnace (name) for 45 minutes and slowly cooled in the furnace. The sintering furnace uses hydrogen gas as fuel. The sintering furnace use hydrogen gas as fuel. **Figure 3.7** shows a high-vacuum sintering furnace machine (name). The sintering profile and inside view of the sintering furnace are shown in **Figure 3.8**. Sintering profile is divided into three main steps. The first step is to remove the lubricant from the compacted specimen by heating it up to 600 oC for 30 minutes. Then, the second step is to increase the heating temperature to 1250 oC (austenite temperature) to homogenize the austenite phase in specimens.

This material is reserved for educational use only, not allowed for commercial use.



(a) Tensile test bar



(b) Coin shape

Figure 3.6 Compacted specimens or green specimens

Lastly, the final step is cooling; specimens are slowly cooled in a sintering furnace. The surface roughness of the sintered specimen is not as smooth as the surface of the green specimen. **Figure 3.9** shows tensile test bars and coin shapes after sintering. As can be seen, the surfaces of sintered specimens are a little bit different from those of green specimens (before sintering).

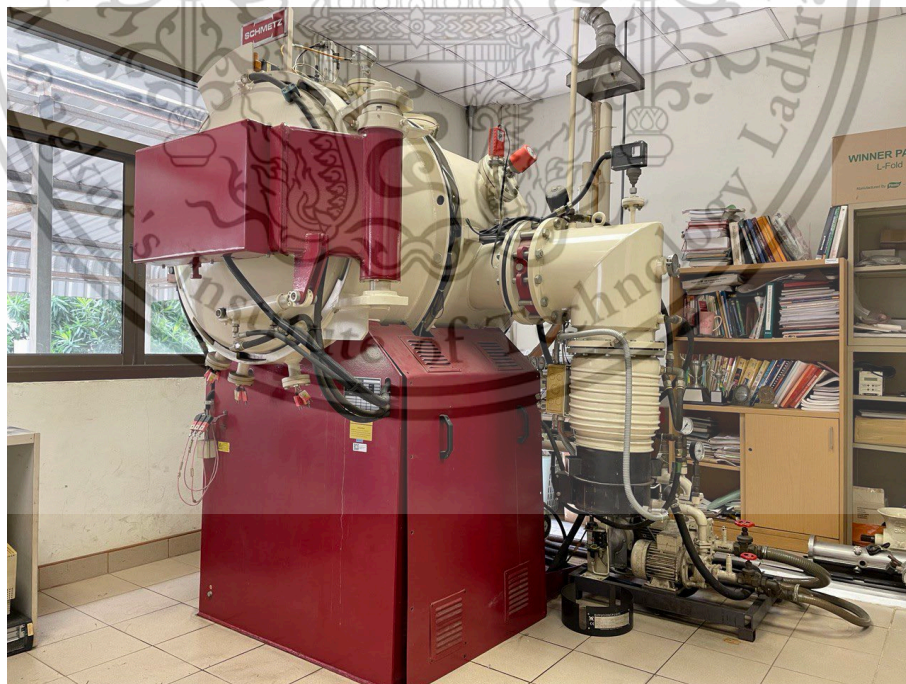


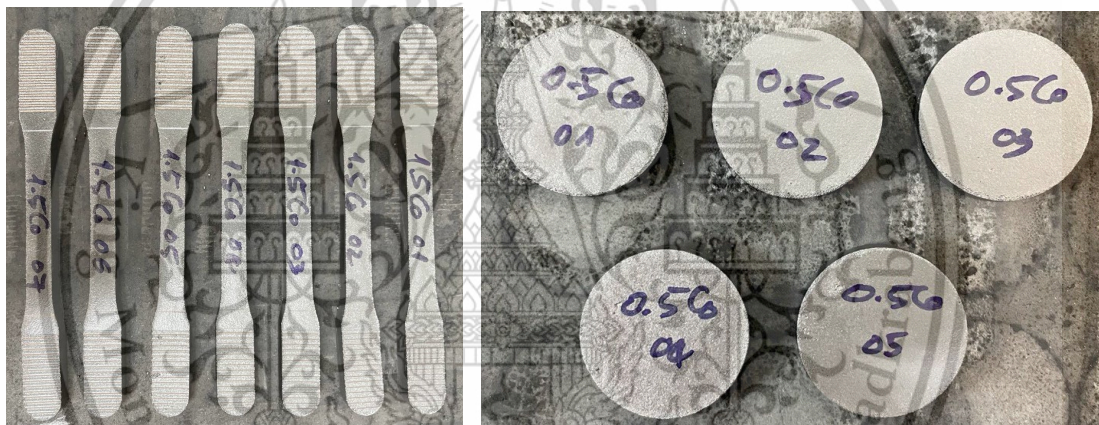
Figure 3.7 High vacuum sintering furnace (SCHMETZ)



(a) Sintering Profile

(b) Inside view of sintering furnace

Figure 3.8 Sintering profile and inside view of sintering furnace



(a) Tensile test specimens

(b) Coin shape specimen

Figure 3.9 Compacted specimens after sintering

3.3 Experimental Procedure

Figure 3.10 below shows the experimental procedure for these studied alloys. The microstructure and mechanical properties of sintered alloys are characterized and determined, respectively. The characterization methods consist of an optical microscope (OM), a scanning electron microscope (SEM), x-ray diffraction (XRD), and an electron probe microanalyzer (EPMA). Mechanical testing, including the Universal Tensile Test (UTS), Rockwell Hardness Test, and Wear Test, is conducted to determine the mechanical properties of the studied alloys. For mechanical tests, tensile test bar specimens after sintering can be used directly for tensile tests without further

preparation, while coin-shaped specimens need to undergo surface preparation for wear tests. Nevertheless, metallography specimens of sintered alloys are prepared for characterization purposes.

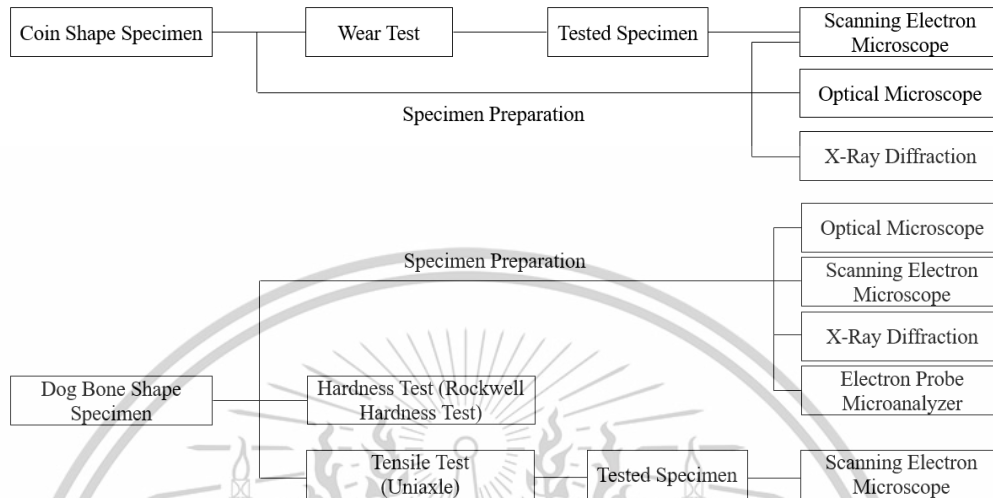


Figure 3.10 Flowchart of experimental procedure

3.4 Microstructure Characterization

The microstructure of the studied alloys is examined by OM and SEM, while its crystalline phases and the distribution of Co addition are analyzed by XRD and EPMA, respectively. Materials preparation and test methods for OM, SEM, and XRD will be discussed in the subsection below. Moreover, wear debris and the worn surface of dry sliding test specimens were also analyzed by SEM.

3.4.1 Optical microscope

Microstructure and morphology of sintered alloys are investigated using an optical microscope (OM), Olympus STM7. Olympus STM7 is a type of light microscope that provides high resolution and high contrast. Different magnifications from 50 to 1000 micrometers are observed. The surface of each sintered specimen was prepared according to metallography specimen preparation. Specimens were ground on silicon carbide papers from 120 grid to 1400 grid, then polished with diamond suspension from 6 to 1 micron. After that, the specimen was etched with 2% Nital. For color-tinted images, the specimen was prepared by same procedure and incorporated another etching step. The added etching step is to produce color contrast in the microstructure of the specimen. The Olympus STM7 machine is shown in **Figure 3.11**.

This material is reserved for educational use only, not allowed for commercial use.

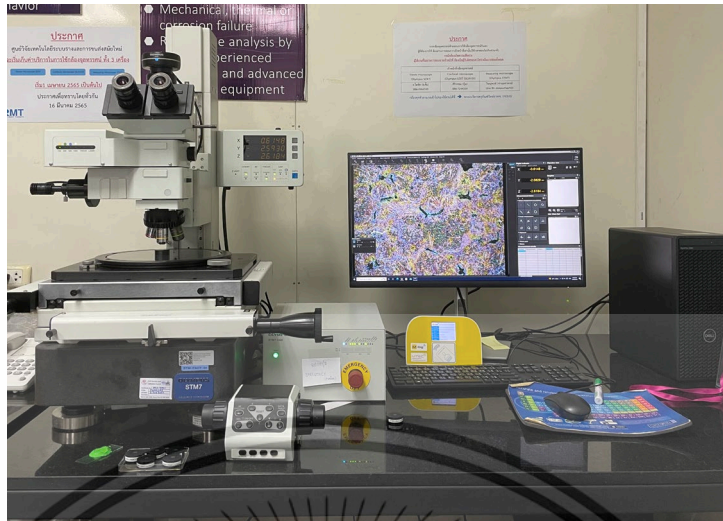


Figure 3.11 Optical microscope (Olympus STM7)

3.4.2 Scanning electron microscopy (SEM)

A scanning electron microscope (SEM) was used to further determine the microstructure of sintered alloys. More details, such as the depth and shape of phases of microstructure, can be observed by SEM. The surface of each sintered specimen was prepared by following the same procedure as an optical microscope. SEM was operated using the JSM-7800F Prime (Field Emission Scanning Electron Microscope) machine at 20 kV. The machine provides a high-contrast image with high magnification up to 3000x (1 micrometer). **Figure 3.12** shows the JSM-7800F Prime SEM machine.



Figure 3.12 Scanning electron microscope (JSM-7800F Prime)

3.4.3 X-ray diffraction (XRD)

X-ray diffraction was conducted to identify phases in the microstructure of sintered alloys. Rigaku TTRAX III X-ray diffractometer was used with a copper source (wavelength of 0.154 nm), a step size of 0.2°, an angle of 30-100°, and a time step of 0.5 s/step. The XRD sample is prepared by grinding with silicon carbide from 120 to 400 grids and etching with HNO₃ acid (40% volume into water) for 40 to 80 seconds and HCL acid (50% volume into water) for 5 to 10 seconds, respectively. A total of seven samples were analysed, and each sample took 30 to 40 minutes to complete. The X-ray diffractometer machine is shown in Figure 3.13.

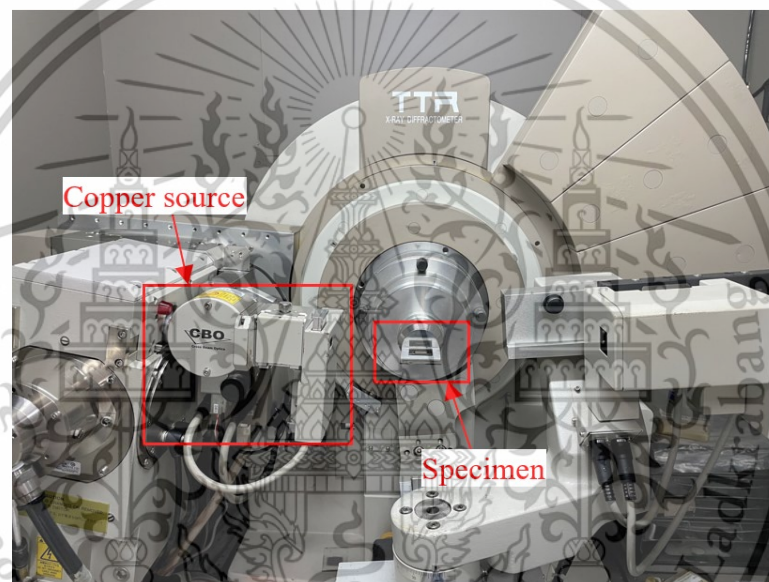


Figure 3.13 X-Ray diffractometer machine, Rigaku TTRAX III

After XRD analysis, quantitative phase analysis is performed using the reference intensity ratio (RIR) method. This method determined the weight percentage of retained austenite based on the peak intensity of each sintered alloy. The RIR method with Rietveld analysis and pattern-matching techniques was performed using JADE9 software. The percentages of retained austenite and ferrite were determined using this method. The ratio of the weight fractions of any two phases whose RIRs are known can be calculated using the following equation:

$$\frac{X_{\alpha}}{X_{\beta}} = \frac{I_{i\alpha}}{I_{j\beta}} \times \frac{I_{j\beta}^{rel}}{I_{i\alpha}^{rel}} \times \frac{RIR_{\beta,c}}{RIR_{\alpha,c}}$$

Where:

X_{α} & X_{β} : weight fraction of phase α and phase β

This material is reserved for educational use only, not allowed for commercial use.

$I_{i\alpha}$ & $I_{j\beta}$: intensity diffraction line i from α phase and line j from β phase

$I_{j\beta}^{rel}$ & $I_{i\alpha}^{rel}$: relative intensities of each phase

$RIR_{\beta,c}$ & $RIR_{\alpha,c}$: reference intensity ration of each phase (can obtain from PDF file)

Moreover, if all of the phases in a mixture have been identified, the following equation may be added.

$$\sum_{k=1}^n X_k = 1$$

Where n is the number of phases in mixture.

3.4.4 Electron probe microanalyzer (EPMA)

The electron probe microanalyzer (EPMA) is an instrument for determining the chemical composition of tiny amounts of solid materials. By using wavelength dispersive spectroscopy (WDS), an EPMA can perform accurate, quantitative elemental analyzes at extremely small "spot" dimensions (down to 1-2 microns), which is its main advantage. In this study, the Shimadzu EPMA 8050G was used to analyze the distribution of alloying elements in each phase of the microstructure. Two sintered alloys, namely the sintered 00Co alloy and the sintered 30Co alloy, were prepared by the same procedure as the SEM sample preparation and then analyzed with the EPMA. Figure 3.14 shows the Shimadzu-8050G electron probe microanalyzer.



Figure 3.14 Electron Probe Microanalyzer Shimadzu 8050G

3.5 Metallography Preparation

To observe the microstructure of sintered alloys, all specimens are prepared via the metallography preparation route. Metallography specimen preparation consists of five main operations: Sectioning, Mounting, Grinding, Polishing, and Etching. For OM and SEM, studied samples were prepared using the same method (metallography specimen), while XRD samples went through a bit different preparation. The preparation methods for OM, SEM, and XRD are described in the following sections.

3.5.1 Sectioning

Sectioning is the first operation in the preparation of a metallography specimen. It is the removal of a large area sample from a small area by a cutting process based on the interested areas of the studied alloys. One or two centimeters from each composition of sintered alloys were cut from the middle area of the tensile test bar. A cutting machine, as shown in **Figure 3.15**, is used for the cutting process.

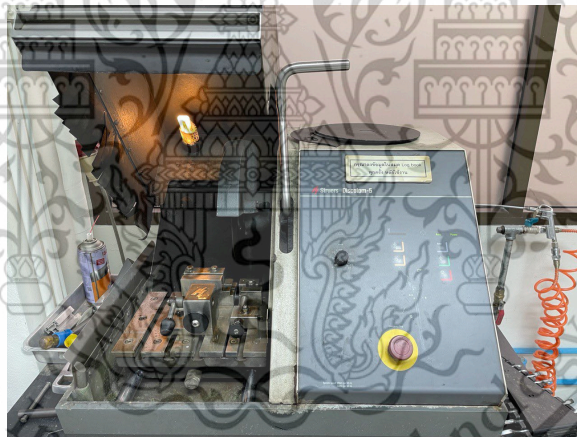


Figure 3.15 Cutting machine (StruersDiscotom-5)

3.5.2 Mounting

Mounting specimens is often necessary in preparation methods. All cut samples were mounted to facilitate handling for the next operation since the thickness of the cut sample is small; in this case, it is around 10 mm. Different types and methods of mounting are used for different purposes. In this preparation, hot or compression mounting was used with black carbide as mounting material. **Figure 3.16** shows the compression mounting machine and mounting material (phenolic black powder).



(a) Mounting machine, LaborPress-3

(b) Phenolic black powder

Figure 3.16 Compression mounting machine and mounting materials

3.5.3 Grinding

After mounting, all samples are ground against silicon carbide papers. Samples were ground to remove any damaged layers and rough surfaces. Silicon carbide paper with 120, 140, 240, 400, 800, 1200, and 1400 grids was used to obtain a smooth surface before the polishing stage. Low grid value means high friction, which results in high removal of the surface layer, while a high grid value offers low friction. A low friction between the sample surface and silicon carbide paper provides a smooth surface while removing scratches from the sample surface. Samples were pressed evenly on grinding paper with a rotation speed of 30 rpm and continuous water coolant to reduce the temperature at the sample surface, which can alter its microstructure. Upon switching from one grid paper to another grid paper, the surface of the sample should have visible scratches homogeneously with grinding rotation direction.

Moreover, samples were rotated about 90 degrees before grinding with the next grid paper to obtain a perpendicular direction to the last grid paper. This inspection during grinding is examined by the naked eye without magnification. Grinding machine and silicon carbide paper are shown in **Figure 3.17** and **Figure 3.18** respectively. All samples were cleaned and dried properly with ethanol and water to remove impurities before polishing.



Figure 3.17 Mechanical Rotating Machine for Grinding and Polishing



Figure 3.18 Silicon carbide papers

3.5.4 Polishing

After grinding, all samples were polished with diamond abrasive particles (diamond suspension). The objective of polishing is to produce a mirror-like surface by removing all scratching on the surface that is visible by naked eye inspection. Diamond abrasive particles with sizes of 6, 3, and 1 micron were used to remove all scratches on the last layer of the sample surface.



Figure 3.19 POLY-Diamond Suspension (Size 6, 3 and 1 micron)

The diamond abrasive particles are suspended in a liquid among the fibers of the polishing cloth. Three polishing clothes were used with each diamond suspension size. Different types of diamond suspension can be used depending on the material type. Figure 3.19 and Figure 3.20 illustrate diamond suspension and polishing clothes, respectively.

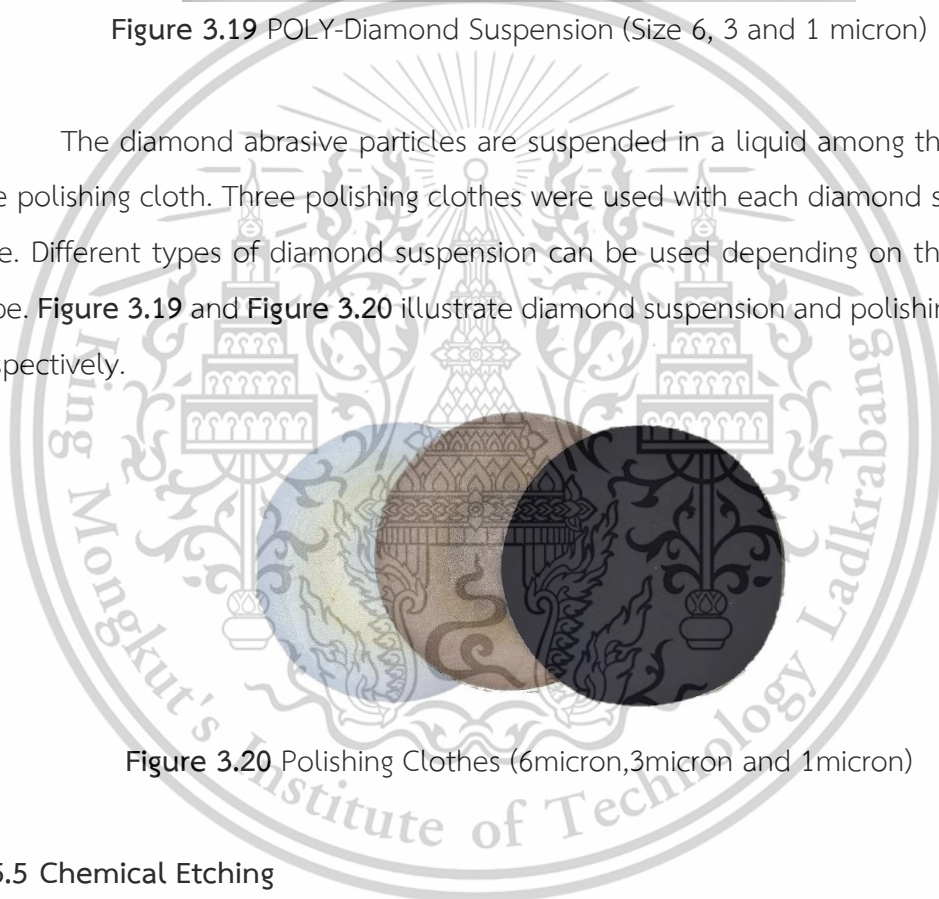


Figure 3.20 Polishing Clothes (6micron,3micron and 1micron)

3.5.5 Chemical Etching

The final step of metallography preparation is the etching step. It is used as a final step to reveal the microstructure of the specimen. Etching can be classified into different types, such as electrolytic etching, chemical etching, etc. In this experiment, chemical etching is used since it is the most commonly applied technique for metals and alloys. Different etchant solutions were used for OM, SEM, and XRD. For normal etching, 2% of Nital was used as an etchant for 5 to 15 seconds on all sintered alloys. Moreover, color etching was conducted for two-stage color tinting OM. For the two-

stage tinting procedure, the polished sample was pre-etched with 4% Picral for 60 s and then etched with 10 g of Na₂S₂O₅ in 100 ml distilled water.



(a) Nital 2% for normal etching

(b) Acid for two stage-tinting OM

Figure 3.21 Chemical etchant used for normal and color etching

3.6 Mechanical Properties Determination

A uniaxial tensile test was employed to determine mechanical properties. A tensile test was performed on sintered specimens using an Instron 8801 Universal Instrument by following the test standard ASTM E-8. **Figure 3.22** shows the Instron 8801 tensile testing machine during testing. Three tensile test bars of each sintered alloy were tested with a cross-head speed of 5 mm/min. Obtainable mechanical properties through this machine are ultimate tensile strength, stress at yield (0.2% strain), modulus (automatic Young's), and tensile strain at break (elongation %).

3.7 Hardness Test

A Hardness test was employed on all sintered specimens. A Rockwell hardness test was conducted using an indentation ball with a diameter of 1/16 inch and 100 kgf of total test force, as defined in ASTM E-18. HRB diamond pins were equipped with a macro hardness test machine, the Instron-930.

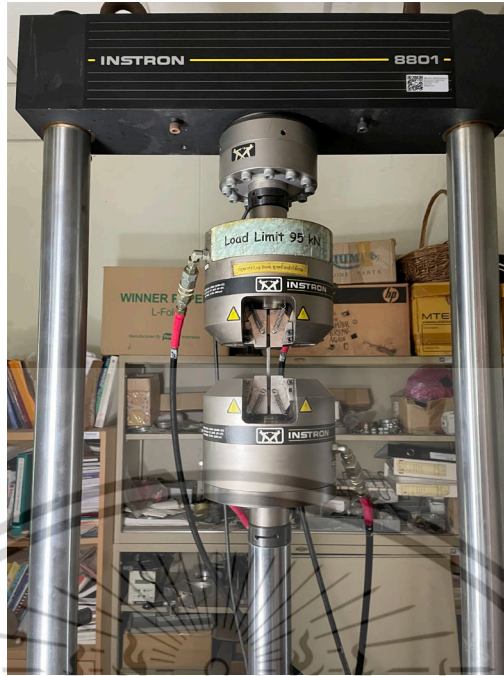


Figure 3.22 Tensile testing machine (Instron 8801)

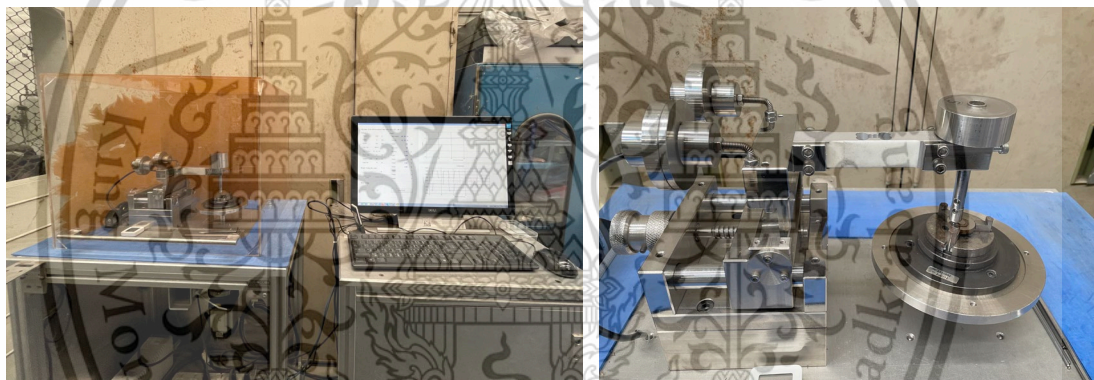
High precision macro hardness Instron-930 testing machine is shown in Figure 3.23. Six indentation points were tested on the different areas of the test bar. During testing, a diamond pin penetrated the surface for about 10–15 seconds, and then hardness values were obtained.



Figure 3.23 Hardness testing machine (Instron-930)

3.8 Determination of Tribology Properties and Wear Rate

All sixty-three coin-shaped specimens are prepared and tested with the pin-on-disc dry sliding test. The test procedure is carried out according to the wear test standard ASTM G99. The test condition includes a 1000-m sliding distance and a sliding speed of 0.1 m/s with relative humidity between 60 and 70%. A chromium SKF ball with a diameter of 6 mm is used as a counterpart material. The counterpart chromium SKF ball has roughness and hardness of $4\mu\text{m}$ and $838 \pm 21 \text{ HV}$ respectively. **Figure 3.24** illustrates the pin-on-disc dry sliding test setup. Tangential frictional force during sliding and surrounding temperatures are measured and recorded with an equipped data acquisition system. A chromium pinball with a 6 mm diameter was used as a counterpart material.



(a) Dry sliding test set up

(b) A close view on test set up

Figure 3.24 Wear test set up (pin-on-disc sliding test)

After tested, friction coefficient can be determine using the equation below:

$$\mu = \frac{F}{F_{\text{load}}} \quad (3.1)$$

Where:

F : tangential frictional force (N)

F_{Load} : normal load (N)

Moreover, the wear rate can be found using the formula given in ASTM G99. Since mass loss is too small to be measured, volume loss cannot be determined by the normal formula. By determining the volume loss using the following equation, the rate of wear of each specimen can be determined.

This material is reserved for educational use only, not allowed for commercial use.

$$\text{disk volume loss} = 2\pi R \left[r^2 \sin^{-1} \left(\frac{d}{2r} \right) - \left(\frac{d}{4} \right) (4r^2 - d^2)^{\frac{1}{2}} \right] \quad (3.2)$$

Where:

R : wear track radius (mm)

d : wear track width (mm)



CHAPTER 4

RESULTS AND DISCUSSION

4.1 Microstructure of Sintered Alloys

4.1.1 OM of sintered alloys without Co addition

An optical microscope image of the etched surface of the sintered alloy without Co addition is depicted in **Figure 4.1**. An OM image of sintered Fe-4.00Ni-0.50Mo-0.20Mn-Si-C with low magnification shows the overall microstructure feature consisting of black particles enveloped with ausferrite (bainitic ferrite and austenite plates) and martensite islands. Brownish regions represent martensite islands, while white regions represent ferrite. Bainitic ferrite is the light blue needle plate that coexists with ferrite. This microstructure has the same features as the microstructure of a sintered Fe-Ni-Si-C alloy containing 4.0 wt.% nickel [7].

The formation of this microstructure consisting of black particles enveloped by ferrite and striated structure (BF/M-A) is already illustrated and explained in [3]. A high martensite fraction is observed in the presence of bainitic ferrite and austenite plates. The high fraction of martensite might be the effect of nickel (Ni). It was previously found that Ni had a remarkable effect on phase transformation by shifting the CCT curve to the right. The addition of 4.0 wt.% Ni increases the proportions of BF/M-A structure while reducing ferrite and pearlite formation.

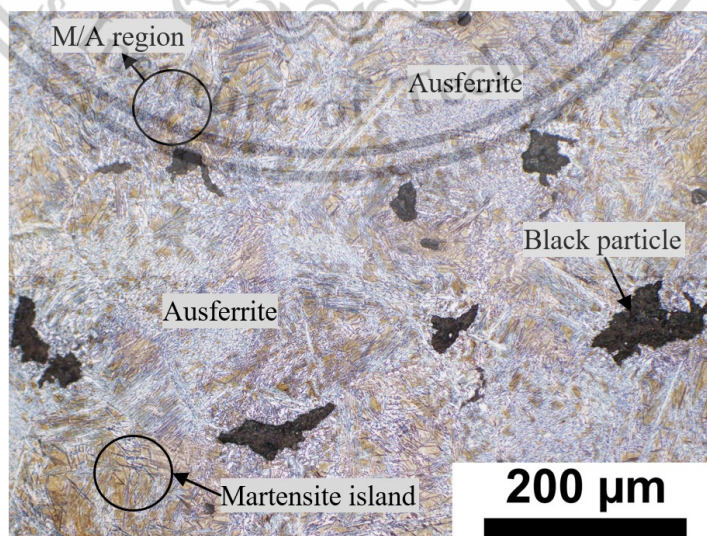


Figure 4.1 OM image of sintered Fe-4.00Ni-0.50Mo-0.20Mn-Si-C (low magnification)

This material is reserved for educational use only, not allowed for commercial use.

Further discussion on the effect of Ni is given alongside two-stage tinted OM images. Thus, the pre-alloyed Fe-4.00Ni-0.50Mo-0.20Mn-Si-C powder used for making the sintered 00Co composite also results in the same microstructure feature as the previous study. However, some features of microstructure are difficult to distinguish via a normal OM image. Two-stage color tinting images are illustrated in **Figure 4.2** to further clarify the presence of those features.

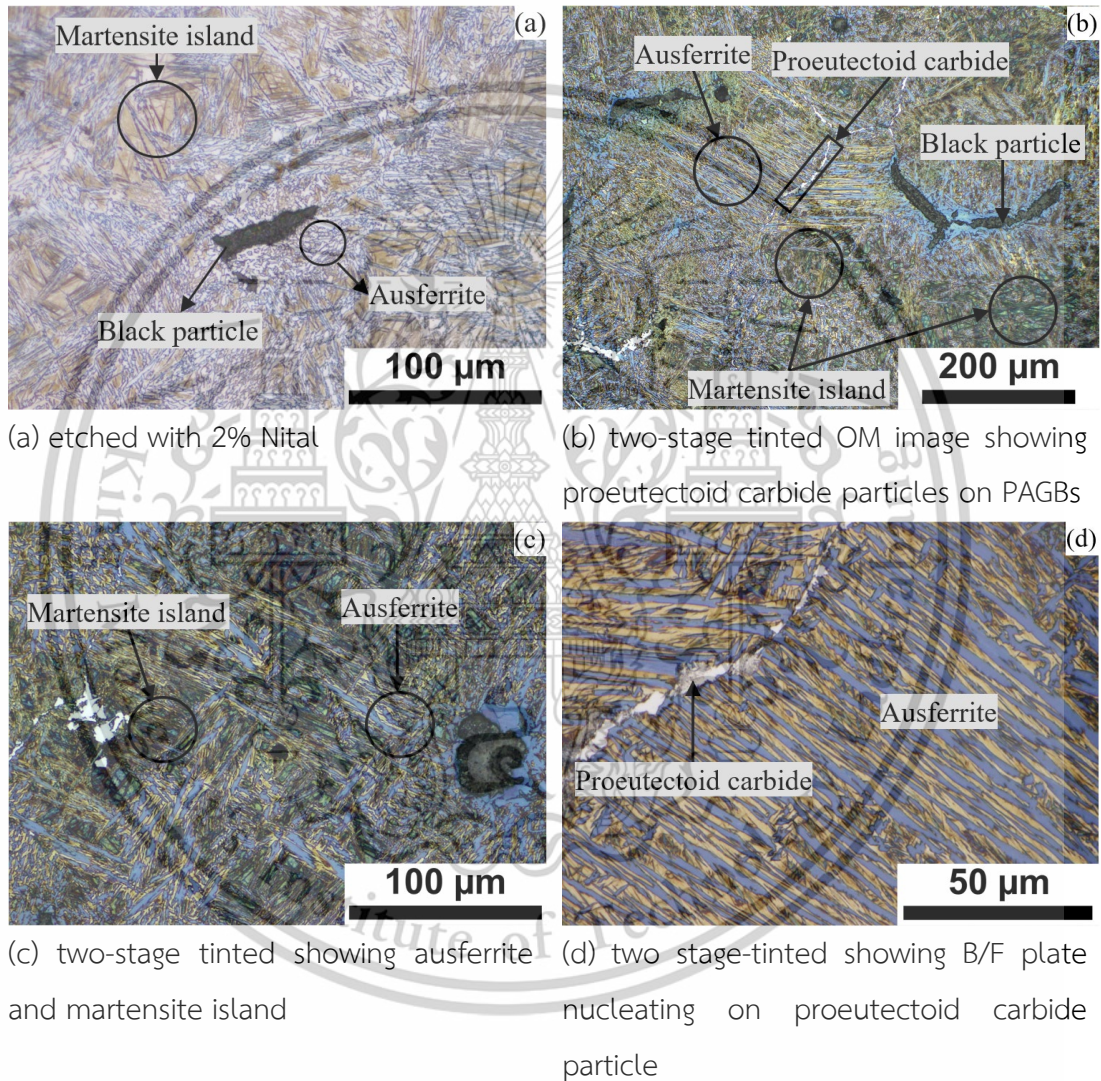


Figure 4.2 OM images of sintered 00Co composite, normal and two stage-tinted (color OM) low and high magnification

The two-stage tinted OM image provides a clearer picture of the feature within the microstructure. Two-stage tinted OM image with low magnification showed proeutectoid carbide networks along prior austenite grain boundaries (PAGBs) (**Figure**

4.2b). A two-stage tinting revealed that ferrite grains around a black particle and BF plates appeared in blue, austenite plates in light brown, and martensite islands in dark brown (Figure 4.2b and Figure 4.2c). In some areas, BF plates were observed to nucleate on thin ferrite films on proeutectoid carbide particles and grow into an austenite matrix (Figure 4.2d).

As shown in normal and two-stage tinted images, Figure 4.2a and Figure 4.2c, the microstructure of sintered 00Co composite shows nearly equal fractions of BF plates and martensite islands. Since the pre-alloyed Fe-4.00Ni-0.50Mo-0.20Mn powder is used for making the sintered 00Co composite, it is suspected that nickel (Ni) should be the principal alloying element, having a prime role in microstructural development.

It was reported that Ni promoted the formation of acicular ferrite while preventing the formation of granular bainite [44]. The presence of BF plates in sintered 00Co composites confirms the Ni role in acicular ferrite promotion. In addition to the function of acicular ferrite promotion, Ni also promotes martensite transformation. It was found previously that the fraction of ausferrite plus martensite increased with increasing Ni content in sintered Fe-Ni-Mo-Mn-Si-C composites [42].

The martensite fraction was even dominant in sintered Fe-Ni-Mo-Mn-Si-C composite produced from pre-alloyed Fe-4.00Ni-0.50Mo-0.20Mn powder. This suggests that one function of alloying Ni element in sintered Fe-Ni-Mo-Mn-Si-C composites is to promote martensite transformation. The coexistence of ausferrite (blue BF plates and light brown austenite plates) and martensite islands (dark brown islands) in sintered 00Co composite matrix (Figure 4.2c) indicates that the austenite matrix surrounding black particles transforms to ausferrite and martensite at low temperatures.

Typical eutectoid transformations (austenite to divorced eutectoid transformation (DET) products [45], austenite to lamellar pearlite (LP) [46], and austenite to degenerated pearlite (DP) [47] are missing from the final microstructure of sintered 00Co composite. Since this sintered composite contains multi-alloying elements, their effects on the formations of ausferrite and martensite under the slow cooling with the rate of 0.1 °C/s is worth discussing in more details.

4.1.2 OM of sintered alloys with Co addition

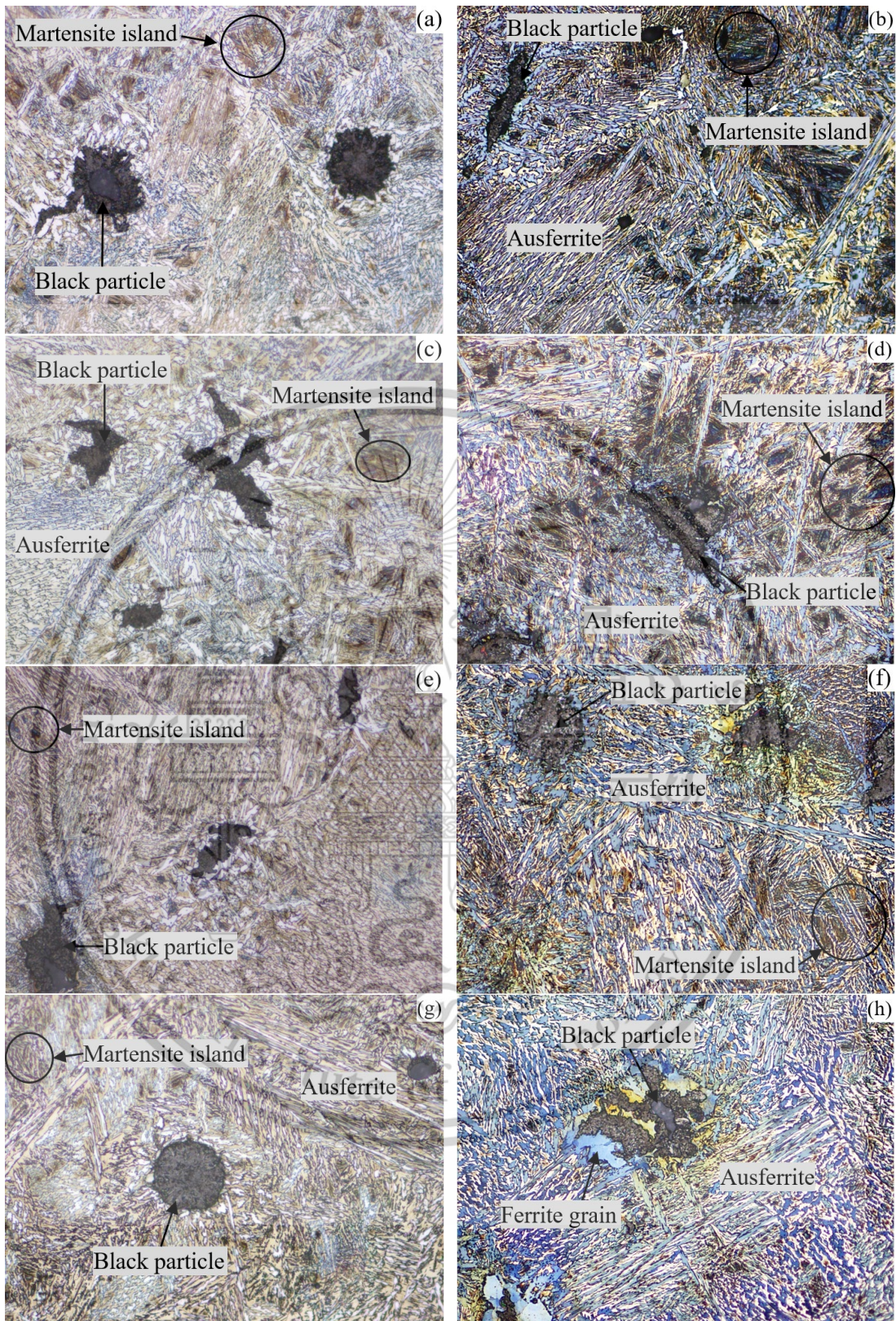
The sintered composites with Co additions showed different microstructural

changes (Figure 4.3). The first change was the decrease of proeutectoid carbide amounts in sintered 05Co, 10Co, and 15Co composites (images are not shown here). The second change was the decrease of martensite block fraction with increasing Mo content in sintered 05Co (Figure 4.3a and 4.3b), 10Co (Figure 4.3c and 4.3d), and 15Co (Figure 4.3e and 4.3f) composites. The martensite islands were hardly observed in sintered 20Co (Figure 4.3g and 4.3h), 25Co (Figure 4.3i and 4.3j), and 30Co (Figure 4.3k and 4.3l) composites. The third was the reappearance of PF grains around black particles in sintered 20Co (Figure 4.3g and 4.3h), 25Co (Figure 4.3i and 4.3j), and 30Co (Figure 4.3k and 4.3l) composites.

The most important change was the increase of blue BF plates and the associated increase of ausferrite (Figure 4.3b, 4.3d, 4.3f, 4.3h, 4.3j and 4.3l). The increase of BF fraction with increasing Co content confirms that Co addition promotes BF transformation. The sintered composites with austempered ductile iron-like microstructure (graphite nodules plus ausferrite without or with a small martensite fraction) can be produced by adding Co contents of ≥ 2.0 wt%.

With BF transformation acceleration, the competitive martensite transformation is reduced. The BF transformation acceleration was explained using thermodynamics. It was mentioned that the difference in free energy between austenite (γ) and ferrite (α) given as $\Delta G^{\gamma\alpha} = G^\alpha - G^\gamma$, is the driving force for transformation [7]. Both the nucleation and the growth rates can be expected to increase as a function of $|\Delta G^{\gamma\alpha}|$. The addition of Co and Al boosts $|\Delta G^{\gamma\alpha}|$, causing the rate of transformation to increase. Similarly, the acceleration of BF transformation is attributed to the increase in the free energy change during the transformation of austenite, caused by the alloying additions [8]–[10].

As given in the reference [48], Co leads to a decrease of the value of the maximum energy for nucleation (ΔG_m) in accordance with a mechanism of nucleation by dissociation of dislocations and an increase in austenite carbon content (x_γ), i.e., a displacement of the T'_0 curve to higher carbon content.



This material is reserved for educational use only, not allowed for commercial use.

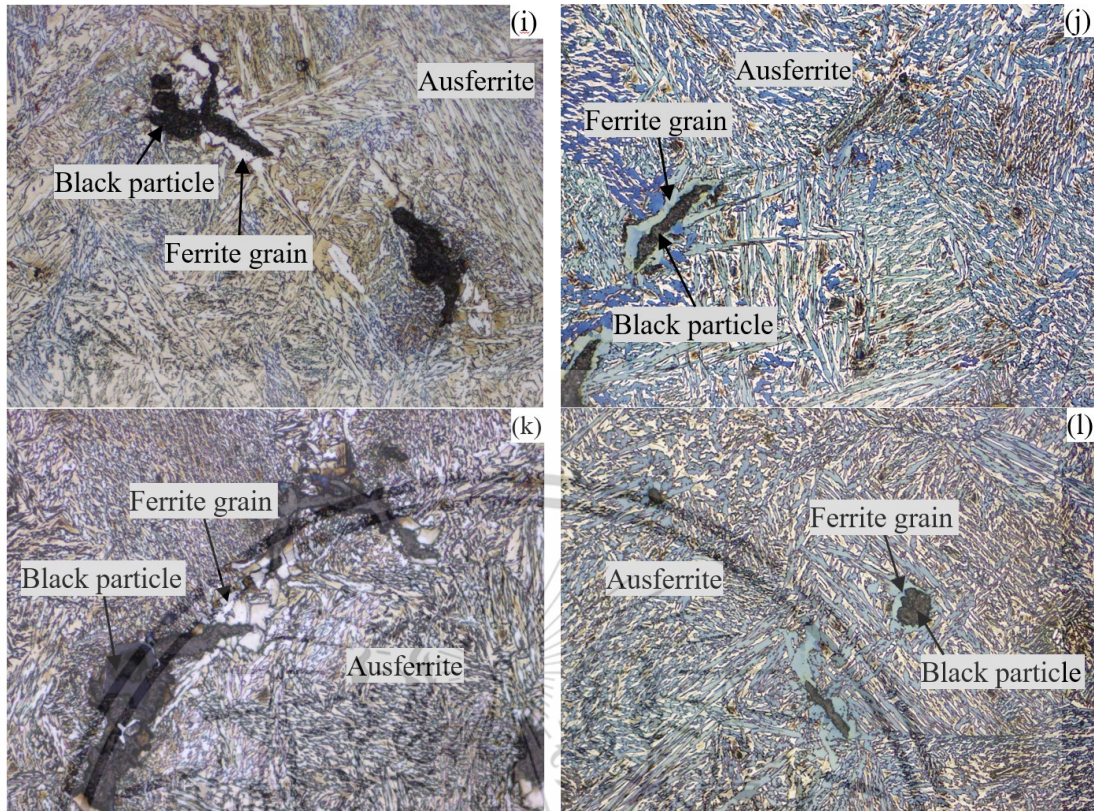


Figure 4.3 OM and tinted OM images of sintered composites: (a and b) sintered 05Co composite, (c and d) sintered 10Co composite, (e and f) sintered 15Co composite, (g and h) sintered 20Co composite, (i and j) sintered 25Co composite, and (k and l) sintered 30Co composite.

Consequently, cobalt leads to an acceleration of the bainitic transformation and to a higher value of the maximum volume fraction of BF formed at the end of the transformation. Due to effective BF transformation acceleration, the Co addition is applied to produce super bainitic steels with extremely high strengths [49]–[52].

4.1.3 X-ray diffraction of sintered alloys

XRD patterns of all experimental sintered alloys showed peaks of face-centered cubic (fcc) crystal structure of γ -austenite and body-centered cubic (bcc) crystal structure of α -ferrite. **Figure 4.4** displays XRD patterns of sintered 00Co (a), 05Co (b), 10Co (c), 15Co (d), 20Co (e), 25Co (f) and 30Co (g) alloys. The XRD pattern of the sintered 00Co composite showed strong peaks of face-centered cubic (fcc) crystal structure of γ -austenite and of body-centered cubic (bcc) crystal structure of α -ferrite (**Figure 4.4a**). All XRD patterns of sintered 05Co (**Figure 4.4b**), 10Co (**Figure 4.4c**), 15Co

(Figure 4.4d), 20 Co (Figure 4.4e), 25Co (Figure 4.4f), and 30Co (Figure 4.4g) composites showed strong peaks of austenite and ferrite. It should be noted here that martensite blocks coexist with BF and RA plates in sintered alloys with added Co contents of up to 1.5 wt.%.

Due to high C content (Table 3.2), martensite in these sintered alloys is highly likely to be plate martensite. In general, the XRD peaks of plate martensite having body-centered tetragonal (bct) crystal structure show peak splits because the lattice parameter a is not equal to the lattice parameter c in the bct crystal structure. However, the XRD peaks of bct crystal structure of plate martensite are not observed in Figure 4.4. No peak split indicates that the bct peaks of plate martensite are masked by bcc peaks of BF plates.

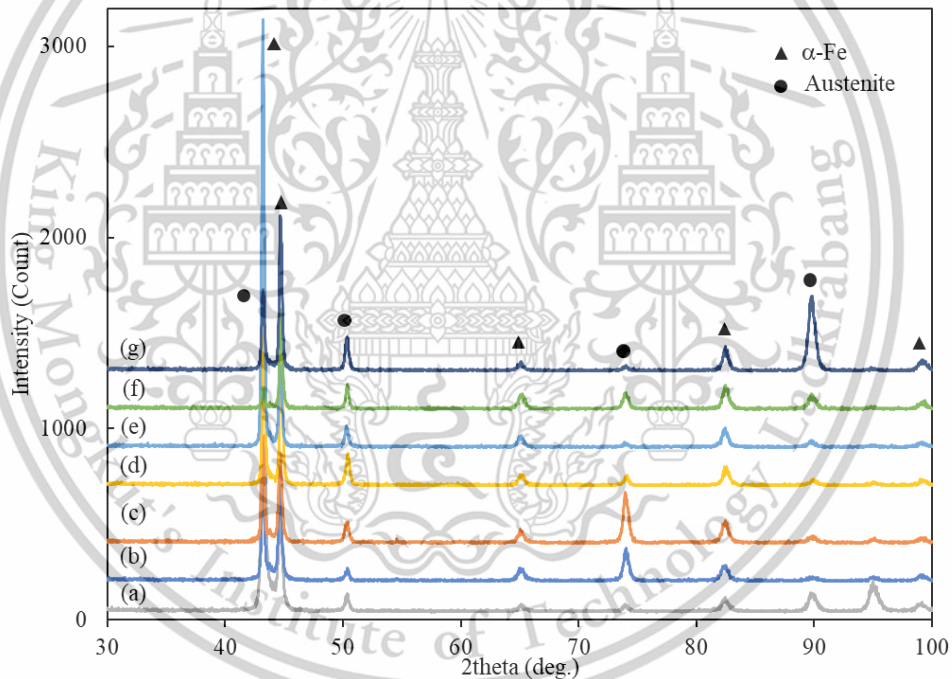


Figure 4.4 XRD pattern of experimental sintered alloys (a) sintered 00Co, (b) sintered 05Co, (c) sintered 10Co, (d) sintered 15Co, (e) sintered 20Co, (f) sintered 25Co and (g) sintered 30Co alloys

The weight fraction of retained austenite and ferrites phases of each sintered alloy was determined using JADE 9 software analysis. Each phase fraction of each sintered alloy is shown in Table 4.1. The XRD analysis reports generated from JADE9 software can be found in the APPENDIX.

This material is reserved for educational use only, not allowed for commercial use.

Table 4.1 Weight fraction of austenite and ferrite in experimental sintered alloys.

Sintered alloys	Weight Fraction (wt.%)	
	Retained Austenite	Ferrite
00Co	50.1	49.9
05Co	39.8	60.2
10Co	49.9	50.1
15Co	47.6	52.4
20Co	54.4	45.6
25Co	27.6	72.4
30Co	42.7	57.3

4.1.4 SEM images of sintered alloys without Co addition

Figure 4.5 shows a SEM micrograph of sintered alloys without Co addition. The common microstructural features of sintered 00Co alloy consist of black particles enveloped with ferrite grains, ausferrite structure, and martensite blocks. These features were also found in an SEM image containing 4.0 wt.% Ni in previous research [7]. Many martensite blocks were observed, along with B/F and austenite. The M block in **Figure 4.5** represents the martensite region, while the B/F+A block represents bainitic ferrite plus austenite region. It was noted that bainitic ferrite formed as a sheaf-like plate and coexisted with austenite.

The observed martensite blocks further confirm the presence of a high fraction of martensite found in the OM micrograph of sintered 00Co alloy. Some martensite formation formed within the austenite grain, which is difficult to differentiate. So, some blocks in this SEM image are classified as M-A (Martensite-Austenite). M-A blocks are also considered martensite-colonized blocks. These low-temperature transformation products, especially M-A, clearly show the effect of Ni in pre-alloy powder. Due to slow kinetic transformation at low temperatures, a low fraction of B/F is formed. Thus,

martensite formation occupied many regions in the microstructure, resulting in a high fraction of M/A.

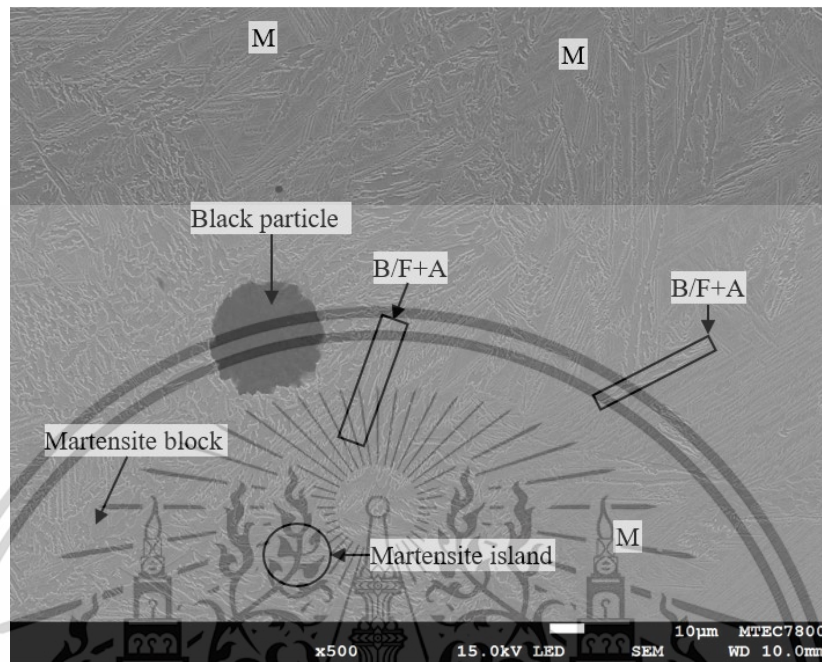
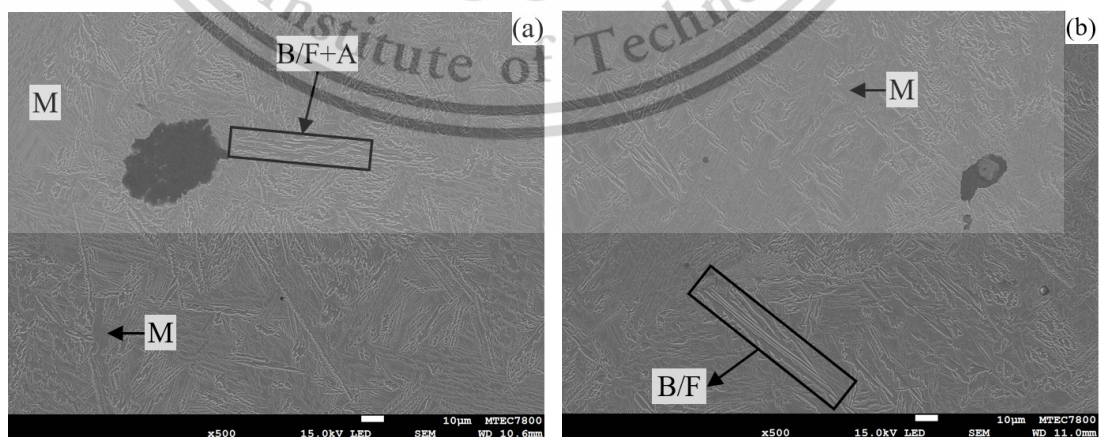


Figure 4.5 SEM image of sintered 00Co alloy

4.1.5 SEM images of sintered alloys with Co addition

SEM images of all sintered alloys with Co addition (sintered 05Co, sintered 10Co, sintered 15Co, sintered 20Co, sintered 25Co, and sintered 30Co alloy) are depicted in Figure 4.6. Figure 4.6 shows common feature as Figure 4.5, however, there is significant change as Co content exceed 1.5 wt.%.



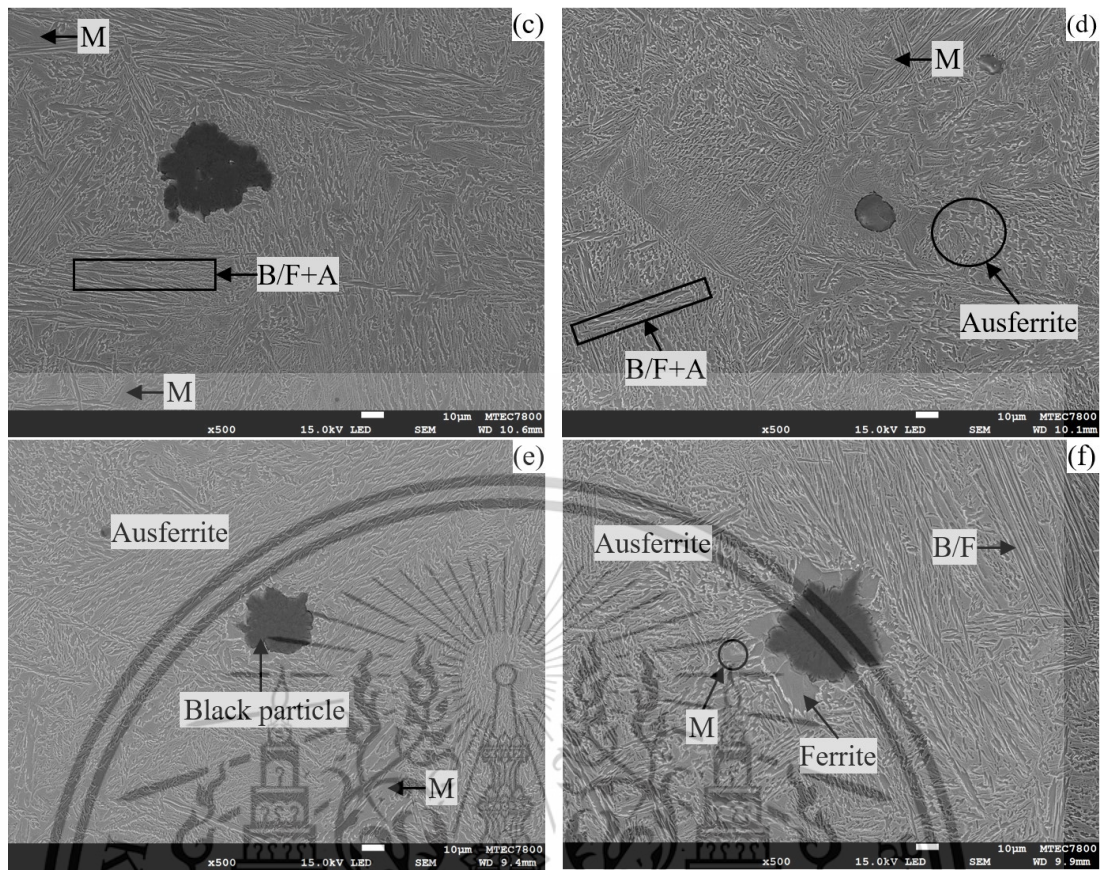


Figure 4.6 SEM image of sintered alloys; (a) sintered 05Co, (b) sintered 10Co, (c) sintered 15Co, (d) sintered 20Co, (e) sintered 25Co and (f) sintered 30 alloys

The matrices of experimental sintered alloys showed etched plates and unetched plates and blocks. The etched plates represented BF plates, while the unetched plates and blocks represented RA plates and martensite blocks, respectively. According to the SEM images given in Figure 4.6, it was found that the BF fraction increased with increasing added Co content. This result also confirms that Co addition promotes bainitic transformation.

To further observe the effect of Co addition, high magnifications of sintered 05 and sintered 30 Co composites are shown in Figure 4.7. High magnification dictates more details on the shape and morphology of the ausferrite features in both sintered composites. Furthermore, the SEM images of sintered 05Co and 30Co give more details on the effect of Co addition on mechanical properties, which are discussed in the next section.

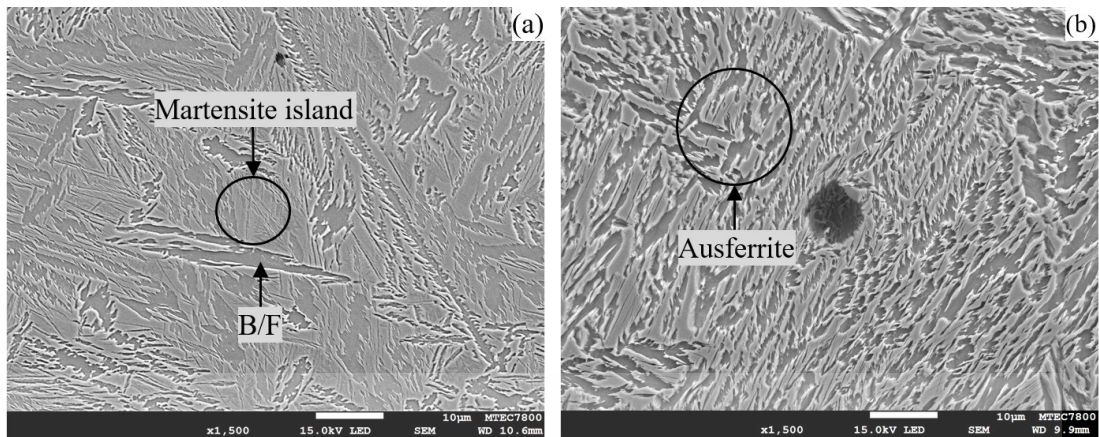
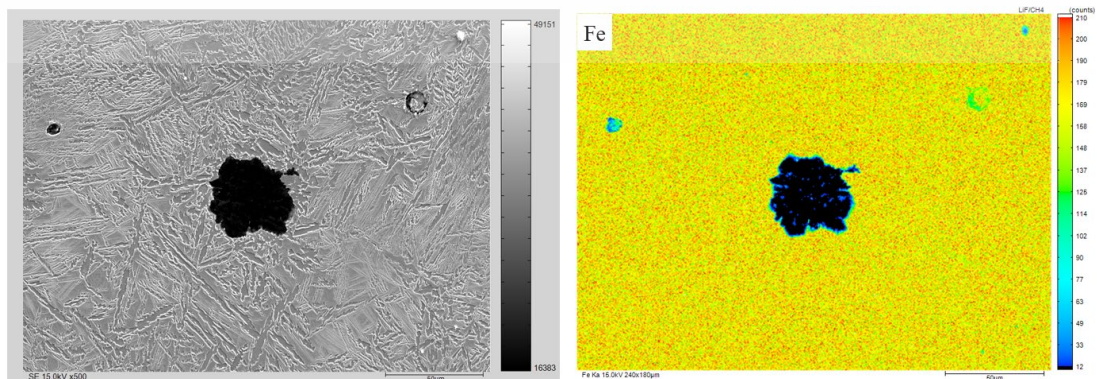


Figure 4.7 Comparison of matrix of sintered composite; (a) sintered 05Co and (b) sintered 30Co

4.1.6 EPMA mapping analysis of sintered 00Co and 30Co alloys

The distribution of chemical content in the microstructure was examined using an electron probe microanalyzer (EPMA). To show how the alloying elements were distributed inside the sintered alloy matrix, EPMA was carried out. Two areas of sintered 00Co alloy had been analyzed. Figure 4.8 illustrates the mapping analysis of sintered 00Co alloy. The EPMA mapping of martensite and ausferrite mixtures around black particles is shown in Figure 4.8. The elemental maps reveal that the black particle contains a high count of carbon, while ausferrite and martensite contain less. The distribution of the alloying is consistent within each microstructure phase.

Besides the Fe element, other alloying elements such as Ni, Mn, and Si are uniformly distributed within the microstructure except Mo. It can be observed that Mo is distributed more in the martensite region. Hence, it can be stated that Mo has a strong influence on the martensite phase. Another analysis area of sintered 00Co alloy can be found in the Appendix.



This material is reserved for educational use only, not allowed for commercial use.

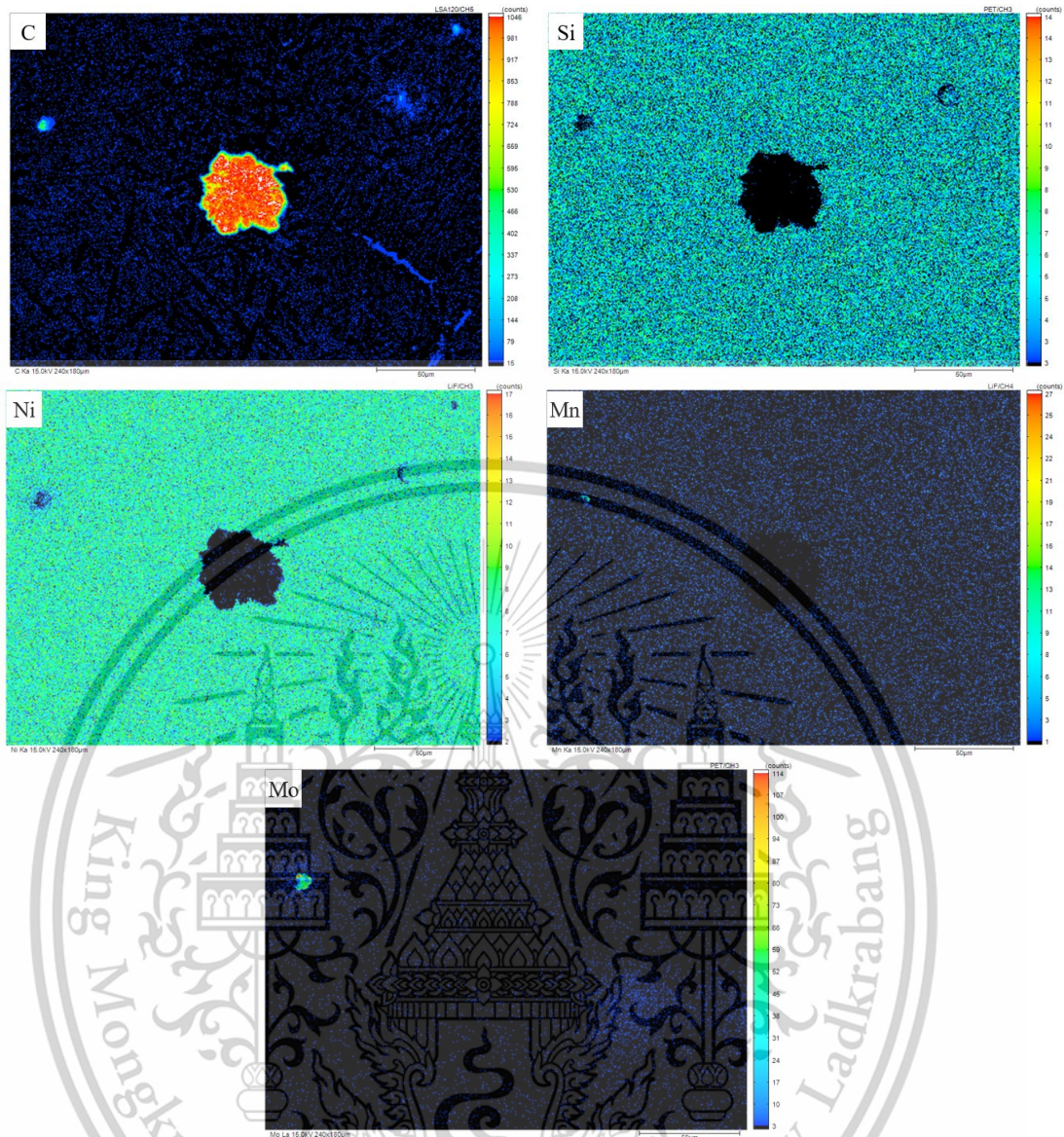


Figure 4.8 EPMA mapping of sintered 00Co alloy

Nevertheless, two areas of sintered 30Co alloy were also subjected to EPMA mapping analysis. Figure 4.9 depicts EPMA mapping of sintered 30Co alloy. The analyzed area consists of black particles surrounded by polygonal ferrite and a mixture of ausferrite and retained austenite. From mapping analysis, carbon is more distributed in black particles and carbon enrich retained austenite region, while no carbon intensity appears in the polygonal ferrite area around black particles. Unlike Mo element in sintered 00Co alloy, Mo is uniformly distributed on all areas, including black particles, in sintered alloy with 3.0 wt.% of Co addition.

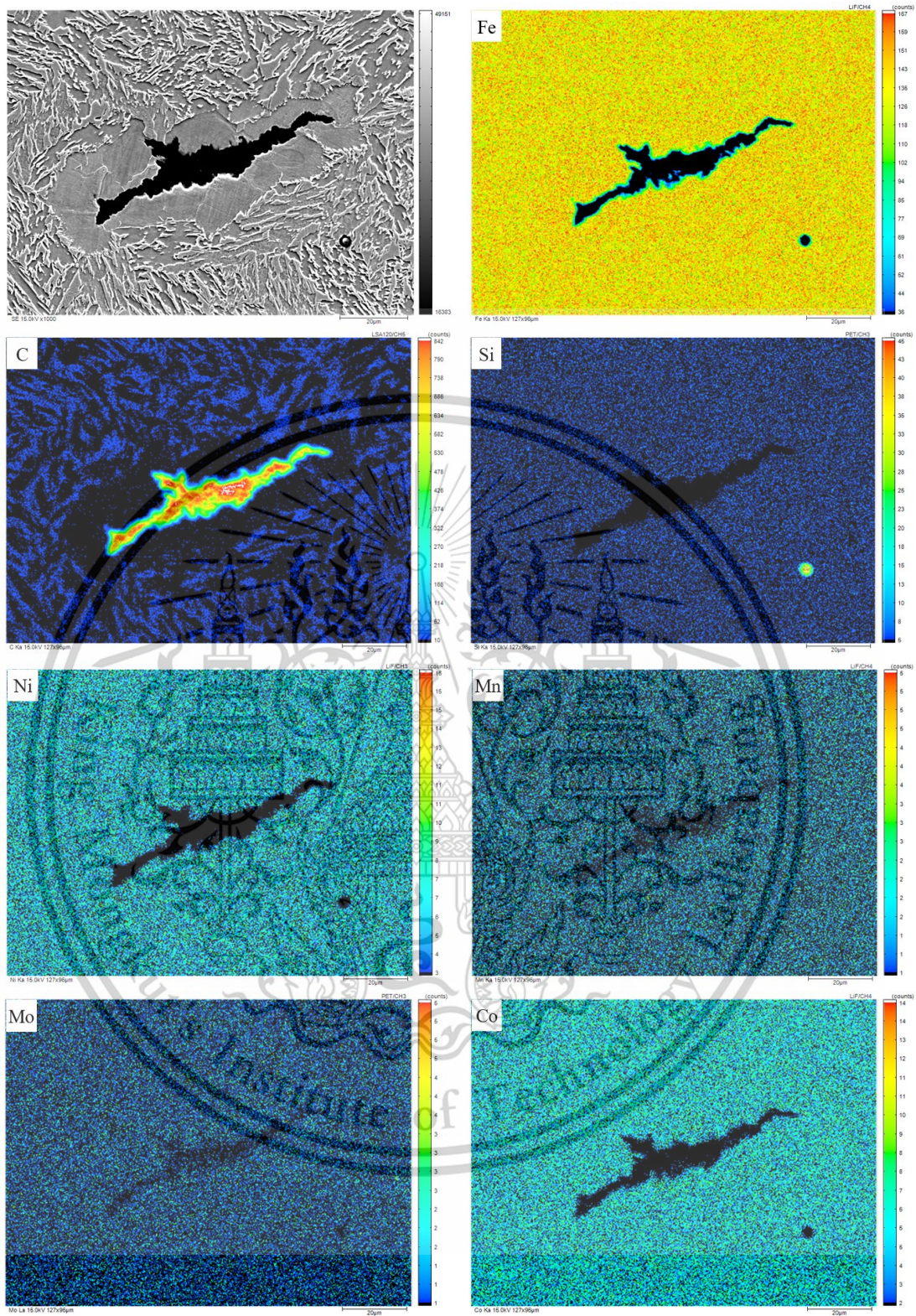


Figure 4.9 EPMA mapping of sintered 30Co alloy

Figure 4.9 shows that Co is uniformly distributed in the ausferrite and polygonal ferrite areas. From this mapping analysis, we can further confirm the formation of

This material is reserved for educational use only, not allowed for commercial use.

retained austenite within the ausferrite matrix. The retained austenite is enriched with carbon.

4.2 Mechanical Properties of Sintered Alloys

4.2.1 Hardness of sintered alloys

The hardness value of sintered alloys with and without Co addition is illustrated in **Figure 4.10**. The average Rockwell scale B values of sintered 00Co, 05Co, 10Co, 15Co, 20Co, 25Co and 30Co composites are 98.83, 95.73, 99.85, 101.48, 101.50, 101.53, and 102.38 HRB, respectively. The lowest hardness value is observed on sintered 00Co composite, while sintered 30Co has the highest hardness value. There is a slight increase in hardness value between 0.5 wt.% Co and 1.05 wt.% Co. However, there is no significant change as the Co increases.

It can be stated that hardness is insensitive to the added Co content. A hardness value of approximately 100HRB was also reported in previous studies on sintered alloys. Moreover, the formation of B/F and M-A was responsible for hardness, as stated in the study of the effect of Molybdenum [42]. From the literature review, the martensite phase is known to be responsible for hardness since fully martensitic steels exhibit a very high hardness value compared to bainitic steels (which contain bainitic ferrite). In this study, the martensite fraction decreased as Co increased and was replaced by the formation of ausferrite (B/F + austenite) but the hardness value did not decrease as martensite decreased. This might be the results of the phase mixture of B/F and M-A in sintered steels. Nevertheless, this phenomenon is not widely investigated in sintered steels produced via conventional PM.

4.2.2 Tensile properties of sintered alloys

Figure 4.11 illustrates the tensile and yield strengths, while **Table 4.2** shows the tensile properties of experimental sintered alloys. The tensile strength gradually increased with increasing Co content. Interestingly, the elongation value increased appreciably with added Co content. All experimental sintered alloys showed ultimate tensile strengths higher than 800 MPa. It was found that the values of elongation at break increased with increasing Co content. The elongation values of ≥ 5.0 % were observed in sintered composites with Co contents of ≥ 1.5 wt. %.

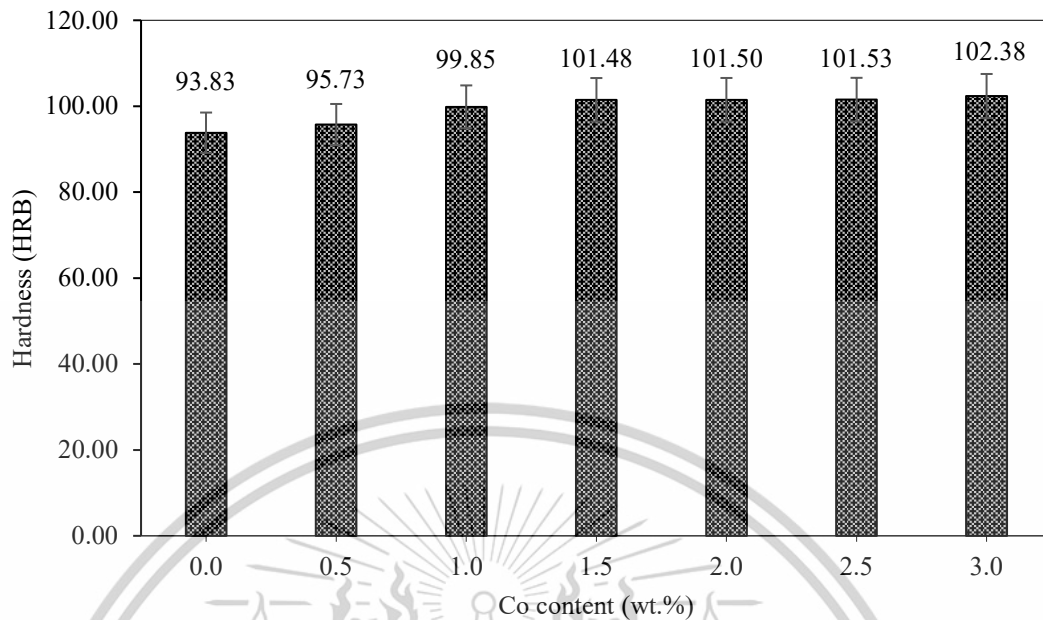


Figure 4.10 Hardness values of experimental sintered composites

By taking the microstructural features given above into account, it is found that the experimental results indicate that the replacement of martensite blocks by fine ausferrite structures leads to a gradual increase in tensile strength and elongation value. The increase in tensile strength is due to the very thin thickness of BF component of ausferrite structure. It was suggested that the strength of bainitic steels arises from the BF plate thickness rather than the length[8], [51], [53], [54].

The increase in elongation value is attributed to the TRIP effect [55]. The Co addition does not only lead to BF promotion but also refines the ausferrite structure. This means that the austenite component of the ausferrite structure is also refined. The TRIP effect depends on RA factors such as volume fraction, shape, size, and environment. The important RA property related to the TRIP effect is mechanical stability. In a past study, it was mentioned in the past study that too-stable austenite was no guarantee for better results [28]. The increase in elongation values indicates that thin RA plates in experimentally sintered Co-added alloys (this work) have stability suitable for the TRIP effect. The experimental results given above also suggest that there is no strength-ductility trade-off in the sintered Co-added alloys produced in this work.

The TRIP effect which enhances the ductility during transformation depend on the thickness, thermal and mechanical stability of the retained austenite plate. However, according to weight fraction from XRD analysis (can be found in Appendix C) shows that the amount of ferrite which include bainitic ferrite and free ferrite grain around black particle is greater than the amount of retained austenite. According to OM image at low magnification, more ferrite grain around black particle were observed in sintered alloy with high Co addition. So, it is speculated that free ferrite grain around black particles had more influence on the ductility of the sintered alloys (≥ 2.0 wt.% Co) which comprise of high fraction of ausferrite in their microstructure.

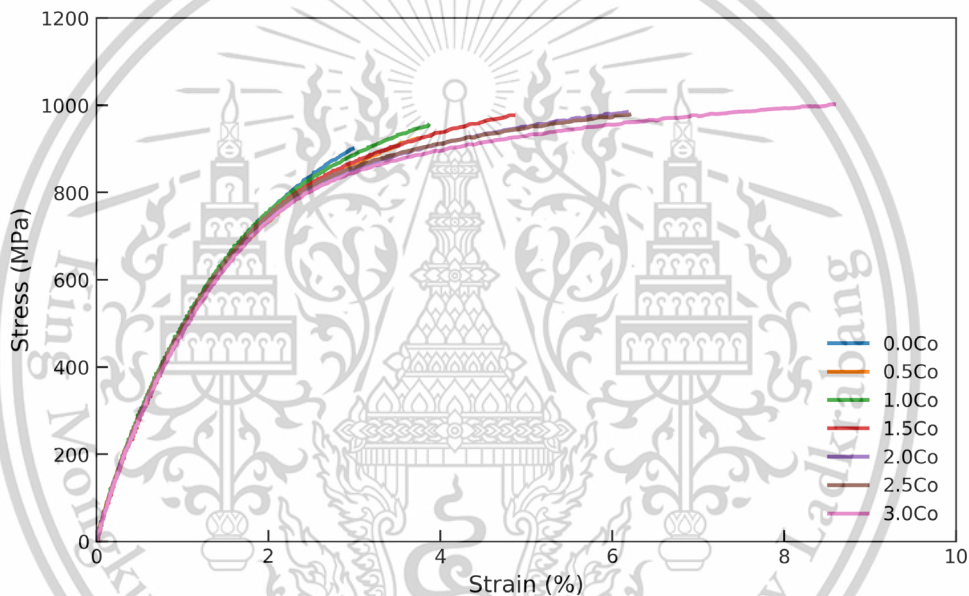


Figure 4.11 Ultimate and yield strength of all sintered alloys

To clarify the influence of microstructure on tensile strength and ductility, the microstructures of sintered 05Co and 30Co composites are compared (Figure 4.7). The sintered 05Co composite microstructure comprises bainitic ferrite plates and large martensite-austenite (MA) islands (Figure 4.7a) whereas sintered 30Co composite microstructure comprises bainitic ferrite and slim MA plates (Figure 4.7b). This may indicate that the microstructure comprising bainitic ferrite and slim MA plates is favored for enhanced ductility.

Table 4.2 Average value of tensile properties of experimental sintered alloys

Co content (wt.%)	UTS (MPa)	YS (MPa)	Elongation (%)
0.0Co	908.34	467.50	2.92
0.5Co	947.42	478.89	3.74
1.0Co	958.88	484.52	4.01
1.5Co	980.66	499.92	5.10
2.0Co	992.23	493.05	6.12
2.5Co	967.77	470.76	6.17
3.0Co	1066.65	494.67	8.64

The strength-ductility trade-off is avoided in sintered Co-added composites, as seen by the rise in elongation value as tensile strength rises. A number of factors, including the dual-phase lamellar microstructure [56], core-shell microstructure [57], nano twinning [58], dual heterogeneous structure [59], heterogeneous structure [60], metastability-engineering strategy [61], micro-banding, and the accumulation of a high density of dislocations in single-phase high-entropy alloys (HEAs) [62], influence how well materials avoid the strength-ductility trade-off dilemma.

Given that the microstructure of sintered 30Co composite (**Figure 4.7b**), which has the highest elongation value among experimental sintered composites, can be classified as lamellar (alternating BF and MA plates), the influence of dual-phase lamellar microstructure on enhancing ductility may be used to explain the increase in elongation value with increasing tensile strength. Recent research has shown that the strength-ductility trade-off of the dual-phase lamellar microstructure was superior to that of the equiaxed microstructure [56].

It has been claimed that necking in the hard phase, whose development was considerably constrained and repressed by the surrounding soft phase, occurred prior to lamellae failure. Thus, it is inferred that such a mechanism would be followed in the failure of sintered composite matrix ausferrite, which exhibits a dual-phase lamellar microstructure comprising hard BF laths and soft austenite sheets.

4.2.3 Surface fracture of sintered alloys after tensile testing

The SEM images of fracture surfaces of sintered 00Co, sintered 15Co, and sintered 30Co alloys after tensile testing are shown in **Figure 4.12**. As can be seen from the figure, the fracture surface of sintered without Co addition is significantly different from sintered with 3.0 wt.% of Co addition, while it has a similar surface fracture feature to sintered with 1.5 wt.% of Co.

The cleavage surface of the sintered 00Co alloy with the lowest elongation value had a cleavage river pattern, but the cleavage and quasi-cleavage patterns were mixed on the fracturing surface of the sintered 30Co alloy. Cleavage fracture, as a characteristic indicator of brittle fracture, was discovered in a pearlite-containing matrix of sintered 00Co alloy, and it was also discovered on the fracture surface of a totally pearlitic eutectoid steel [63]. In contrast, quasi-cleavage displays both cleavage and plastic deformation. This fracture mechanism in the sintered 30Co alloy exhibits high plastic deformation since this alloy has a high strength and low elongation value.

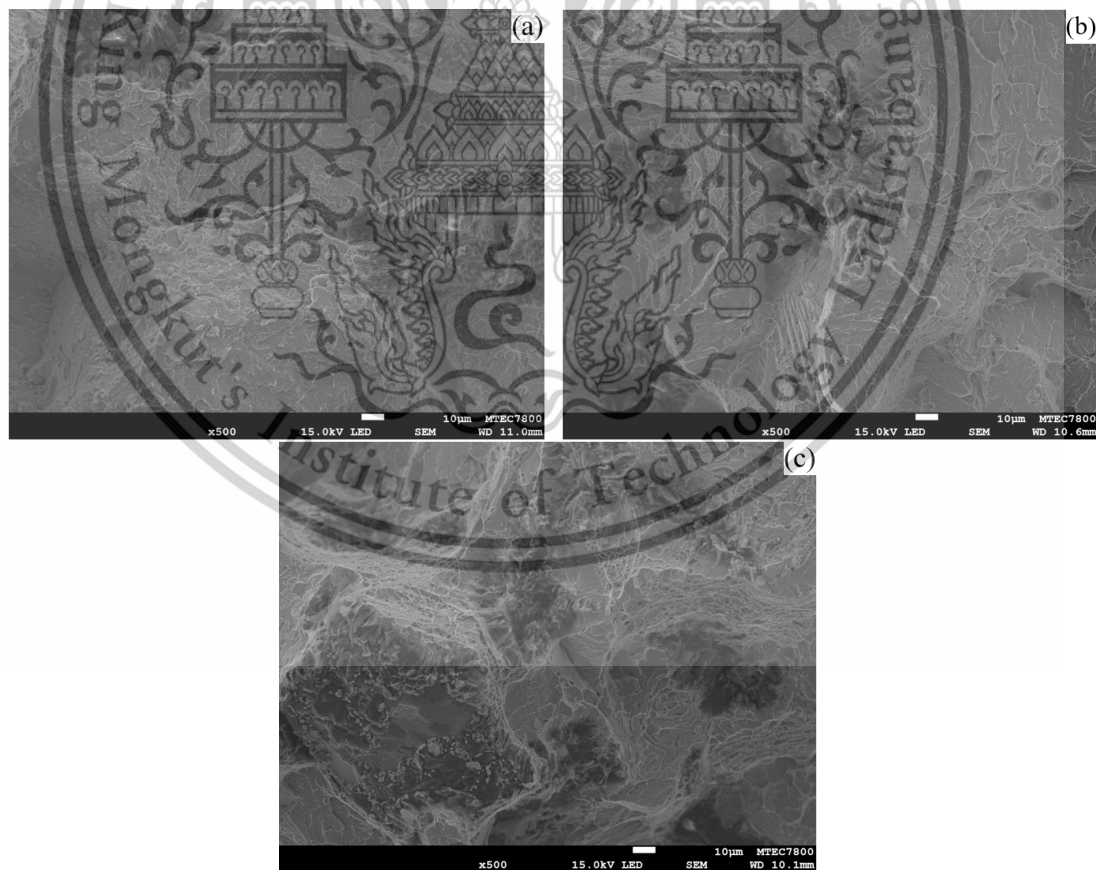


Figure 4.12 SEM images of surface fracture of sintered alloys; (a) 0.0Co alloy, (b) 1.5Co alloy and (c) 3.0Co alloy

4.3 Tribological Properties of Sintered Alloys

4.3.1 Friction coefficient of sintered alloys

Friction coefficient or coefficient of friction (CoF) of all sintered alloys at normal loads of 5N, 10N and 15N is illustrated in **Figure 4.13**. As can be seen from **Figure 4.13**, the friction coefficient of alloys with and without Co addition is not significantly different. At 5N normal load, alloys without Co addition exhibit a greater friction coefficient than those with Co addition, except alloys with 2.0 wt.% Co (sintered 20Co alloy). The average friction coefficient values of all sintered 00Co and 20Co alloys at 5N normal load are 0.53. At 10N normal load, the highest friction coefficient value was observed on sintered alloy with 1.0 wt.% Co addition (sintered 10Co alloy). Sintered 10Co alloys have an average friction coefficient value of 0.55, while the rest of the sintered alloys have an average coefficient value lower than 0.50. For a 15N normal load, there is a fluctuation trend in the coefficient of friction.

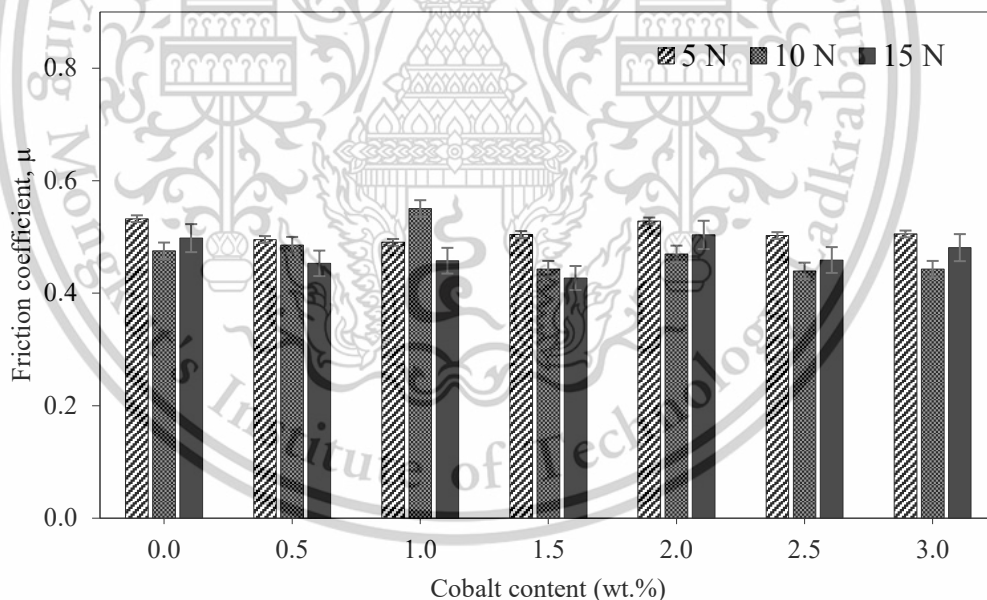


Figure 4.13 Friction coefficient of all sintered alloys at difference normal load

The microstructure of studied sintered alloys showed similar features as the microstructure of austempered ductile iron (ADI). Some discussion can be made by referring to the tribological of ADI. The friction coefficient under a 5N load is higher than a higher normal load (10, 15N), this result is identical to a study by Yuzhou et al.

This material is reserved for educational use only, not allowed for commercial use.

[64]. At high loads (10N and 15N), the coefficient of friction decreased and fluctuated except for sintered 10Co alloy. However, average friction values at 10N and 15N are in the range of 0.45 to 0.55 which is not significantly different. These friction coefficient values fall in the range of friction of conventional ADI under the same or different normal loads as reported [64], [65].

The difference in friction coefficient is mainly dependent on spheroidal graphite since spheroidal graphite has the ability to reduce the friction coefficient. Some investigations suggest that graphite nodules or spheroidal graphite can act as lubricants during tests [66]. At high normal load, the graphite embedded in ADI-like microstructure is easily deformed and peeled off from the matrix as reported in a previous study, hence, distributes on tribosurface. As a consequence, the friction coefficient was decreased with high load. This ruptured phenomenon of the graphite under wear test has also been reported in previous studies on the tribological behavior of ADI (Yuzhou et al., Hua Zhang et al). However, the amount of spherical (nodular) graphite, nodularity of graphite, and embedded matrix constituents also affects the ability of graphite as a lubricant (to reduce friction coefficient).

As observed on the OM images of sintered alloys with less or without Co addition, the number of graphite is not much different compared to high Co addition. Moreover, the graphite shape and its nodularity are not homogeneous and consistence in sintered alloy with low Co addition compare to sintered alloy with high Co addition. However, separate study on the effect of the ability of graphite to act as lubricant in sintered alloy should be conduct in the future.

Nevertheless, strength or hardness was another factor contributing to the peel-off phenomena of graphite during testing. It was usually discovered that friction coefficient rises with matrix hardness, in good agreement with the earlier studies [67], [68]. Hence, the hardness is not taken into account in this case since the hardness values of sintered alloys are not significantly different. According to Yuzhou et al., under mild stresses, the matrix of ADIs with low hardness is barely plastically deformed. As a result, graphite's potential to lower friction was insignificant.

The friction versus distance of each normal load is depicted in **Figure 4.14**, **Figure 4.15**, and **Figure 4.16** respectively. Besides the given friction coefficient value, the friction versus distance graph shows that there are two stages in the test results.

They are the initial and steady stages of the friction coefficient on a 1000 m sliding

This material is reserved for educational use only, not allowed for commercial use.

distance. The initial stage and the stable stage of the wear mechanism are depicted in the results. The initial stage is depicted in the first phase of the graph at a distance of 0 to 100 m, which shows the unstable friction coefficient caused by the initial point-contact between the chromium SKF ball and the sintered composite surface.

This phenomenon in the initial stage of the test is due to point-contact between the surface of the disk specimen and the chromium ball. After a sliding distance of 50m, the friction coefficient decreases. This decreased due to the change of contact from point to surface contact. The change from point to surface contact phenomena is attributed to the flake-off of graphite particles, which has already been reported and explained in this study [69]. Nevertheless, the effect of Co addition on the friction coefficient of sintered steels has not been investigated before.

So, the influence of Co addition in this study might not be well elaborated. The Co addition up to 3.0 wt.% seems to have an insensitive effect on the friction coefficient of the sintered alloys. The high friction coefficient value is strongly dependent on the bainitic microstructure, as reported in a previous study [70]. As observed on the OM images of sintered alloys with less or without Co addition, the number of graphite is not much different compared to high Co addition.

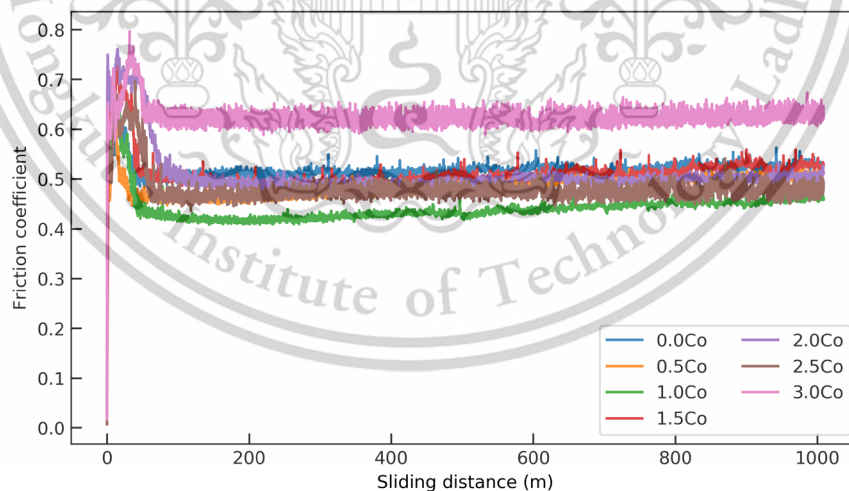


Figure 4.14 Friction coefficient versus sliding distance at normal load 5N

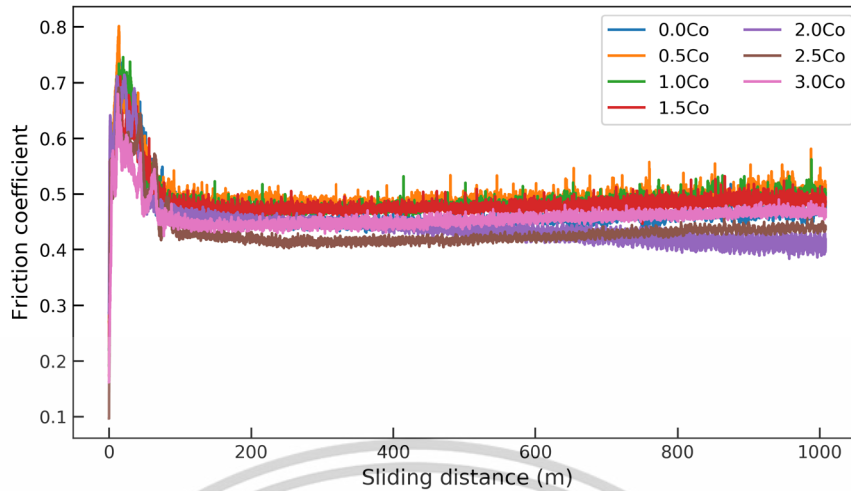


Figure 4.15 Friction coefficient versus sliding distance at normal load 10

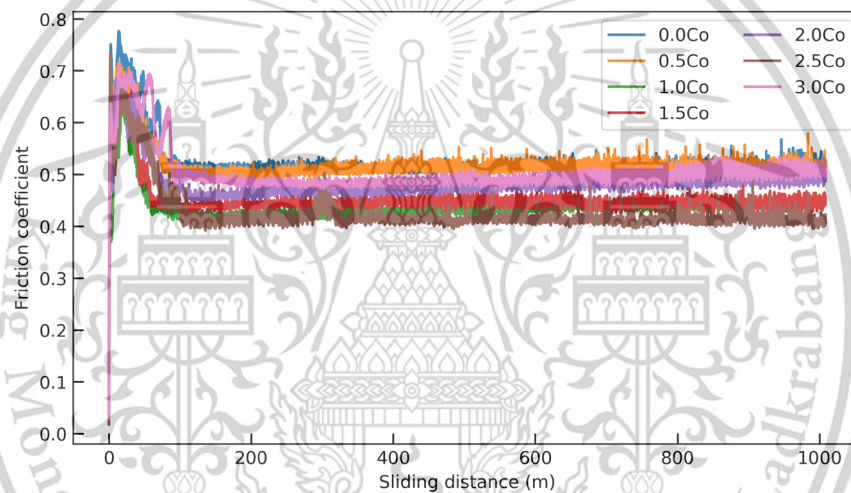


Figure 4.16 Friction coefficient versus sliding distance at normal load 15N

4.3.2 Wear rate of sintered alloys

Wear rate values of all studied sintered Fe-4.00Ni-0.50Mo-0.20Mn-Si-C-Co alloys under different normal loads are listed in **Table 4.3**. Wear rates demonstrate the effect of the coefficient of friction as a function of sliding distance. Wear rate values are determined under the mentioned dry sliding test condition (sliding speed of 0.1 m/s for 1000 m of sliding distance). Since the mass loss on the disk specimens is not significant, the wear rate is derived following the ASTM G99 standard. The wear rate value is strongly dependent on the volume loss of the test specimen.

As can be seen at a normal load of 15N, the wear rate values are significantly higher than the wear rate at a normal load of 10N. It can be stated that at the same

sliding distance, when the normal load increases, the wear rate increases since the surface of disk specimens is subjected to a high-stress concentration with the chromium ball. As a result, more volume loss can be observed at higher normal loads, even with the naked-eye inspection. This phenomenon is known as the thermal softening of material. It is caused by an increase in normal load, which leads to crack propagation and then the formation of wear debris (wear fragments).

Table 4.3 Wear rate value of sintered Fe-4.00Ni-0.50Mo-Si-C at specific normal load under different Cobalt additions

Co content (wt.%)	Wear rate at specific normal loads ((mm ³ /m) × 10 ⁻³)		
	5N	10N	15N
0.0Co	0.458	1.073	1.503
0.5Co	0.507	0.820	1.229
1.0Co	0.376	1.101	1.468
1.5Co	0.560	0.899	1.384
2.0Co	0.549	1.111	1.858
2.5Co	0.587	1.255	1.360
3.0Co	0.583	0.865	1.693

Figure 4.17 illustrates the effect of different normal loads on wear rate on sintered Fe-4.00Ni-0.50Mo-0.20Mn-Si-C with different Co content. This plot indicates that at the highest normal load of 15N, the specimen exhibits a higher wear rate than at the lowest normal load of 5N. However, the effect of Co on wear rate is not understood since the wear rate value does not increase or decrease as Co content increases. For instance, at normal load 5N, there is no significant difference in wear rate value among all sintered alloys; however, sintered 10Co alloy had the lowest wear rate value. At normal load 10N, the wear rate value fluctuated. The lowest wear rate value is observed on the sintered 05Co alloy, while the sintered 25Co alloy has the highest wear rate value. For a normal load of 15N, the wear rate value fluctuates among sintered alloys. The wear rate values of sintered 00Co, sintered 10Co, sintered 15Co alloy, and sintered 25Co alloy are slightly different while sintered 20Co alloy exhibits the highest wear rate value.

According to these mentioned values, it is difficult to describe the influence of Co addition on sintered Fe-4.00Ni-0.50Mo-0.20Mn-Si-C alloy in terms of wear rate value. One more important factor worth mentioning is the actual wear rate value. Since the wear rate value is too small, a slight difference can be negligible.

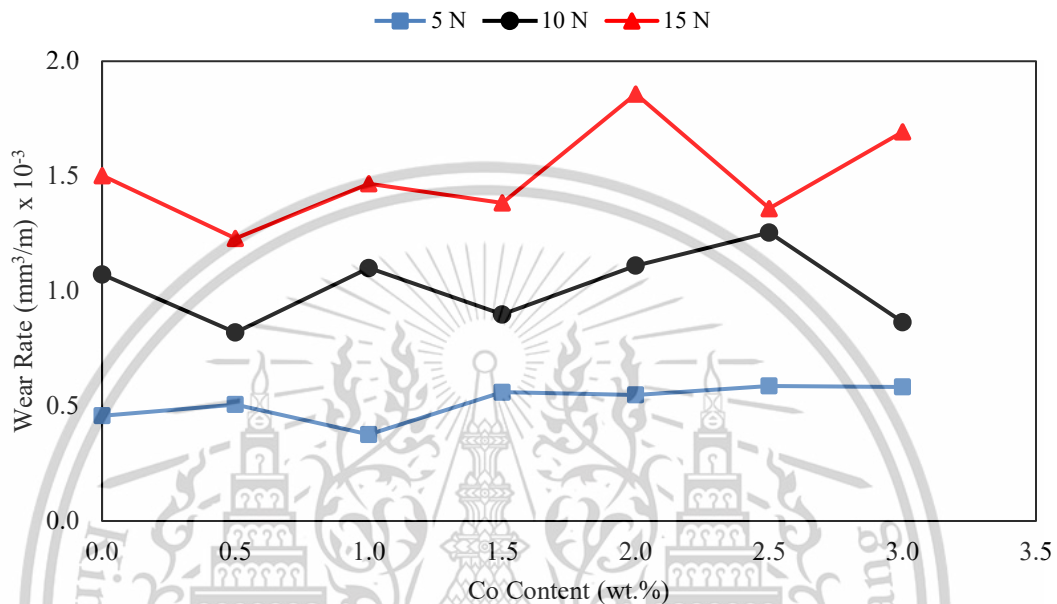


Figure 4.17 Wear rate at specific normal load of sintered Fe-4.00Ni-0.50Mo-0.20Mn-Si-C versus Co contents

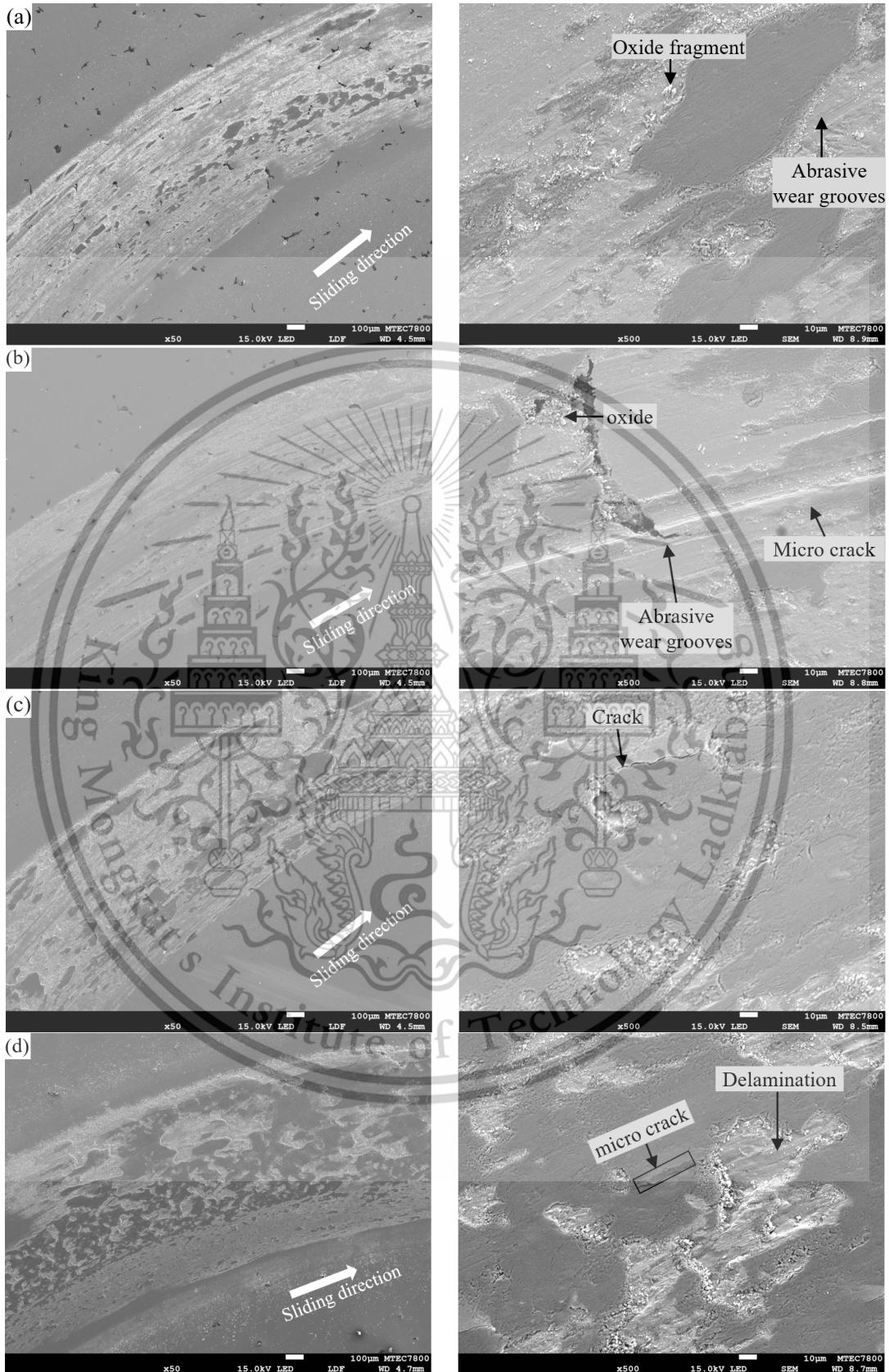
4.3.3 Worn surface of all sintered alloys at 5N normal load

Figure 4.18 shows the SEM micrographs of the worn surface of sintered Fe-4.00Ni-0.50Mo-0.20Mn-Si-C alloys under 5N normal load. From SEM micrographs, two types of wear mechanisms, namely abrasive and fatigue wear, were observed. Abrasive wear occurs as a result of sliding against a hard surface under normal pressure, leading to plastic deformation and scratching on the outer layer as abrasive grooves [71], [72]. This wear process also happens when hard particles or surfaces glide or roll over a softer surface, causing the material to be removed by scratching or plowing.

On the other hand, fatigue wear formation begins with cracks and fissures that develop on the material's surface; the fracture is caused by strain that accumulates on the surface by repetitive sliding on the surface.

Low Magnification (50X)

High Magnification (500X)



This material is reserved for educational use only, not allowed for commercial use.

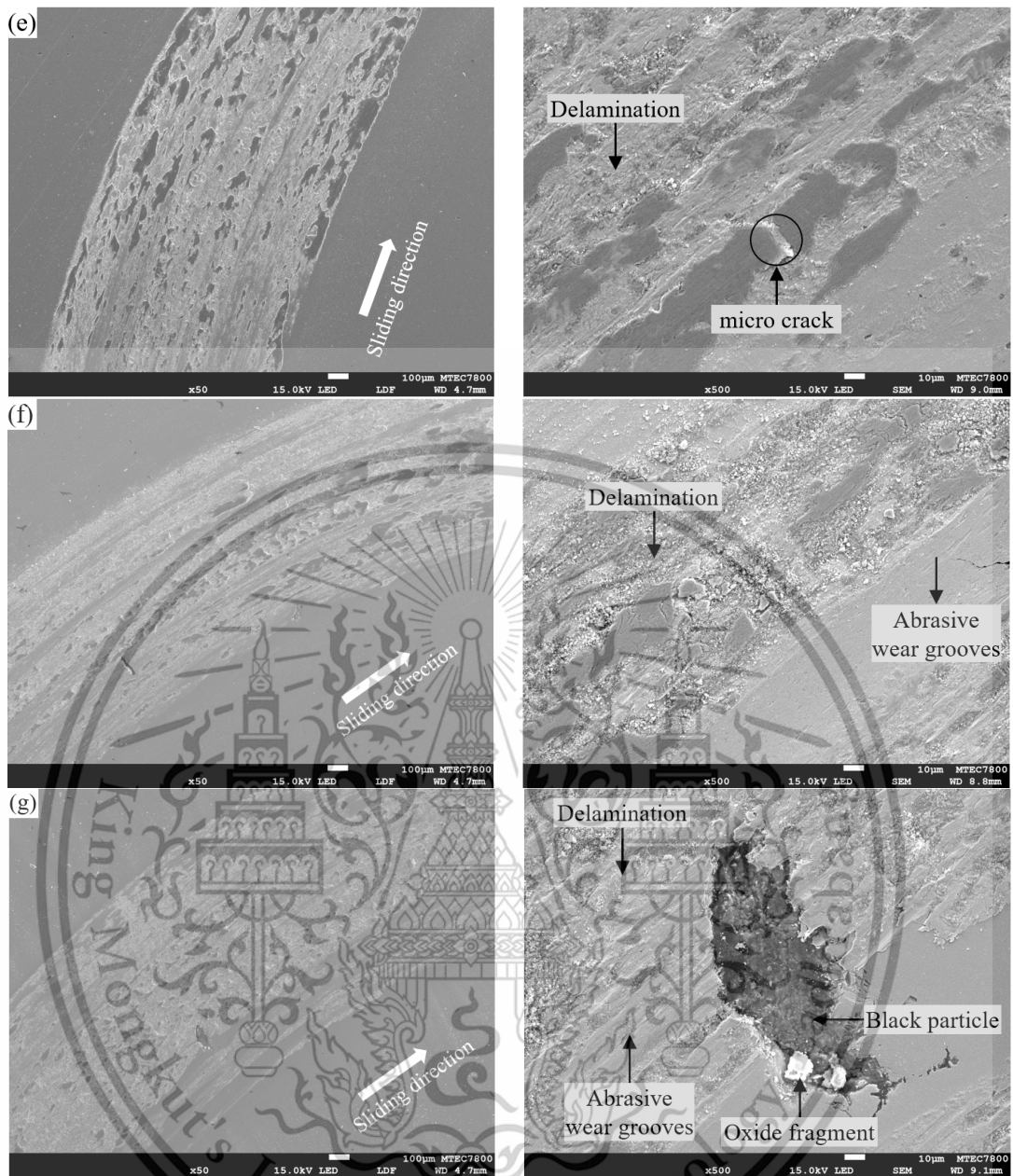
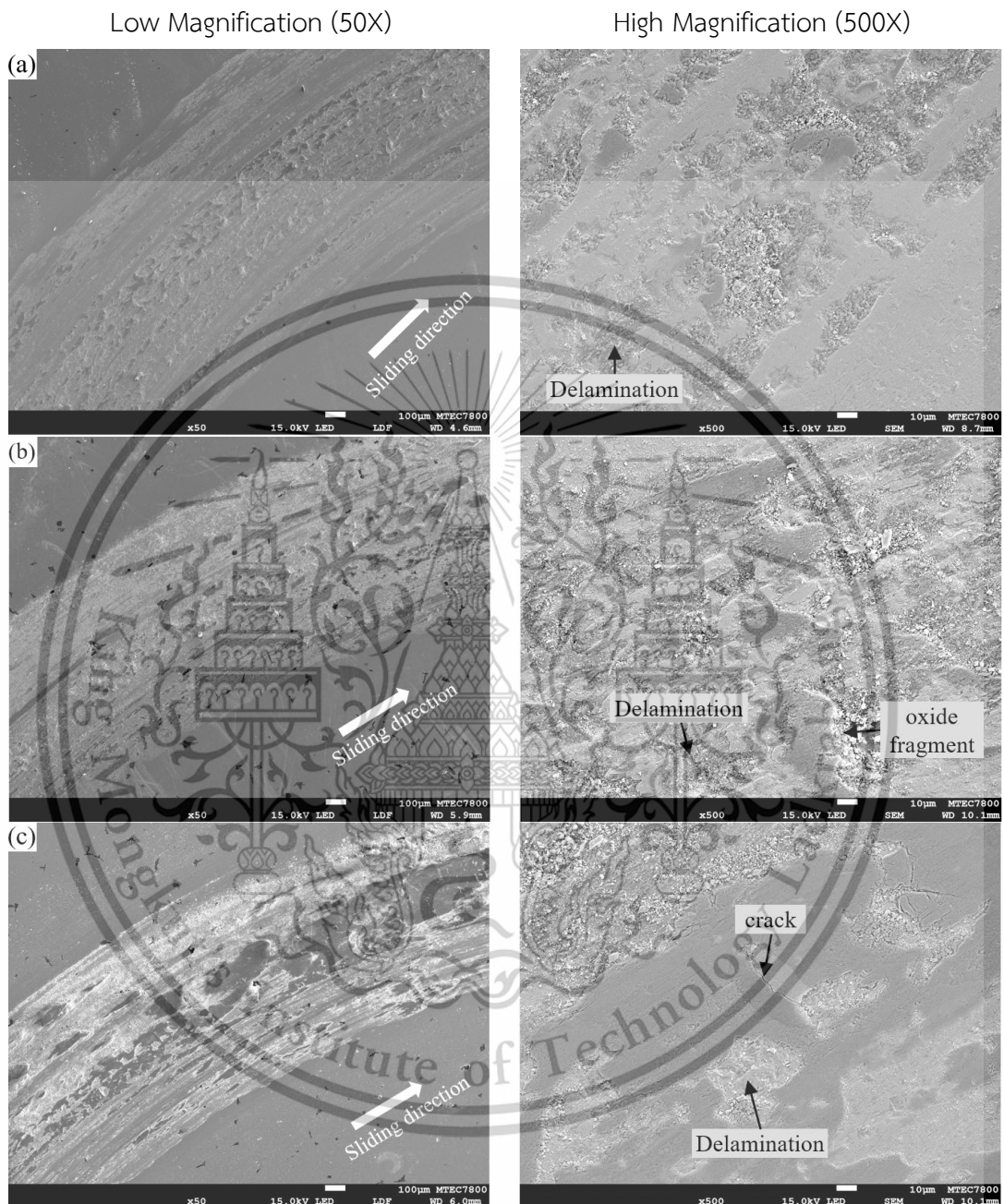


Figure 4.18 SEM micrograph of worn surface of all sintered alloys at 5N normal load

4.3.4 Worn surface of all sintered alloys at 10N normal load

SEM micrographs of the worn surface of sintered Fe-4.00Ni-0.50Mo-0.20Mn-Si-C alloys at 10N normal load are illustrated with low and high magnification in **Figure 4.19**. Abrasive and fatigue wear mechanisms are clearly observed in all sintered alloys. At 10N normal load, the surface of the disc specimen after testing is mildly damaged, while wear delamination is clearly found in each sintered alloy with a difference in Co

content. Oxidation occurred during or after testing since oxide formations are observed within wear debris.



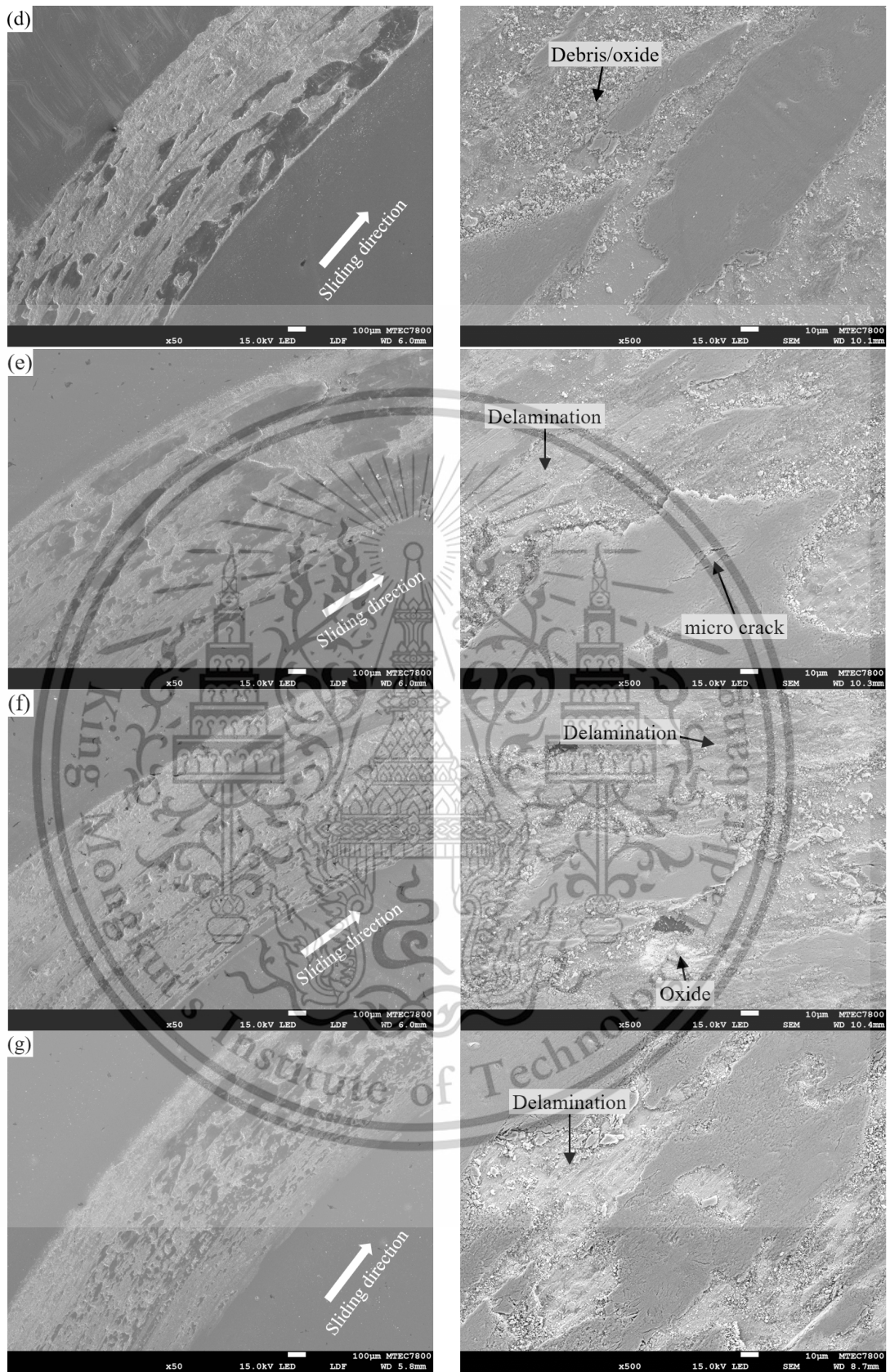
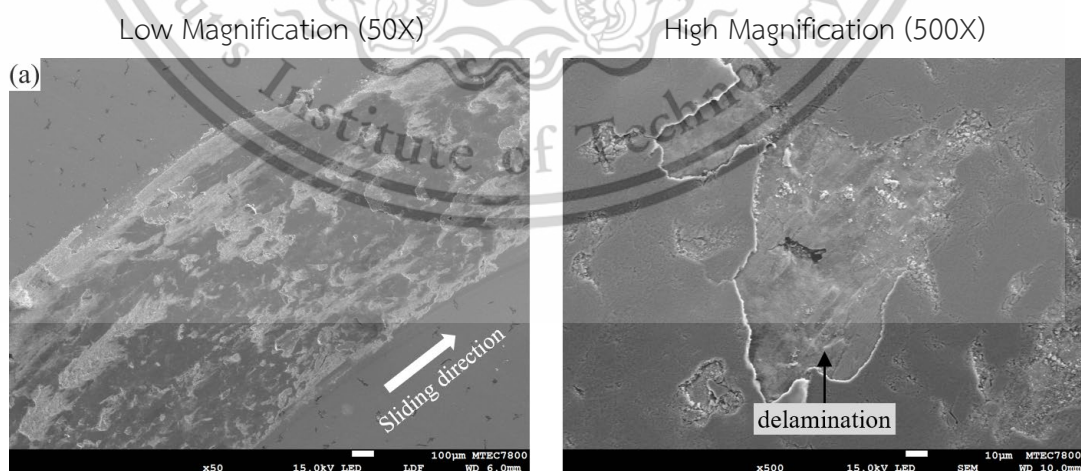


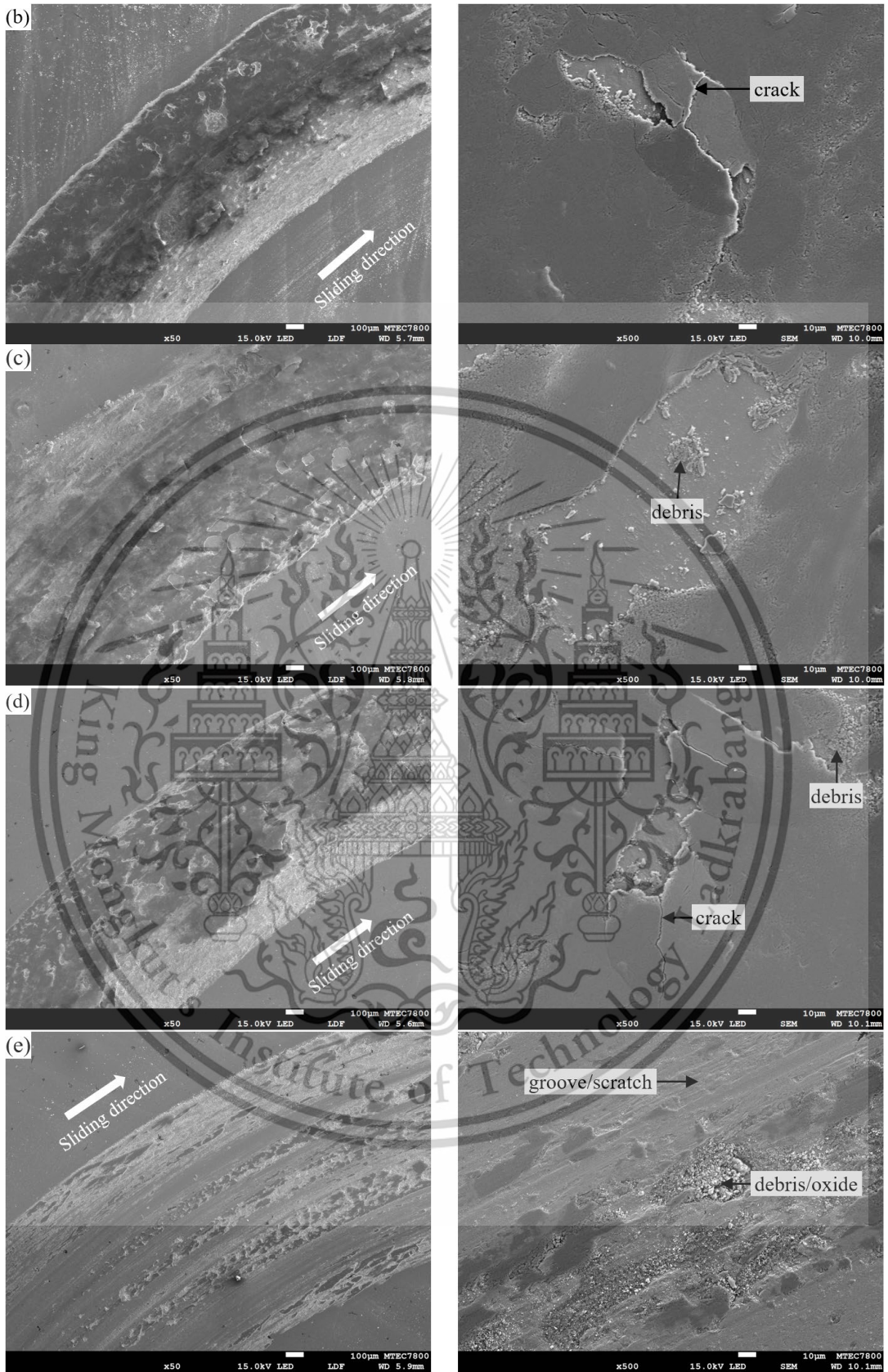
Figure 4.19 SEM micrograph of worn surface of all sintered alloys at 10N normal load

4.3.5 Worn surface of all sintered alloys at 15N normal load

The worn surface of sintered Fe-4.00Ni-0.50Mo-0.20Mn-Si-C alloys at 15N normal load is depicted in **Figure 4.20**. From SEM images at low magnification, the surface of the disc specimens was severely damaged. Microcracks on the surface of disc specimens, which lead to crack propagation and surface delamination, are observed on specimens with relatively low Co content, as can be seen in high magnification SEM micrographs. Adhesive wear mechanisms were also found alongside abrasive and fatigue mechanisms. Severe delamination was also observed on the worn surface of all sintered alloys under normal load 15N. It resulted from the surface softening as thermal energy was stretched along the sliding direction. Furthermore, the worn surface of all sintered composites illustrates the oxide agglomerates, which refer to oxidative wear [73].

According to the observations from worn surface micrographs, the amount of surface damage decreases as cobalt (Co) content increases. This is due to the fact that the specimen's coefficient of friction lowers as the amount of Co content increases, which might result in reduced shear stresses on the material's subsurface layer while sliding. Lower shear stresses, according to this theory, result in lessening the occurrence and development of subsurface cracks and minimizing the delamination mechanism. Due to the better material resistance to fracture propagation, the volume loss reduces with increasing Co concentration.





This material is reserved for educational use only, not allowed for commercial use.

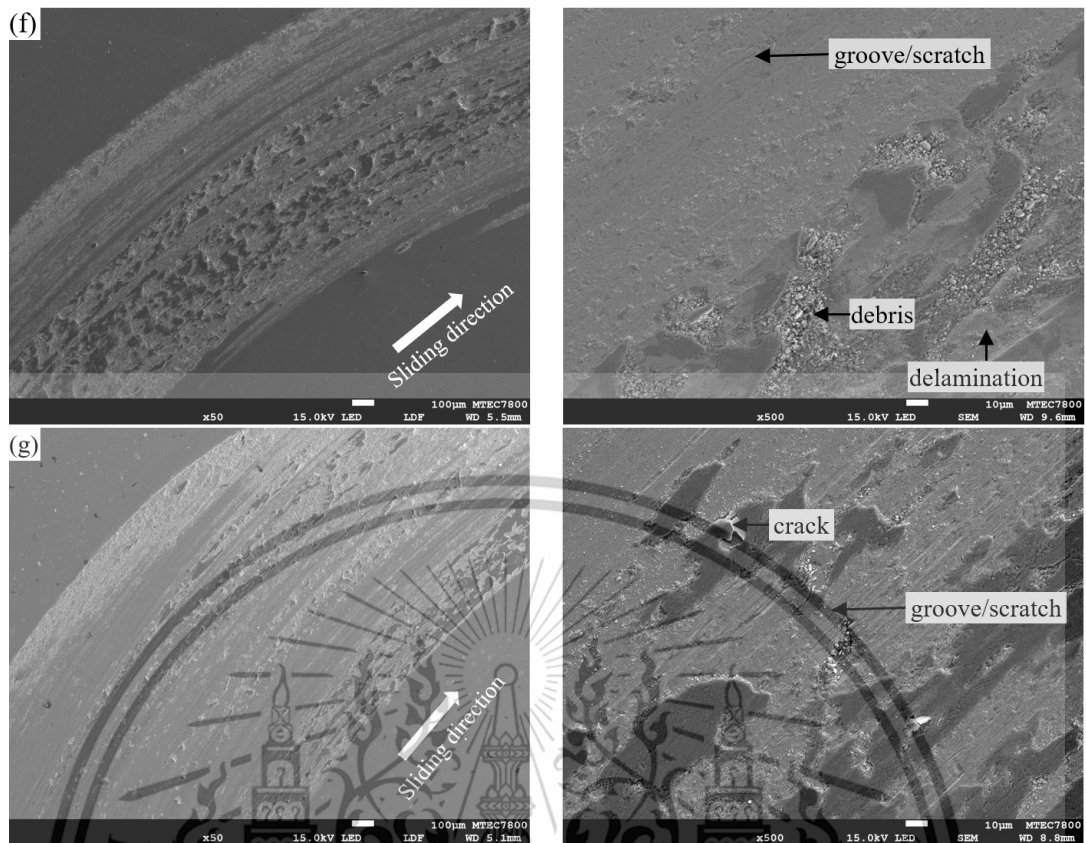
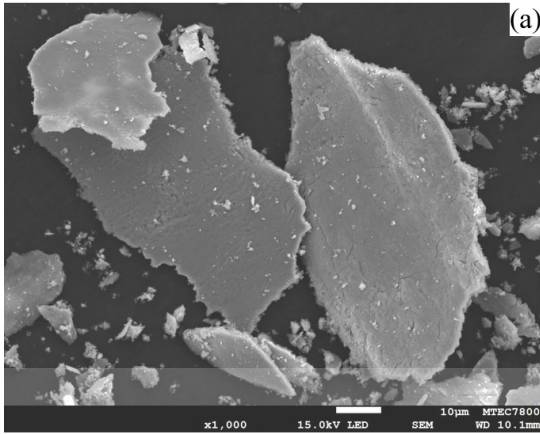


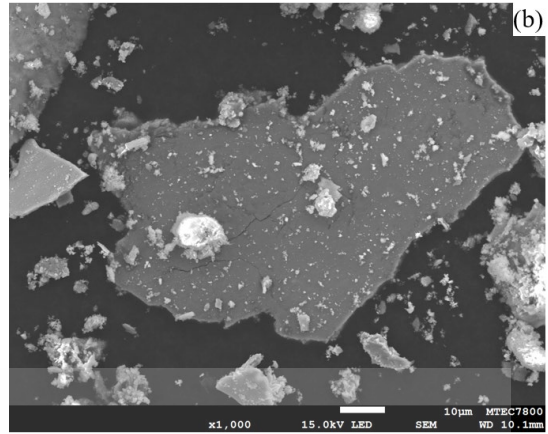
Figure 4.20 SEM micrograph of worn surface of all sintered alloys at 15N normal load

4.3.6 Wear debris of all sintered alloys at 15N normal load

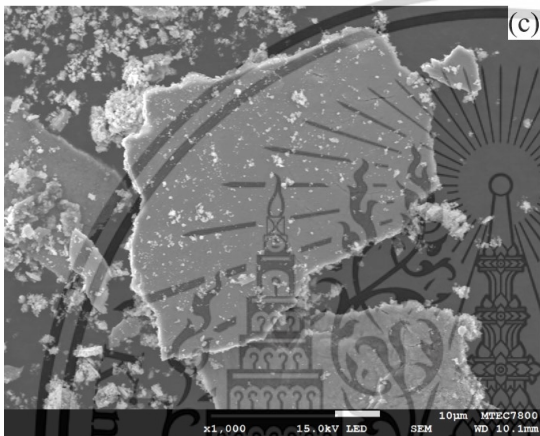
SEM micrographs of wear debris of sintered Fe-4.00Ni-0.50Mo-0.20Mn-Si-C alloys with and without Co addition after a wear test at a 15N normal load are depicted in Figure 4.21. The wear debris is the result of continuous friction between the disc specimen and the countermaterial chromium ball. The debris of sintered Fe-4.00Ni-0.50Mo-0.20Mn-Si-C alloys with and without Co addition shows an irregular shape, which is formed by the wear delamination. Wear delamination is commonly caused by mild to severe plastic deformation during sliding. Oxide formations are also found in wear debris. Moreover, wear debris of sintered alloy with Co addition seems to have a large plate-like formation or structure which is an indication of an adhesive wear mechanism [74]. The wear debris shape of sintered alloys at 10N and 5N normal loads is similar to wear debris at 15N normal loads. Thus, more SEM micrographs of each sintered alloy at 10N and 5N normal loads are shown in Appendix A.



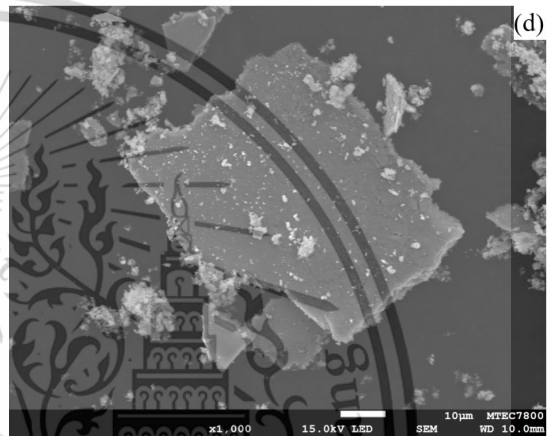
(a) 0.0Co sintered alloy



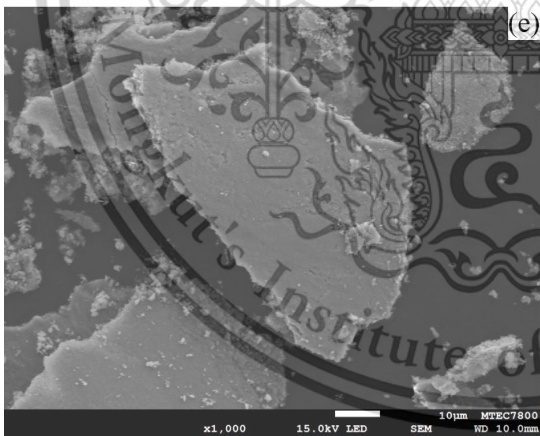
(b) 0.5Co sintered alloy



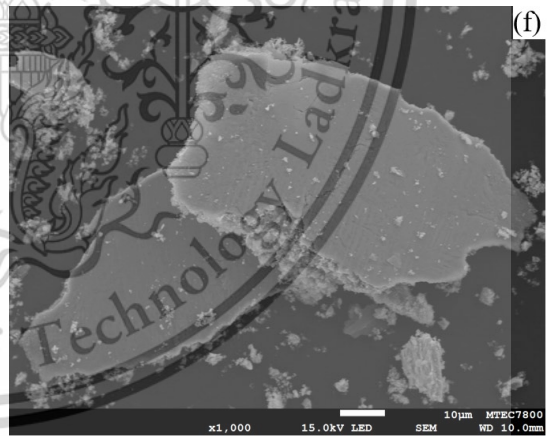
(c) 1.0Co sintered alloy



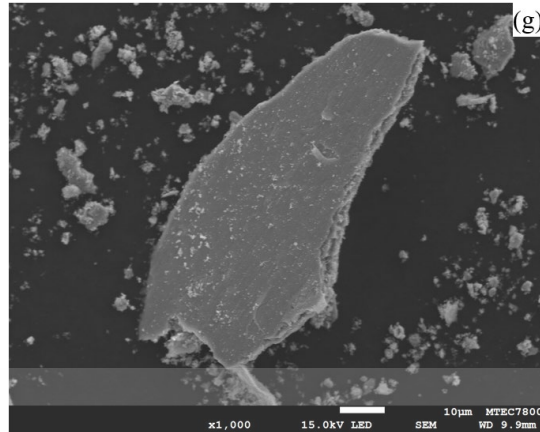
(d) 1.5Co sintered alloy



(e) 2.0Co sintered alloy



(f) 2.5Co sintered alloy



(f) 3.0Co sintered alloy

Figure 4.21 SEM micrograph of wear debris at all sintered alloys at 15N normal load

4.3.7 EDS inspection of wear debris at 15N normal load

EDS spectrum of wear debris of sintered Fe-4.00Ni-0.50Mo-0.20Mn-Si-C alloys with 0.0Co, 1.5Co, and 3.0Co content at normal load 15N are displayed in Figure 4.22, Figure 4.23, and Figure 4.24 respectively. EDS of other Co content can be found in Appendix A. The wear debris of all Co addition composites has a strong oxygen peak, which relates to iron oxide from oxidative wear, and a weak chromium peak, which refers to counterball surface debris.

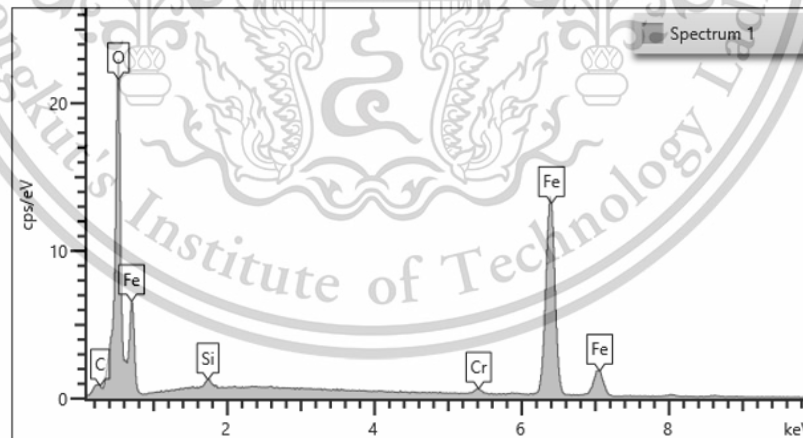


Figure 4.22 EDS of wear debris of sintered 00Co alloy

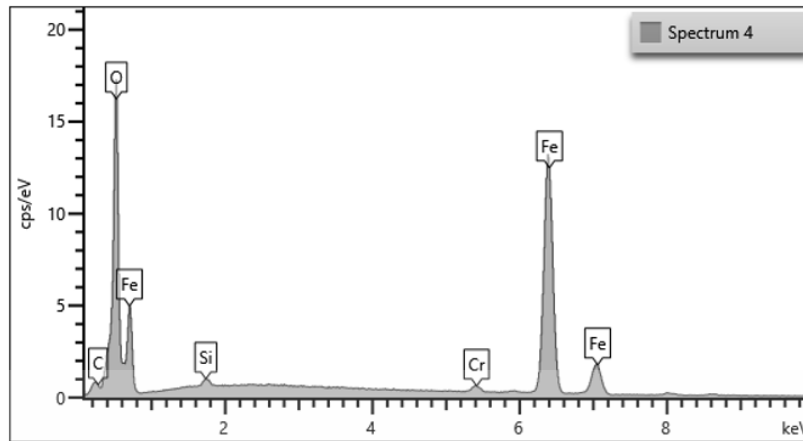


Figure 4.23 EDS of wear debris of sintered 15Co alloy

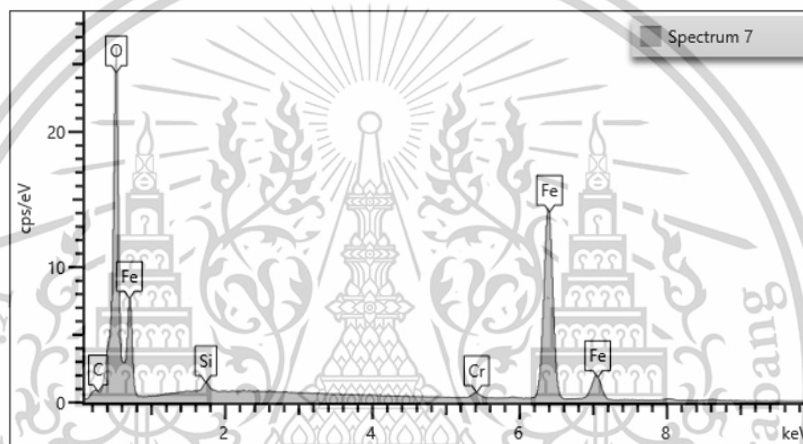


Figure 4.24 EDS of wear debris of sintered 30Co alloy

CHAPTER 5

CONCLUSIONS AND RECOMMENDATION

5.1 Conclusion

The current work investigates the effects of cobalt addition on the microstructure, mechanical properties, tribological properties (including friction coefficient and wear behavior) of sintered Fe-0.50Mo-0.20Mn-4.00Ni-Si-C alloys. The key discovery from the experimental findings is outlined below.

- 1) Cobalt addition accelerated bainitic transformation. This acceleration gradually replaced the martensite blocks with an ausferrite structure (BF + RA mixture).
- 2) The sintered alloys with the austempered ductile iron-like (ADI) microstructure (graphite nodules plus ausferrite) could be produced by adding Co content of 2.0 wt.% or more.
- 3) The tensile strength and elongation values of the sintered alloys increased with increasing Co content. High elongation values of up to 7-9% could be achieved by using a Co content of up to 3.0 wt.%. There is no strength-ductility trade-off in the sintered Co-added alloys produced in this work.
- 4) Co-addition has no effect on the hardness value of sintered alloys. There is no significant change in the coefficient of friction of sintered alloys at 5N, 10N and 15N normal load.
- 5) At a normal load of 15N, sintered alloys have the highest wear rate value. This is due to the strong delamination caused by wear, which causes crack propagation on the surface of the materials, resulting in strong plastic deformation.
- 6) Three common types of wear mechanisms, abrasive, adhesive and delamination wear, are observed on the worn surface and wear debris of all sintered alloys.
- 7) The worn surface of sintered 30Co alloys seems to have better friction resistance, as their worn surface at 5N, 10N, and 15N is not severe compared to other Co-added alloys.

5.2 Recommendation for Future Work

The study's goal is to improve mechanical properties, especially the elongation value of sintered materials, using available sintering parameters restricted by industries. Co addition can significantly increase the elongation value by promoting lower ausferrite formation. More research on ausferrite formation should be conducted to study the benefits of this microstructure. In addition, impact tests should be conducted to study toughness. A further investigation of the effect of tempering on the studied sintered alloys is expected to enhance the mechanical properties and put the sintered parts into commercial use.



REFERENCES

- [1] S. Chakthin, N. Poolthong, and R. Tongstri, "Effect of Reaction between Fe and Carbide Particles on Mechanical Properties of Fe-Base Composite," *Adv. Mater. Res.*, vol. 55–57, pp. 357–360, Aug. 2008, doi: 10.4028/www.scientific.net/AMR.55-57.357.
- [2] K. Ruangchai *et al.*, "Microstructure, Hardness and Wear Properties of Sintered Fe-Mo-Si-C Steels with Spheroidal Graphite Iron/Compacted Graphite Iron-Like," *Key Eng. Mater.*, vol. 751, pp. 47–52, 2017, doi: 10.4028/www.scientific.net/KEM.751.47.
- [3] K. Ruangchai, A. Wiengmoon, M. Morakotjinda, N. Tosangthum, and R. Tongstri, "Sintered Fe-Mo-Si-C alloys with ductile cast iron microstructure," *J. Phys. Conf. Ser.*, vol. 1144, no. 1, p. 012099, Dec. 2018, doi: 10.1088/1742-6596/1144/1/012099.
- [4] K. Ruangchai, A. Wiengmoon, R. Krataitong, T. Yotkaew, N. Tosangthum, and R. Tongstri, "Pearlitic ductile iron-like sintered Fe-Cr-Mo-Si-C alloys," *J. Phys. Conf. Ser.*, vol. 1144, no. 1, p. 012147, Dec. 2018, doi: 10.1088/1742-6596/1144/1/012147.
- [5] J. Zhao, "Thermomechanical processing of advanced high strength steels," *Prog. Mater. Sci.*, vol. 94, pp. 174–242, Jan. 2018, doi: 10.1016/j.pmatsci.2018.01.006.
- [6] G. Jha, S. Das, S. Sinha, A. Lodh, and A. Haldar, "Design and development of precipitate strengthened advanced high strength steel for automotive application," *Mater. Sci. Eng. A*, vol. 561, pp. 394–402, Jan. 2013, doi: 10.1016/j.msea.2012.10.047.
- [7] T. Kaewkam *et al.*, "Sintered Fe-Ni-Si-C alloys," *IOP Conf. Ser. Mater. Sci. Eng.*, vol. 1137, no. 1, p. 012035, May 2021, doi: 10.1088/1757-899X/1137/1/012035.
- [8] H. K. D. H. Bhadeshia, "Nanostructured bainite," *Proc. R. Soc. Math. Phys. Eng. Sci.*, vol. 466, no. 2113, pp. 3–18, Jan. 2010, doi: 10.1098/rspa.2009.0407.
- [9] C. Garcia-Mateo, F. G. Caballero, and H. K. D. H. Bhadeshia, "Development of Hard Bainite," *ISIJ Int.*, vol. 43, no. 8, pp. 1238–1243, 2003, doi: 10.2355/isijinternational.43.1238.
- [10] F. G. Caballero and H. K. D. H. Bhadeshia, "Very strong bainite," *Curr. Opin. Solid State Mater. Sci.*, vol. 8, no. 3, pp. 251–257, Jun. 2004, doi: 10.1016/j.cossms.2004.09.005.
- [11] C. Garcia-Mateo, F. G. Caballero, and H. K. D. H. Bhadeshia, "Acceleration of Low-temperature Bainite," *ISIJ Int.*, vol. 43, no. 11, pp. 1821–1825, 2003, doi: 10.2355/isijinternational.43.1821.
- [12] T. Tsutsui, "Recent Technology of Powder Metallurgy and Applications".

- [13] P. Ramakrishnan, "17 - Automotive applications of powder metallurgy," in *Advances in Powder Metallurgy*, I. Chang and Y. Zhao, Eds., in Woodhead Publishing Series in Metals and Surface Engineering. , Woodhead Publishing, 2013, pp. 493–519. doi: 10.1533/9780857098900.4.493.
- [14] J. T. Black and R. A. Kohser, "*Powder Metallurgy (Particulate Processing)*", in *DeGarmo's materials and processing in manufacturing*, Thirteenth edition. Hoboken: Wiley, 2019.
- [15] A. Aytimur, S. Koçyiğit, and İ. Uslu, "Calcium Stabilized Ceria Doped Zirconia Nanocrystalline Ceramic," *J. Inorg. Organomet. Polym. Mater.*, vol. 24, no. 6, pp. 927–932, Nov. 2014, doi: 10.1007/s10904-014-0064-6.
- [16] G. N. Haidemenopoulos, "'Physical metallurgy of Steels', Physical Metallurgy".
- [17] T. Islam and H. M. M. A. Rashed, "Classification and Application of Plain Carbon Steels," in *Reference Module in Materials Science and Materials Engineering*, Elsevier, 2019, p. B9780128035818103000. doi: 10.1016/B978-0-12-803581-8.10268-1.
- [18] H. K. D. H. Bhadeshia, "*Aspects of kinetic theory*", *Theory of transformations in steels*. Boca Raton: CRC Press, 2021.
- [19] "Metallography of Steels." Accessed: Apr. 26, 2023. [Online]. Available: http://www.phase-trans.msm.cam.ac.uk/2008/Steel_Microstructure/SM.html
- [20] R. Manna, "Time Temperature Transformation (TTT) Diagrams".
- [21] M. Takahashi, "Recent progress: kinetics of the bainite transformation in steels," *Curr. Opin. Solid State Mater. Sci.*, vol. 8, no. 3–4, pp. 213–217, Jun. 2004, doi: 10.1016/j.cossms.2004.08.003.
- [22] F. Caballero, M. Miller, S. Babu, and C. Garciamateo, "Atomic scale observations of bainite transformation in a high carbon high silicon steel," *Acta Mater.*, vol. 55, no. 1, pp. 381–390, Jan. 2007, doi: 10.1016/j.actamat.2006.08.033.
- [23] J. I. Verdeja González, D. Fernández-González, and L. F. Verdeja González, *Physical Metallurgy and Heat Treatment of Steel*. in "Solid-State Transformation in the Iron Carbon System", Topics in Mining, Metallurgy and Materials Engineering. Cham: Springer International Publishing, 2023. doi: 10.1007/978-3-031-05702-1.
- [24] M. Maalekian, "The Effects of Alloying Elements on Steels".
- [25] G. E. Totten, "*Effects of Alloying Elements on the Heat Treatment of Steel*", *Steel Heat Treatment: Metallurgy and Technologies*. CRC Press, 2006.

- [26] F. Hu, K. M. Wu, and A. Shirzadi, "Influence of Co and Al on pearlitic transformation in superbainitic steels," *Ironmak. Steelmak.*, vol. 39, pp. 535–539, Oct. 2012, doi: 10.1179/1743281211Y.0000000092.
- [27] G. Arici, M. Acarer, and M. Uyaner, "Effect of Co addition on microstructure and mechanical properties of new generation 3Cr-3W and 5Cr-3W steels," *Eng. Sci. Technol. Int. J.*, vol. 24, no. 4, pp. 974–989, Aug. 2021, doi: 10.1016/j.jestch.2020.12.025.
- [28] C. García-Mateo and F. G. Caballero, "The Role of Retained Austenite on Tensile Properties of Steels with Bainitic Microstructures," *Mater. Trans.*, vol. 46, no. 8, pp. 1839–1846, 2005, doi: 10.2320/matertrans.46.1839.
- [29] J. Yang, H. Qiu, P. Xu, H. Yu, and Y. Wang, "The substitution of aluminum for cobalt in nanostructured bainitic steels," presented at the MATERIALS SCIENCE, ENERGY TECHNOLOGY AND POWER ENGINEERING II (MEP2018), Hangzhou, China, 2018, p. 020001. doi: 10.1063/1.5041096.
- [30] Y. Yao and Y. Zhou, "Effects of Deep Cryogenic Treatment on Wear Resistance and Structure of GB 35CrMoV Steel," *Metals*, vol. 8, p. 502, Jun. 2018, doi: 10.3390/met8070502.
- [31] G02 Committee, "Test Method for Wear Testing with a Pin-on-Disk Apparatus," ASTM International. doi: 10.1520/G0099-17.
- [32] B. Bhushan, *Introduction to Tribology*. John Wiley & Sons, 2013.
- [33] R. Aghababaei, D. H. Warner, and J.-F. Molinari, "Critical length scale controls adhesive wear mechanisms," *Nat. Commun.*, vol. 7, p. 11816, Jun. 2016, doi: 10.1038/ncomms11816.
- [34] A. ASTM, "Standard terminology relating to wear and erosion," *G40*, 2013.
- [35] J.-F. Molinari, R. Aghababaei, T. Brink, L. Frérot, and E. Milanese, "Adhesive wear mechanisms uncovered by atomistic simulations," *Friction*, vol. 6, pp. 245–259, Sep. 2018, doi: 10.1007/s40544-018-0234-6.
- [36] W. Kuang, Q. Miao, W. Ding, and H. Li, "A short review on the influence of mechanical machining on tribological and wear behavior of components," *Int. J. Adv. Manuf. Technol.*, vol. 120, May 2022, doi: 10.1007/s00170-022-08895-w.
- [37] N. Chawla and X. Deng, "Microstructure and mechanical behavior of porous sintered steels," *Mater. Sci. Eng. A*, vol. 390, no. 1, pp. 98–112, Jan. 2005, doi: 10.1016/j.msea.2004.08.046.

- [38] P. Głowacz, M. Tenerowicz-aba, M. Sułowski, and J. Konstanty, “Sintered Fe-Mn-Si-C Steels”.
- [39] M. Sulowski, “Sintered Structural Steels Containing Mn, Cr And Mo—The Summary of the Investigations,” *Powder Metall. Prog.*, vol. 16, no. 2, pp. 59–85, 2016.
- [40] J. You *et al.*, “Effects of molybdenum addition on microstructure and mechanical properties of Fe-B-C sintered alloys,” *Mater. Charact.*, vol. 173, p. 110915, Mar. 2021, doi: 10.1016/j.matchar.2021.110915.
- [41] W. Srijampan *et al.*, “Microstructure and mechanical property of sintered Fe-Cr-Mo steels due to phase transformations with fast cooling rates,” *Mater. Des.*, vol. 88, pp. 693–701, Dec. 2015, doi: 10.1016/j.matdes.2015.09.030.
- [42] T. Nithimethakul *et al.*, “The effect of molybdenum on the microstructure and mechanical behaviour of the sintered Fe-Mo-Mn-Si-C composite,” *IOP Conf. Ser. Mater. Sci. Eng.*, vol. 1137, no. 1, p. 012028, May 2021, doi: 10.1088/1757-899X/1137/1/012028.
- [43] P. HG and A. Xavior, “Processing of Graphene/CNT-Metal Powder,” 2018. doi: 10.5772/intechopen.76897.
- [44] S. G. Lee *et al.*, “Effects of Ni and Mn addition on critical crack tip opening displacement (CTOD) of weld-simulated heat-affected zones of three high-strength low-alloy (HSLA) steels,” *Mater. Sci. Eng. A*, vol. 697, pp. 55–65, Jun. 2017, doi: 10.1016/j.msea.2017.04.115.
- [45] J. D. Verhoeven and E. D. Gibson, “The divorced eutectoid transformation in steel,” *Metall. Mater. Trans. A*, vol. 29, no. 4, pp. 1181–1189, Apr. 1998, doi: 10.1007/s11661-998-0245-4.
- [46] M.-X. Zhang and P. M. Kelly, “The morphology and formation mechanism of pearlite in steels,” *Mater. Charact.*, vol. 60, no. 6, pp. 545–554, Jun. 2009, doi: 10.1016/j.matchar.2009.01.001.
- [47] “Second Stage of Upper Bainite in a 0.3 Mass Pct C Steel | SpringerLink.” Accessed: May 10, 2023. [Online]. Available: <https://link.springer.com/article/10.1007/s11661-016-3902-z>
- [48] M. J. Santofimia, F. G. Caballero, C. Capdevila, C. García-Mateo, and C. G. de Andrés, “New Model for the Overall Transformation Kinetics of Bainite. Part 1: the Model,” *Mater. Trans.*, vol. 47, no. 10, pp. 2465–2472, 2006, doi: 10.2320/matertrans.47.2465.

- [49] C. Garcia-Mateo and F. G. Caballero, "Ultra-high-strength Bainitic Steels," *ISIJ Int.*, vol. 45, no. 11, pp. 1736–1740, 2005, doi: 10.2355/isijinternational.45.1736.
- [50] F. Hu, K.-M. Wu, and H. Zheng, "Influence of Co and Al on Bainitic Transformation in Super Bainitic Steels," *Steel Res. Int.*, vol. 84, no. 10, pp. 1060–1065, 2013, doi: 10.1002/srin.201200334.
- [51] T. Sourmail and V. Smanio, "Influence of Cobalt on Bainite Formation Kinetics in 1 Pct C Steel," *Metall. Mater. Trans. A*, vol. 44, no. 5, pp. 1975–1978, May 2013, doi: 10.1007/s11661-013-1656-4.
- [52] S. Chen, C. Wang, L. Shan, X. Zhao, and W. Xu, "Effect of isothermal time and alloy elements on bainitic transformation below Ms in medium Mn Steels," *IOP Conf. Ser. Mater. Sci. Eng.*, vol. 592, no. 1, p. 012018, Aug. 2019, doi: 10.1088/1757-899X/592/1/012018.
- [53] C. Capdevila, F. G. Caballero, and C. G. de Andrés, "Determination of Ms Temperature in Steels: A Bayesian Neural Network Model," *ISIJ Int.*, vol. 42, no. 8, pp. 894–902, 2002, doi: 10.2355/isijinternational.42.894.
- [54] C. Garcia-Mateo *et al.*, "Transferring Nanoscale Bainite Concept to Lower C Contents: A Perspective," *Metals*, vol. 7, no. 5, Art. no. 5, May 2017, doi: 10.3390/met7050159.
- [55] W. Bleck, X. Guo, and Y. Ma, "The TRIP Effect and Its Application in Cold Formable Sheet Steels," *Steel Res. Int.*, vol. 88, no. 10, p. 1700218, 2017, doi: 10.1002/srin.201700218.
- [56] Y. F. Gao, W. Zhang, P. J. Shi, W. L. Ren, and Y. B. Zhong, "A mechanistic interpretation of the strength-ductility trade-off and synergy in lamellar microstructures," *Mater. Today Adv.*, vol. 8, p. 100103, Dec. 2020, doi: 10.1016/j.mtadv.2020.100103.
- [57] A. K. Srivastava, N. K. Patel, B. Ravi Kumar, A. Sharma, and B. Ahn, "Strength-Ductility Trade-Off in Dual-Phase Steel Tailored via Controlled Phase Transformation," *J. Mater. Eng. Perform.*, vol. 29, no. 5, pp. 2783–2791, May 2020, doi: 10.1007/s11665-020-04799-6.
- [58] Y. Wei *et al.*, "Evading the strength-ductility trade-off dilemma in steel through gradient hierarchical nanotwins," *Nat. Commun.*, vol. 5, no. 1, Art. no. 1, Apr. 2014, doi: 10.1038/ncomms4580.

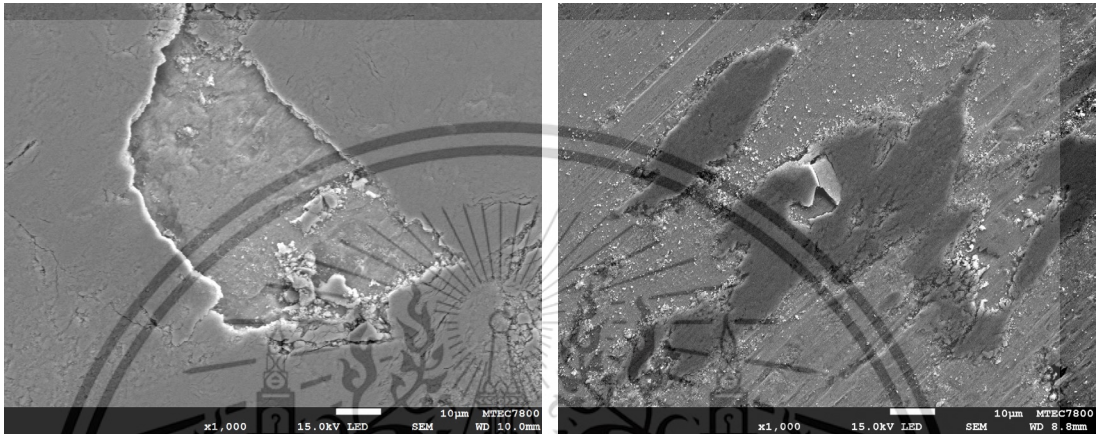
- [59] X. H. Du *et al.*, “Dual heterogeneous structures lead to ultrahigh strength and uniform ductility in a Co-Cr-Ni medium-entropy alloy,” *Nat. Commun.*, vol. 11, no. 1, Art. no. 1, May 2020, doi: 10.1038/s41467-020-16085-z.
- [60] S. W. Wu *et al.*, “Enhancement of strength-ductility trade-off in a high-entropy alloy through a heterogeneous structure,” *Acta Mater.*, vol. 165, pp. 444–458, Feb. 2019, doi: 10.1016/j.actamat.2018.12.012.
- [61] Z. Li, K. G. Pradeep, Y. Deng, D. Raabe, and C. C. Tasan, “Metastable high-entropy dual-phase alloys overcome the strength–ductility trade-off,” *Nature*, vol. 534, no. 7606, Art. no. 7606, Jun. 2016, doi: 10.1038/nature17981.
- [62] W. Guo *et al.*, “Dislocation-induced breakthrough of strength and ductility trade-off in a non-equiatomic high-entropy alloy,” *Acta Mater.*, vol. 185, pp. 45–54, Feb. 2020, doi: 10.1016/j.actamat.2019.11.055.
- [63] J. J. Lewandowski and A. W. Thompson, “Microstructural effects on the cleavage fracture stress of fully pearlitic eutectoid steel,” *Metall. Mater. Trans. A*, vol. 17, no. 10, pp. 1769–1786, Oct. 1986, doi: 10.1007/BF02817275.
- [64] Y. Du, X. Gao, X. Wang, X. Wang, Y. Ge, and B. Jiang, “Tribological behavior of austempered ductile iron (ADI) obtained at different austempering temperatures,” *Wear*, vol. 456–457, p. 203396, Sep. 2020, doi: 10.1016/j.wear.2020.203396.
- [65] H. Zhang, Y. Wu, Q. Li, and X. Hong, “Mechanical properties and rolling-sliding wear performance of dual phase austempered ductile iron as potential metro wheel material,” *Wear*, vol. 406–407, pp. 156–165, Jul. 2018, doi: 10.1016/j.wear.2018.04.005.
- [66] V. Fontanari, M. Benedetti, C. Girardi, and L. Giordanino, “Investigation of the lubricated wear behavior of ductile cast iron and quenched and tempered alloy steel for possible use in worm gearing,” *Wear*, vol. 350–351, pp. 68–73, Mar. 2016, doi: 10.1016/j.wear.2016.01.006.
- [67] D. Zeng, L. Lu, N. Zhang, Y. Zhang, and J. Zhang, “Investigation on the scuffing resistance of ductile cast iron as affected by fine particle bombardment to produce surface hardened layer and micro-dimpled surface,” *Wear*, vol. 378–379, pp. 174–182, May 2017, doi: 10.1016/j.wear.2017.02.046.
- [68] J. Zhang, N. Zhang, M. Zhang, D. Zeng, Q. Song, and L. Lu, “Rolling–sliding wear of austempered ductile iron with different strength grades,” *Wear*, vol. 318, no. 1–2, pp. 62–67, Oct. 2014, doi: 10.1016/j.wear.2014.06.015.

- [69] J. Wang, Y. Cheng, Y. Zhang, Z. Yin, X. Hu, and Q. Yuan, "Friction and wear behavior of microwave sintered Al₂O₃/TiC/GPLs ceramic sliding against bearing steel and their cutting performance in dry turning of hardened steel," *Ceram. Int.*, vol. 43, no. 17, pp. 14827–14835, Dec. 2017, doi: 10.1016/j.ceramint.2017.07.231.
- [70] T. K. Kandavel, R. Chandramouli, M. Manoj, B. Manoj, and D. K. Gupta, "Influence of copper and molybdenum on dry sliding wear behaviour of sintered plain carbon steel," *Mater. Des.*, vol. 50, pp. 728–736, Sep. 2013, doi: 10.1016/j.matdes.2013.03.037.
- [71] E. Zdravecká, J. Tkáčová, and M. Ondáč, "Effect of microstructure factors on abrasion resistance of high-strength steels," *Res. Agric. Eng.*, vol. 60, no. 3, pp. 115–120, Sep. 2014, doi: 10.17221/20/2013-RAE.
- [72] A. Kumar, S. Kumar, N. K. Mukhopadhyay, A. Yadav, V. Kumar, and J. Winczek, "Effect of Variation of SiC Reinforcement on Wear Behaviour of AZ91 Alloy Composites," *Mater. Basel Switz.*, vol. 14, no. 4, p. 990, Feb. 2021, doi: 10.3390/ma14040990.
- [73] R. L. Deuis, C. Subramanian, and J. M. Yellup, "Dry sliding wear of aluminium composites—A review," *Compos. Sci. Technol.*, vol. 57, no. 4, pp. 415–435, Jan. 1997, doi: 10.1016/S0266-3538(96)00167-4.
- [74] M. B. N. Shaikh, T. Aziz, S. Arif, A. H. Ansari, P. G. Karagiannidis, and M. Uddin, "Effect of sintering techniques on microstructural, mechanical and tribological properties of Al-SiC composites," *Surf. Interfaces*, vol. 20, p. 100598, Sep. 2020, doi: 10.1016/j.surfin.2020.100598.

APPENDIX A

SEM of Worn Surface with EDS and Fracture Surface

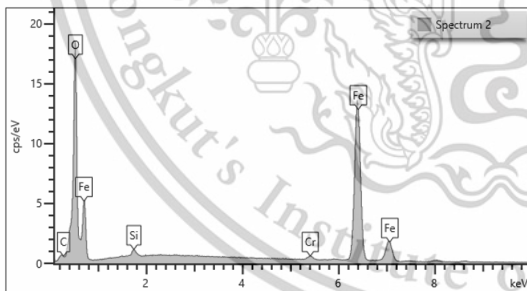
High magnification of SEM image of worn surface of sintered 00 & 30Co alloys under 15N normal load



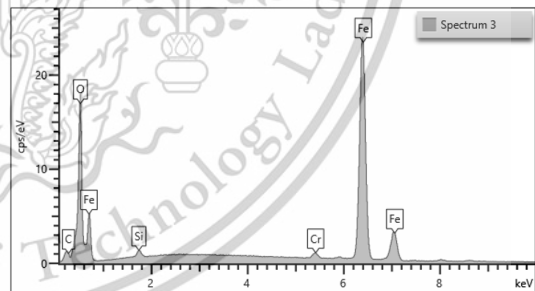
Sintered 00Co alloy

Sintered 30Co alloy

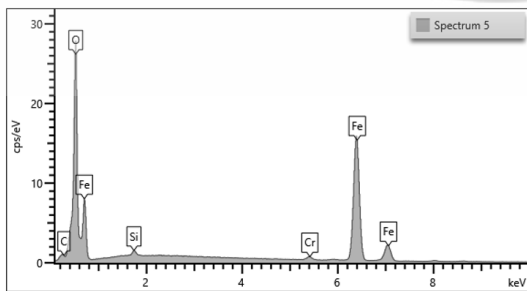
EDS spectrum of sintered 05Co alloy, sintered 10Co alloy, sintered 20Co and sintered 25Co alloy respectively



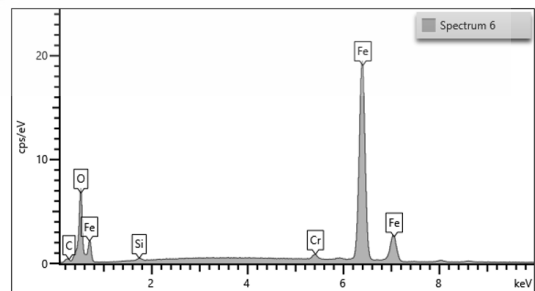
Sintered 05Co alloy



Sintered 10Co alloy



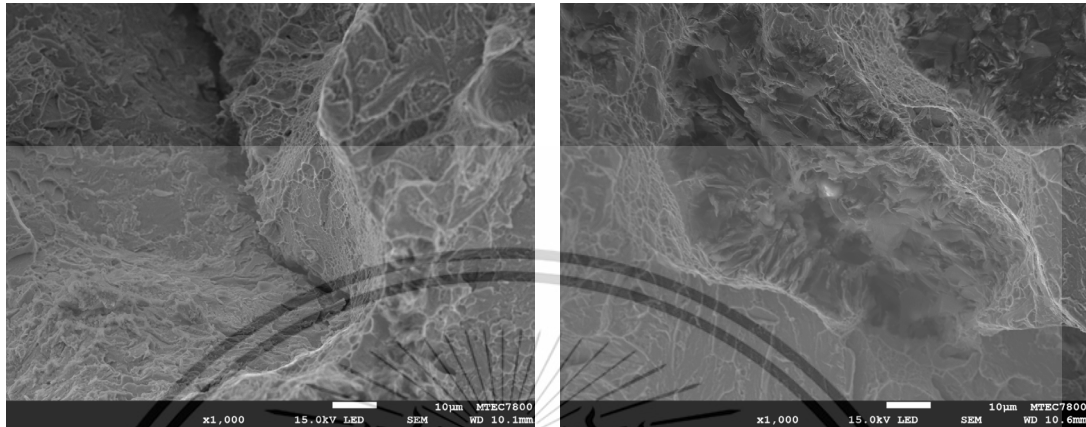
Sintered 20Co alloy



Sintered 25Co alloy

This material is reserved for educational use only, not allowed for commercial use.

High magnification of SEM images of surface fracture of sintered 00Co, sintered 15Co and sintered 30Co alloys respectively



Sintered 00Co alloy

Sintered 15Co alloy

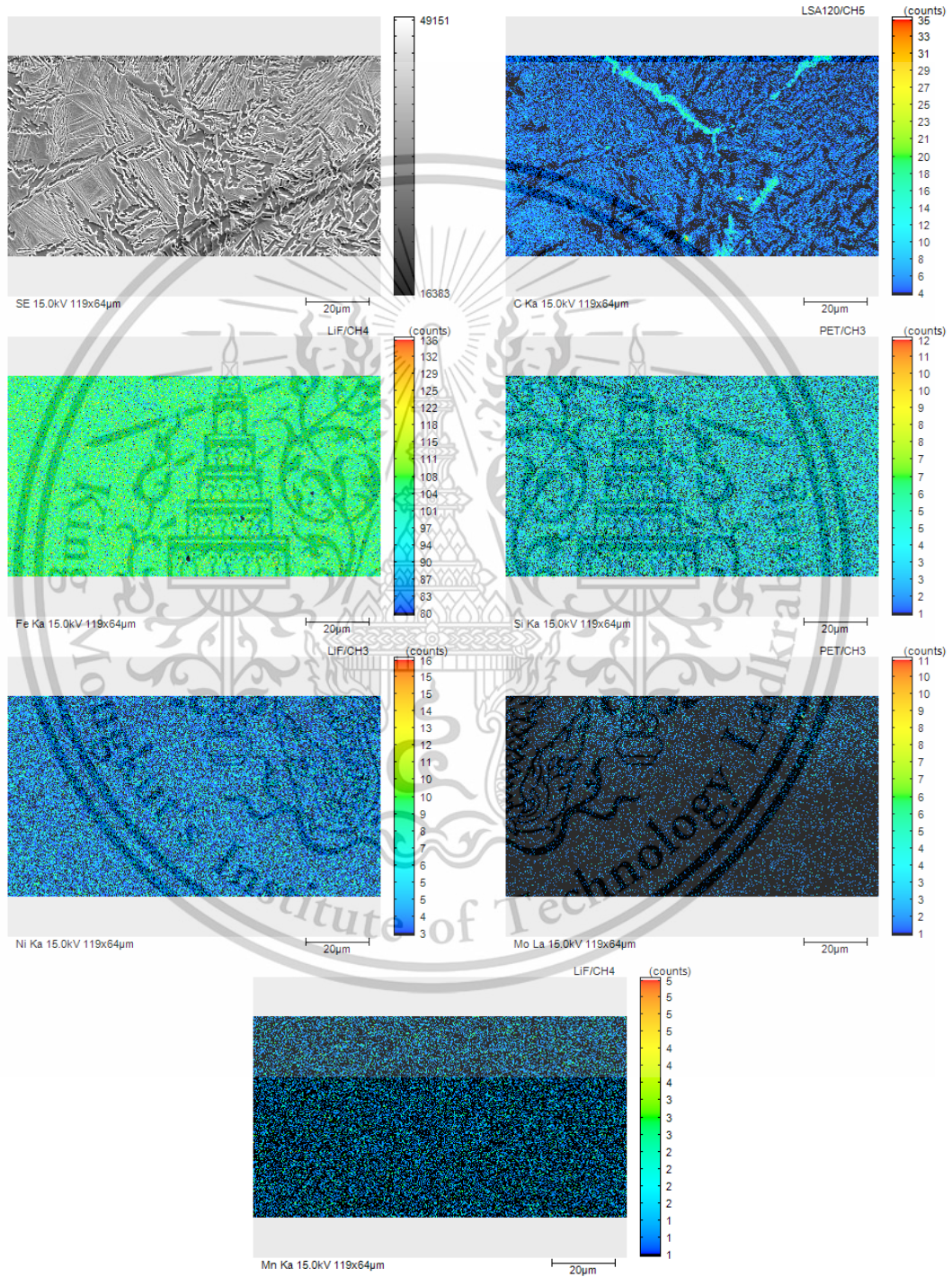


Sintered 30Co alloy

Appendix B

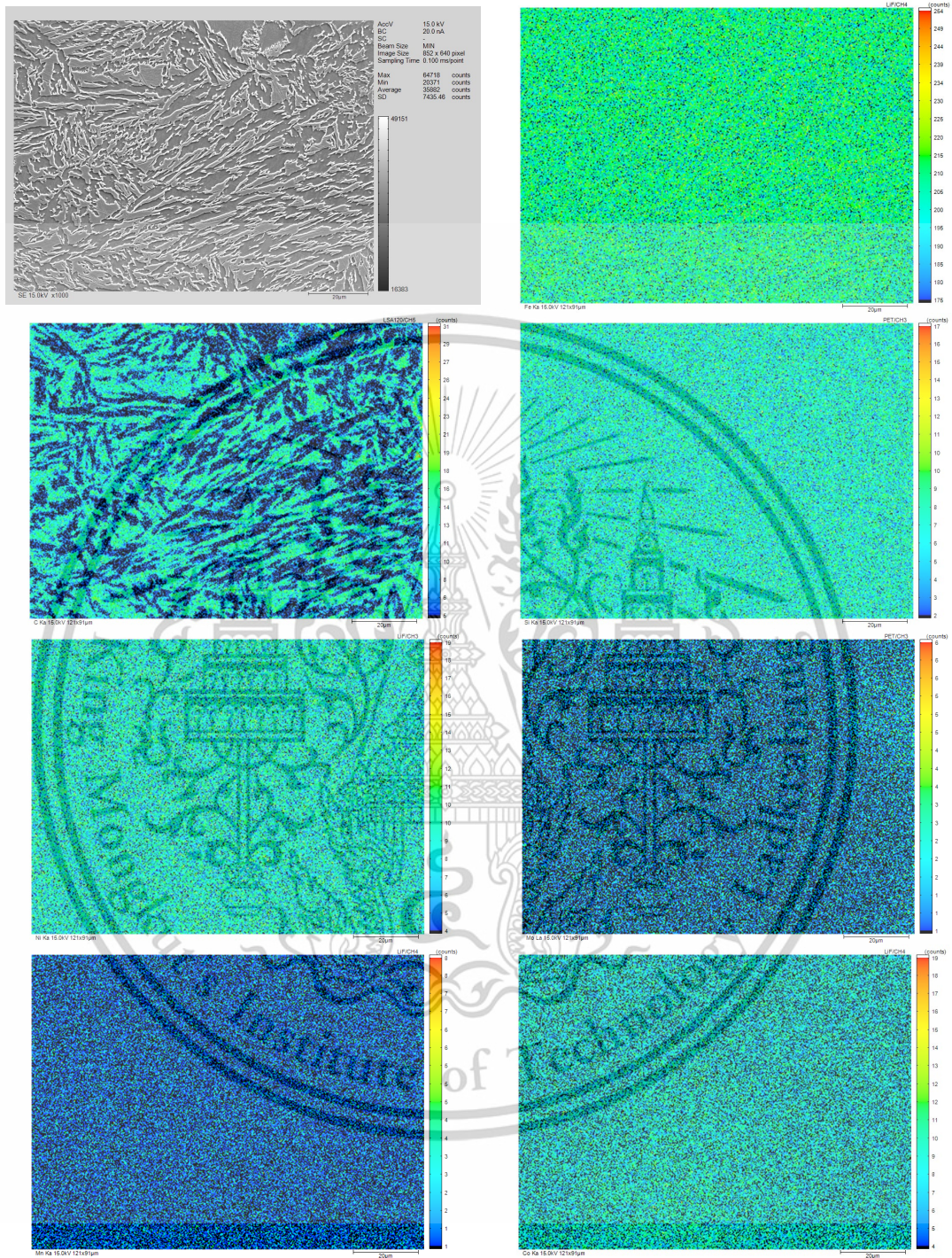
EPMA and X-Ray Analysis of sintered alloys

EPMA Mapping Analysis of Sintered 00Co Alloys



This material is reserved for educational use only, not allowed for commercial use.

EPMA Mapping Analysis of Sintered 30Co Alloys

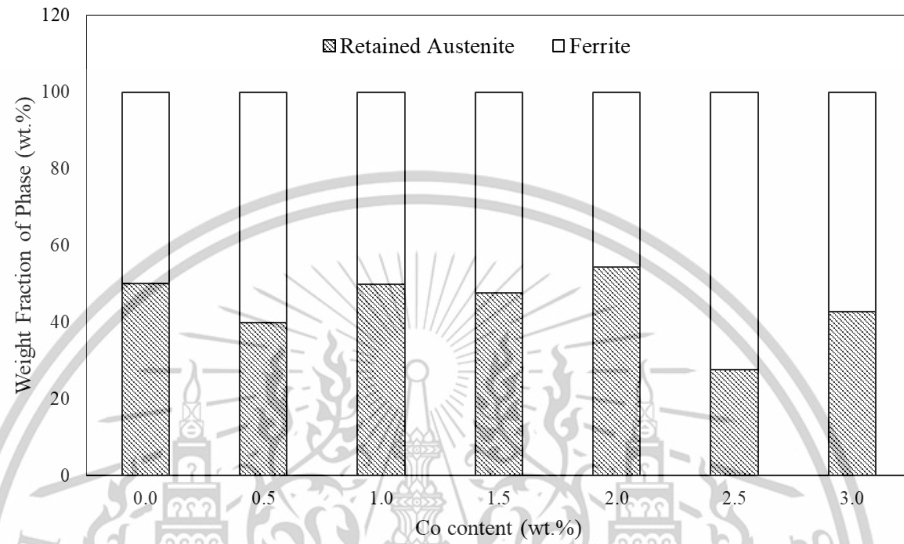


This material is reserved for educational use only, not allowed for commercial use.

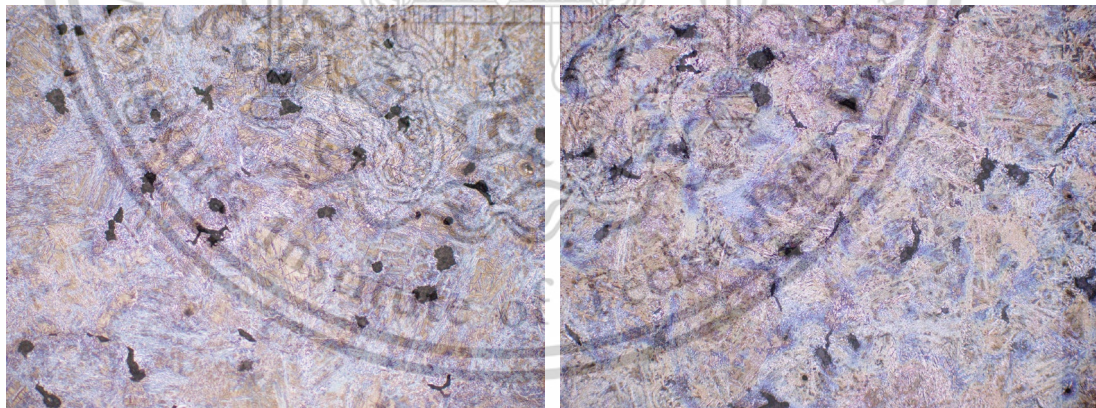
APPENDIX C

Weight fraction plot and OM images of sintered alloys at low magnification

Weight Fraction of each sintered alloys

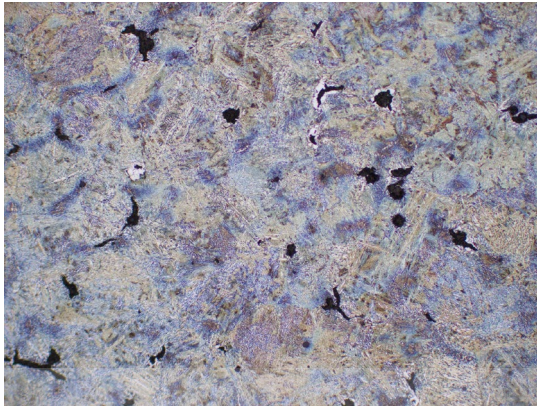


OM images at low magnification of each sintered alloys

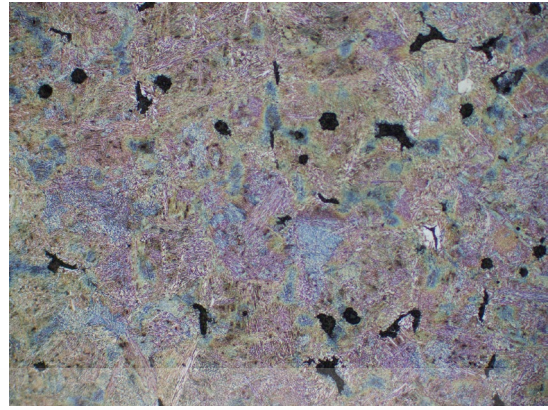


Sintered 00Co alloy

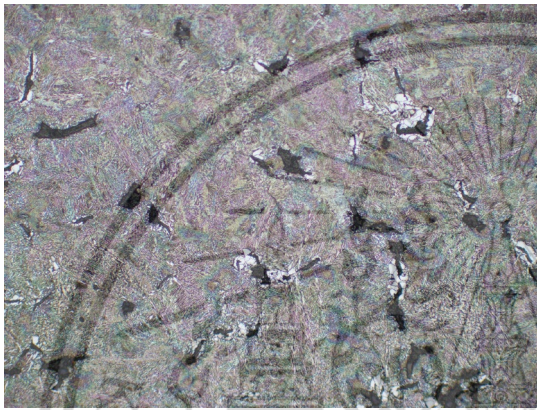
Sintered 05Co alloy



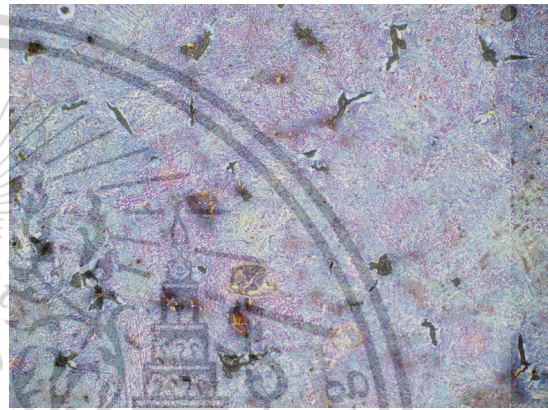
Sintered 10Co alloy



Sintered 15Co alloy



Sintered 20Co alloy



Sintered 25Co alloy



Sintered 30Co alloy

AUTHOR BIOGRAPHY

Author: Mr. Viseth Putsaccada
Nationality: Cambodian
Degree: Master of Engineering
Date of Birth: 01st December 1999
Place of Birth: Kampot, Cambodia

Undergraduate and Graduate Education:

Master of Engineering in Automotive and Advanced Transportation Engineering,
King Mongkut's Institute of Technology Ladkrabang, Bangkok, 2024

Bachelor's degree in Mechanical and Industrial Engineering,
Institute of Technology of Cambodia, Phnom Penh, 2021

Major: Automotive and Advanced Transportation Engineering

Presentations and Publications:

[1] Putsaccada V, Jittrapon-Wongsa N, Nhaoto O, Ruangdaj T 2022 Enhancing ductility of sintered Fe-Ni-Mo-Mn-Si-C alloy by Co addition 12th International Conference on Mechanical Engineering (TSME-ICoME 2022), December 13th-16th, Phuket Thailand

[2] Putsaccada V, Jittrapon-Wongsa N, Nhaoto O, Ruangdaj T 2024 Enhancing ductility of sintered Fe-Ni-Mo-Mn-Si-C alloy by Co addition AIP Conference Proceedings